ABSTRACT

Title of dissertation: DYNAMICS OF VAPOR COMPRESSION CYCLE WITH THERMAL INERTIA

Rohit Dhumane
Doctor of Philosophy
2018

Dissertation directed by: Professor Reinhard Radermacher
Department of Mechanical Engineering

The use of heating, ventilation, air conditioning, and refrigeration (HVACR) systems is always increasing. Reducing energy consumption has become necessary in modern times for environmental, economic and legislative reasons. Thus, there is ongoing research to improve the performance and reduce the negative environmental impact of these systems. HVACR systems are normally sized for peak load conditions. As a result, these systems operate under off-peak conditions most of the time by on-off cycling. The efficiency of the system during cycling is lower than continuous operation due to transient losses caused by refrigerant migration and redistribution. This motivates a detailed understanding of the dynamics of vapor compression systems (VCS) for their improved design and performance.

The dissertation contributes towards reducing energy consumption from HVACR by exploring both sides: improving the performance of current systems and developing highly energy efficient personal conditioning systems (PCS) which reduce the load of HVACR systems altogether. PCS reduce the energy consumption of building

HVACR by up to 30%. Multi-physics modeling including thermo-fluid, electricity and mechanical domains is conducted to compare performance of four PCS employing different thermal storage options. The dissertation then focuses on vapor compression system based version of PCS called Roving Comforter, operating cyclically between its cooling and recharge mode. Exhaustive study of design space including optimization of thermal storage, operation with a natural refrigerant and alternate recharge modes is conducted to improve its overall coefficient of performance.

The dissertation then presents comprehensive dynamic validated modeling of air-conditioning systems operating in cyclic operations to characterize cyclic losses. Parametric study with different operating conditions is carried out to provide guidelines for reduction of these cyclic losses. Secondly, a physically based model of the test setup for quantifying the cyclic losses of HVACR systems is developed and used to understand its influence on the cyclic losses. A new term called Thermal Inertia Factor is defined to enable more uniform rating of equipment from various test centers and help selection of actual energy efficient HVACR.

DYNAMICS OF VAPOR COMPRESSION CYCLE WITH THERMAL INERTIA

by

Rohit Dhumane

Dissertation submitted to the Faculty of the Graduate School of the
University of Maryland, College Park in partial fulfillment
of the requirements for the degree of
Doctor of Philosophy
2018

Advisory Committee:
Dr. Reinhard Radermacher, Chair/Advisor
Dr. Raymond Adomaitis, Dean's Representative
Dr. Jelena Srebric
Dr. Amir Riaz
Dr. Bao Yang
Dr. Jiazhen Ling

Dedication

Dedicated to my parents for their support and sacrifice to encourage me to pursue my studies in a different country.

Acknowledgments

I would first of all like to extend sincere thanks to my advisor, Prof Reinhard Radermacher, for providing me several exciting opportunities to work with world-class scholars during my past four years and also funding my graduate school. His timely guidance has benefited me not only in technical aspects, where he is one of the foremost scholars, but also in matters of professional etiquette and ethics. CEEE is a highly successful research group due to his excellent work practices and learning these first hand from him will help me immensely in my career. I also thank members of my committee with whom I share good relations. They have been kind enough to share their valuable time and expertise to provide direction to the dissertation; Prof Jelena Srebric for her constant encouragement and motivation during RoCo meetings and towards my Ph.D. proposal, Prof Raymond Adomaitis for his always always-smiling and encouraging support during Solar Decathlon, Prof Bao Yang for encouragement during his courses in my initial stages of graduate school and Prof Amir Riaz during several friendly interactions on the office floor.

Next I would like to thank Dr Vikrant Aute for providing me two extremely high-quality research projects, both of them being unique in their own aspects. His outstanding knowledge in a variety of mathematical domains and guidance towards approaching problem has benefited me enormously. This Ph.D. work could not have been possible without Dr Jiazhen Ling, who taught me how to navigate through graduate school successfully. He is a superman who provided me guidance on a variety of aspects from teaching me Modelica, on managing time for multiple tasks,

writing publications and to several aspects on personal side as well. I also thank Dr Yunho Hwang with whom I got to work during my PhD projects and Solar Decathlon. Finally, I thank Jan Muehlbauer for providing me several crash courses on experimental design: be it installing thermocouples, refrigerant tubes, water pumps, controls in Arduino and so on. I feel really privileged to have gotten an opportunity to collaborate with all the CEEE faculty, who have been kind, patient and very approachable.

I would also like to thank sponsors of both my projects, ARPA-E and Carrier Center of Excellence. I am grateful to Jack Esformes and Allen Chad Kirkwood for providing their technical insights, encouragement and professional opportunities in the past two years. I would also especially thank Dr Anne Mallow for teaching me best practices on publication over numerous telephone interactions. It has really been a pleasure to have her as a senior student and mentor. Among office colleagues, I feel lucky to have Zhenning Li for entirety of my graduate school life and being part of several wonderful memories over the past four years. His kindness and helpfulness is unbelievable. Other colleagues who have brought positive influence on my graduate life are Ransisi Huang (lunch mate), Ryan Kenneth, Sarah Troch, Andrew Riveira (previous 3 for introducing me to American culture), Viren Bhanot (the only person to whom I talked Hindi in office), Daniel Bacellar (brainstorming research directions and guidance on graduate school life), James Tancabel (thanks for numerous edits!) and Arne Speerforck (teaching German publication best practices). Finally, I also extent my gratitude to my flatmates Shayandev Sinha and Parth Desai, who are my family here in College Park.

Table of Contents

List of Tables viii

List of Figures ix

1 Introduction 1
1.1 Motivation . . . 1
1.2 Literature Review . . . 5
1.2.1 Vapor Compression System Modeling with Modelica . . . 6
1.2.1.1 Modeling Thermo-Fluid Systems with Modelica . . . 7
1.2.1.2 Stream Connectors . . . 10
1.2.1.3 Current State of Art of Modeling VCC . . . 13
1.2.1.4 Mass Conservation in Dynamic VCC Models . . . 15
1.2.1.5 Non-homogeneous two-phase flow . . . 17
1.2.2 Thermosiphon Modeling . . . 19
1.2.3 Phase Change Materials . . . 21
1.2.3.1 Numerical Modeling . . . 22
1.2.3.2 3-D analysis . . . 23
1.2.3.3 System simulation . . . 24
1.2.4 Personal Conditioning Systems . . . 25
1.2.5 Refrigerant Migration . . . 28
1.2.6 Current methods for estimating HVAC cyclic performance . . . 31
1.3 Objectives . . . 38
1.4 Thesis Outline . . . 39

2 Portable Personal Conditioning Devices 40
2.1 Multi-physics Modeling of PPCS . . . 41
2.1.1 PCM Heat Exchanger . . . 45
2.1.2 Air-to-Water Heat Exchanger . . . 49
2.1.3 Water Tank . . . 50
2.1.4 Ice Tank . . . 51
2.1.5 Battery . . . 52
2.1.6 Robotic Platform . . . 55

2.2 Results and Discussion . . . 57
2.2.1 System Comparison . . . 60
2.2.2 Air Flow Rate . . . 63
2.2.3 Phase Change Material . . . 65
2.2.4 Price Considerations . . . 66

3 Development of Vapor Compression Cycle based Personal Conditioning System 72
3.1 Introduction . . . 72
3.2 Component Modeling . . . 76
3.2.1 Downcomer and Riser . . . 77
3.2.2 Phase Change Material Control Volume . . . 78
3.2.2.1 PCM Heat Storage . . . 79
3.2.2.2 PCM Heat Transfer . . . 80
3.2.2.3 Empirical heat transfer coefficient function . . . 81
3.2.3 Thermosiphon Evaporator Control Volume . . . 84
3.3 System Modeling . . . 88
3.4 Evaluating Performance of Graphite Enhanced PCM . . . 93

4 Performance Improvements of Personal Conditioning Systems 100
4.1 Introduction . . . 100
4.2 Performance with a natural refrigerant . . . 100
4.2.1 Empirical PCM heat transfer coefficient . . . 101
4.2.2 Simulation of Cooling Operation of Roving Comforter . . . 105
4.2.3 Comparison of RoCo performance with R134a and R290 . . . 109
4.3 Analysis of heat pump based recharge . . . 113
4.3.1 Heat Pump System Description . . . 113
4.3.2 Modeling graphite enhanced PCM storage . . . 115
4.3.3 Validation of graphite enhanced PCM model . . . 118
4.3.4 Heat Pump based recharge . . . 122

5 Cyclic Losses in Vapor Compression System 127
5.1 Introduction . . . 127
5.2 Modeling Vapor Compression System . . . 127
5.2.1 Heat Exchangers . . . 128
5.2.1.1 Refrigerant Control Volume . . . 131
5.2.1.2 Air side Control Volume . . . 135
5.2.1.3 Tube Walls and Fins Control Volume . . . 136
5.2.2 Compressor . . . 137
5.2.3 Thermostatic Expansion Valve . . . 138
5.2.4 Refrigerant Lines . . . 140
5.3 Code Tester . . . 141
5.3.1 Background . . . 141
5.3.2 Model development . . . 143
5.4 Results and Discussion . . . 145

5.4.1 Validation of cyclic test performance . . . 146
5.4.2 Refrigerant Migration . . . 149

6 Analysis of evaluation of Cyclic Degradation Coefficient 156
6.1 Introduction . . . 156
6.2 Influence of thermal inertia from Code Tester . . . 157
6.3 New Correction Method to reduce Code Tester influence . . . 162
6.4 Measurement uncertainty . . . 166

7 Summary 176
7.1 Conclusions . . . 176
7.2 Contributions . . . 178

Bibliography 181

List of Tables

1.1 Cyclic Losses from Refrigerant Migration 28
1.2 Refrigerant Charge Distribution in HVAC Systems 29

2.1 Thermophysical properties of PCM 48
2.2 Dimensions for the Air to Water Heat Exchanger 51
2.3 Total HVAC energy savings when varying cooling setpoints [109] . . . 67

3.1 Evaluation of Ideal Cd for CT-A and CT-B 82
3.2 Geometric parameters of PCMHX 86
3.3 Properties of PCM and PCM composites 94
3.4 CENG thermal storage geometry 96

5.1 Evaporator geometry parameters 129
5.2 Condenser geometry parameters 130

6.1 Evaluation of Ideal Cd for CT-A and CT-B 165
6.2 Uncertainties for evaluation of Cd 169
6.3 Uncertainties for evaluation of Cd 175

List of Figures

1.1 Sequence of Operation in a Typical Refrigerant Control Volume . . . 9
1.2 The FluidPort connector in Modelica Standard Library 11
1.3 Connectors connecting three thermo-fluid components 12
1.4 Object diagram of heat exchanger 14
1.5 Refrigerant density of R410a as the static quality varies from a sub-cooled liquid to a superheated vapor at a pressure of 2850 kPa 16
1.6 Schematic of Environment Chamber showing Code Tester 32
1.7 Schematic of a Code Tester 33

2.1 Portable Personal Conditioning System in Operation 41
2.2 Schematics of the four cooling systems compared 42
2.3 Model of Ice Tank System 43
2.4 Model of Vapor Compression System 44
2.5 Discretization of PCM Control Volume 46
2.6 Discretization of Waterside Control Volume 49
2.7 Modeling of Battery Pack by Scaling a Single Cell Modeled as an RC Circuit 53
2.8 Validation of Battery Model 54
2.9 Free Body Diagram for Robotic Platform 56
2.10 Input Set for the Robotic Platform 56
2.11 Temperatures at various locations in WTS 57
2.12 Temperatures at various locations in ITS 58
2.13 Temperatures at various locations in PCMS 59
2.14 Temperatures at various locations in VCS 60
2.15 Breakdown of Power Consumption in VCS 61
2.16 Comparison of Weight 61
2.17 Comparison of Price 62
2.18 Comparison of Battery 62
2.19 Cooling Capacity Required to Obtain the Same Supply Air Temperature at Different Ambient Conditions 64
2.20 Power Consumption by the Four PPCS 68
2.21 Mean Yearly Savings from PPCS Operation 68

2.22 Maximum Yearly Savings from PPCS Operation 69
2.23 Payback Evaluation from Mean Savings for VCS 70
2.24 Payback Evaluation from Maximum Savings for VCS 70

3.1 Schematic of two modes of operation of RoCo 73
3.2 Control volume for downcomer 77
3.3 Schematic of the setup for evaluating heat transfer coefficient on the shell side of PCM storage and the helical coil used for the experiment 82
3.4 Temperatures measured by RTDs (resistance temperature detector) located on the water-side at inlet and outlet of PCM-HX 83
3.5 Temperatures averaged from the three thermocouples for wall, and ten thermocouples located inside PCM 84
3.6 Melt fraction as a function of temperature 85
3.7 Heat transfer coefficient as a function of melt fraction 85
3.8 PCM-HX used in RoCo and the control volume used for modeling . . 87
3.9 Model diagram for solidification experiment with water 89
3.10 Water temperatures at the inlet and outlet of PCM-HX 90
3.11 Modelica model used for the thermosiphon simulation with pure PCM 91
3.12 PCM temperature comparison between experimental data and simulation 92
3.13 Condenser airside temperature comparison between experimental data and simulation 93
3.14 Average heat transfer coefficient as a function of CENG volume fraction 95
3.15 Relative performance of various CENG composites capable of a two-hour operation time 96
3.16 Temperature profile during thermosiphon operation with enhanced graphite thermal storage 97
3.17 Heat removal rate during thermosiphon operation with enhanced graphite thermal storage 98
3.18 COP of RoCo for the different thermal storage options 99

4.1 Temperatures at the inlet and outlet of PCM-HX 102
4.2 Mass flow rate of water flowing through PCM-HX 103
4.3 Temperatures of the thermocouple on PCM-HX tube 103
4.4 Enthalpy temperature function obtained from DSC data 104
4.5 Lumped PCM Temperature obtained from Enthalpy 104
4.6 Melting HTC as a function of melt fraction 105
4.7 Model diagram for cooling cycle of Roving Comforter 106
4.8 Validation of Suction and Discharge Pressure of RoCo 108
4.9 Validation of Mass Flow Rate of RoCo 109
4.10 Validation of Compressor Power of RoCo 110
4.11 Validation of Measured Cooling Capacity 110
4.12 Comparison of cooling capacity 110
4.13 Comparison of operating pressures 111
4.14 Comparison of mass flow rate 111

4.15 Comparison of compressor power . . . 112
4.16 Schematic showing both thermosiphon and heat pump mode of recharge 114
4.17 Cross section for modeling PCM . . . 116
4.18 Model diagram for discretized PCM control volume . . . 117
4.19 Model diagram for thermosiphon . . . 118
4.20 Comparison of airside temperature across condenser . . . 119
4.21 Refrigerant pressure inside PCM-HX . . . 120
4.22 Refrigerant temperature inside PCM-HX . . . 121
4.23 Temperature of PCM . . . 121
4.24 Model diagram for heat pump recharge . . . 123
4.25 Power consumption of PCM at different RPM with heat pump recharge 124
4.26 Melt fraction of PCM at different RPM with heat pump recharge . . . 125
4.27 Recharge performance by heat pump operation at different compressor RPM . . . 126
4.28 Comparison of various recharge options for RoCo . . . 126

5.1 Model diagram for cyclic D-Test of air conditioner in a Code Tester . 128
5.2 Calculations inside refrigerant control volume of heat exchangers . . . 132
5.3 Void fraction from various correlations at flow conditions of system under investigation . . . 133
5.4 Pressure Drop Regularization . . . 134
5.5 Interpolation of heat transfer coefficient between phases . . . 134
5.6 Schematic of heat transfer interactions in compressor model . . . 138
5.7 Tunnel Air Enthalpy Method Arrangement . . . 142
5.8 Modeling various components of code tester . . . 144
5.9 Component Model of Duct and Mixer . . . 144
5.10 Comparison of suction and discharge pressure . . . 146
5.11 Comparison of refrigerant mass flow rate . . . 147
5.12 Comparison of compressor power . . . 148
5.13 Comparison of code tester outlet thermocouple grid . . . 148
5.14 Comparison of temperatures at suction and discharge . . . 149
5.15 Comparison of temperatures at suction and discharge . . . 150
5.16 Refrigerant distribution in three locations during C-Test . . . 151
5.17 Refrigerant distribution in three locations during D-Test . . . 152
5.18 Case 01 for Refrigerant distribution in three locations during D-Test . 153
5.19 Case 02 for Refrigerant distribution in three locations during D-Test . 154
5.20 Case 03 for Refrigerant distribution in three locations during D-Test . 154

6.1 Distribution of thermal inertia of CT-A . . . 158
6.2 Model diagram for heater test with CT-A . . . 159
6.3 Temperature Validation of Model at Outlet TC grid . . . 160
6.4 Temperature Validation of Model at Mixer TC grid . . . 160
6.5 Net heat stored in code tester during cycling with heater . . . 161
6.6 Parametric study with code tester airflow variables . . . 166
6.7 TLDB for multiple five cyclic D-Tests . . . 172

6.8 Plotting TLDB for all on-cycles from the five cyclic D-Tests 173
6.9 Standard deviation for TLDB array 173

Nomenclature

Abbreviations

$\dot{m}$	Mass Flow Rate [$\mathrm{kg\,s^{-1}}$]
$\dot{Q}$	Heat Exchanger Capacity [W]
$\mathbb{V}$	Voltage [V]
A	Area [$\mathrm{m^2}$]
a	Acceleration [$\mathrm{m\,s^{-2}}$]
C	Capacity of cell [C]
c	Specific Heat Capacity [$\mathrm{J\,kg^{-1}\,K^{-1}}$]
C_d	Cyclic degradation coefficient [$-$]
COP	Coefficient of Performance [$-$]
E	Energy density [$\mathrm{J\,m^{-3}}$]
EER_B	Energy efficiency ratio from B-Test [$\mathrm{Btu/hr-W}$]
F	Force [N]
f	Fanning Friction Factor [$-$]
G	Thermal Conductance [$\mathrm{W\,K^{-1}}$]
g	Acceleration due to gravity [$\mathrm{m\,s^{-2}}$]
h	Specific Enthalpy [$\mathrm{J\,kg^{-1}}$]
I	Current [A]
K	Thermal Degradation Parameter [$-$]
k	Thermal Conductivity [$\mathrm{W\,m^{-2}\,K^{-1}}$]
k_C	Degradation coefficient[C]
L	Latent Heat of Melting [$\mathrm{J\,kg^{-1}}$]

L_t Length [m]

m Mass [kg]

n Number of items

P Power [W]

p Pressure [Pa]

PLF Part Load Factor [−]

q'' Heat flux [$\mathrm{W\,m^{-2}}$]

q Integrated cooling capacity [J]

Q_{abs} Absolute value of charge transferred to and from cell [C]

R Electric Resistance [Ω]

r Radius [m]

S Perimeter [m]

S Surface area [$\mathrm{m^2}$]

$SEER$ Seasonal energy efficiency ratio [−]

SOC State of charge [−]

T Temperature [K]

t Time [s]

t_c Complete cycle time (On+Off) during D-Test [s]

t_o On time during cyclic D-Test [s]

TIF Thermal Inertia Factor [−]

u Kirchoff Temperature [K]

V Volume [$\mathrm{m^3}$]

v Velocity [$\mathrm{m\,s^{-1}}$]

Greek

α Heat Transfer Coefficient [$\mathrm{W\,m^{-2}\,K^{-1}}$]

η_v Volumetric Efficiency [−]

λ Melt Fraction [−]

ρ	Density [$\mathrm{kg\,m^{-3}}$]
θ	Inclination Angle [°]

Subscript

a	acceleration
air	Air side
b	TXV bulb
bat	battery
c	cross section
$cell$	cell
cv	Control Volume
cyc	cyclic test D-Test
d	TXV diaphragm
d	drag
dis	Discharge side of Compressor
dry	dry condition of coil, i.e. no condensation
e	Evaporator
eff	Effective
ext	external
f	friction
fc	Forced Convection
fin	Heat Exchanger Airside Fins
$flow$	Refrigerant Flow Direction during On-cycle
g	gravity
i	Inner
ice	ice
in	inlet
j	Grid point in the discretized control volume

L	Liquid
$leak$	Refrigerant Leakage during Off-cycle
m	Melting Temperature
nc	Natural Convection
o	Outer
out	outlet
p	parallel arrangement of cells
pcm	Phase Change Material
ref	Refrigerant Side
S	Solid
s	series arrangement of cells
sat	Saturation Temperature Correction
sen	Sensible Heat
sl	Solid to Liquid Phase Change
ss	steady state test, C-Test
suc	Suction side of Compressor
t	total
ts	Thermosiphon
$tube$	Refrigerant Tube
$tube$	refrigerant tubing
V	Vapor
vcc	Vapor Compression Cycle
w	water

Chapter 1: Introduction

Human beings are sophisticated creatures and have been modifying their surroundings to make their existence more comfortable. With development of languages and written communication, it has become possible to connect with generations from the past and use their knowledge and wisdom. Human creativity over the years has enabled the use of discoveries like fire from basic uses like cooking and protection, to several modern ones like automobile combustion and fireworks. With the amount of natural resources being limited and the human population ever increasing, it is prudent to adapt a sustainable lifestyle. This requires reduction of our dependence on natural resources.

1.1 Motivation

With the goal of promoting sustainability, this thesis looks at the generic question of "What are more efficient ways of using energy?" from the point of view of space heating and cooling in buildings.

Heating, ventilating and air conditioning (HVAC) systems consume 14% of US primary energy consumption [1]. Since this is a sizable portion of the total energy consumption, there are many ongoing efforts to achieve improved building heating

and cooling efficiency. Over 15 billion dollars are spent on energy for residential air-conditioning alone each year, and air-conditioning remains the largest source of peak electrical demand [2]. Reduction of energy consumption and refrigerant charge in HVAC systems is becoming increasingly important for environmental, legislative and economic reasons.

Current approaches can generally be categorized as novel configurations of HVAC components, improved designs of components and more strategic use of existing system through different control and optimization strategies [3]. Technologies being developed to reduce energy consumption in building HVAC include, but are not limited to thermoelectric systems [4, 5], shifting peak demand with phase change materials [6–8], variable refrigerant flow systems [9], use of new refrigerant mixtures [10], ground-source heat pump systems [11, 12], desiccant cooling [13, 14], ejector systems, use of thermally activated building systems [15], novel heat exchangers [16], controllers based on optimization of energy consumption [17], and energy efficient design of building envelope [18–20].

However, even though these new approaches for enhanced HVAC performance tend to save operational costs, capital investment is greater compared to conventional air conditioning systems [21–23]. Furthermore, most of them require retrofitting, which is not cost-effective because of much longer service life of the building components (e.g, residential HVAC systems are designed for 10 to 25 years) [24]. The average life span of residential buildings is about 30 to 40 years [25], during which building owners are not motivated to invest on retrofitting due to longer payback periods (typically greater than 5 years [26]). By retrofitting existing

roof-top units with advanced controls, Wang et al. (2015) [27] observed average 57% energy consumption savings. Thus, there is a great scope in saving building energy consumption and it is essential to develop technologies that can be implemented in existing buildings in a cost-effective manner.

Secondly, much of building HVAC energy consumption goes into maintaining narrow indoor temperature ranges that building operators consider necessary for comfort, however, this is not actually true [28]. Current practice persists because there is a substantial reluctance in the building and real estate industry to try new measures for indoor comfort control [29]. In a broad overview of best practices for the design of offices, Aronoff and Kaplan [30] argue that because the thermal conditions that individuals find comfortable are so variable, the ideal solution would be to allow everyone to set the conditions that they find comfortable. However, improved spatial control requires a reconfiguration of the building interior or complete replacement of the building HVAC units. It is highly unlikely that spatial control with current building HVAC technologies will reach the resolution of the individual occupant [29].

Vapor compression cycle (VCC) have been at the heart of HVAC systems for several years now. Through research efforts spanning several decades and regulatory control, their energy efficiency has been constantly rising. However, thermodynamics and heat transfer put a limit on the extent to which the efficiency of these systems can be improved. Use of local thermal management systems reduces the load on the building HVAC and permits them to operate at elevated set-points temperature without compromising personal comfort. Development of a low-cost, low-energy consuming local thermal management system is expected to provide 10 to 30% of

reducing in the HVAC energy consumption of buildings.

Building HVAC systems are sized for peak capacity and operate cyclically most of the time. Refrigerant migration and redistribution have been identified as factors affecting the dynamic cyclic performance of all refrigeration and AC equipment. When the compressor is turned off, the condenser gradually cools down, while the evaporator heats up, depending on the surrounding temperature. The refrigerant migrating from condenser to evaporator carries energy and disturbs the steady state operating parameters of the system. This refrigerant and heat redistribution presents itself as a load during the startup as the thermal mass of the system and so the system has to be reconditioned to steady state conditions. This reconditioning represents a loss in capacity of the system during the startup until the steady operating conditions are achieved. Transient losses of about 18.5% have been reported by Kapadia et al. [31]. The increased understanding of the process of refrigerant migration is expected to enable improved design of HVAC systems for cyclic performance.

The measurements of the cooling capacity are performed as per the AHRI 210/240 [32] standard. However, the standard is not sufficiently uniform and leads to variations in the measured cyclic performance and seasonal energy efficiency ratio of the unit, which provide guidance for selecting the most energy efficient air conditioner. The present study represents a first attempt at understanding and reducing the variations in the measured cyclic performance of the same HVAC system with different measurement setup.

To summarize, there are several inefficiencies existing in the use of energy

by the current HVAC systems. The physics involved in the operation of these technologies is complex and development of dynamic modeling tools to understand their operation has potential towards their improvement. Modeling and simulation are indispensable when dealing with complex engineering systems. Dynamic simulations can be used to design and evaluate systems, controllers and understand system trends for improved design. Several dynamic models are developed in the thesis capable of answering design questions related to dynamic operation of a variety of two-phase thermo-fluid systems. The models are validated with experiment data and then exercised to suggest improvements in the existing technology towards reduced energy consumption in building space heating and cooling.

1.2 Literature Review

Modelica is used as the primary tool for the current research. So, a literature review of the state of the art is presented to familiarize the reader to the basic terminology and unique approaches of this language. The existing technology for personal conditioning system is reviewed to understand current state-of-art and identify challenges for widespread implementation. Studies to improve cyclic operation of VCC are reviewed to understand the dynamics of cyclic operation of HVAC and standards for its quantification.

1.2.1 Vapor Compression System Modeling with Modelica

Modeling in Modelica is much different from the standard procedural coding platforms. It has several unique features which makes it very challenging to adjust to the new way of thinking. The next subsection attempts to provide an appreciation of the advantages and limitations of the framework as well as familiarize the reader to the terminology used throughout this thesis.

Modelica is a language for modeling of physical systems, designed to support effective library development and model exchange. It is specifically designed to facilitate model reuse [33]. It is intended for modeling within many application domains such as electrical circuits, multi-body systems, hydraulics, thermodynamics, etc. and is intended to serve as a standard format so that models arising in different domains can be exchanged between tools and users [34].

Modelica is particularly appropriate for the development of system models, due to its object-oriented, declarative and acausal modeling approach [35]. The Modelica view on object orientation is different than traditional object oriented programming languages like Simula, C++, Java, etc., as well as procedural languages such as Fortran or C. It emphasizes structured mathematical modeling and views object orientation as a structuring concept that is used to handle the complexity of large system description to further simplify analysis [36]. Thus, the system models can have multiple levels and it is possible to create models which can have many sub-models, which have sub-models themselves.

The concept of declarative programming is inspired by mathematics, where it

is common to state or declare what holds, rather than giving a detailed stepwise algorithm on how to achieve the desired goal, as required when using procedural languages. This relieves the programmer from the burden of keeping track of transport of data between objects through assignment statements, makes the code more concise and easier to change without introducing error [36].

Acausal modeling is a declarative modeling style, meaning modeling based on equations instead of assignment statements. Equations do not specify which variables are inputs and which are outputs, whereas in assignment statements variables on the left hand side are always outputs and variables on the right hand side are always inputs. Thus, the causality of equation based models is unspecified and becomes fixed only when the corresponding equation systems are solved. Equations are more flexible than assignments since they do not prescribe a certain data flow direction or execution order. This is the key to the physical modeling capabilities and increased reuse potential of Modelica classes [36]. However, thinking in terms of equations is a bit unusual for a programmer. This makes development in Modelica quite challenging since it requires a novel outlook towards programming. Strategies unique to the domain of modeling are developed and distributed as part of `Modelica Standard Library` to aid designers. The following section describes thermo-fluid system modeling with Modelica and a brief discussion on the current state of the art.

1.2.1.1 Modeling Thermo-Fluid Systems with Modelica

The modeling of thermo-fluid systems started with the efforts of Tummescheit and Eborn [37–41] which provided strong groundwork with sufficiently generic components and framework to enable extensive detailed component development. Consequently, several

libraries developed by expanding their work in the past decade e.g. Thermal-Flow Library [39, 40], ThermoTwoPhase Library [42], Air Conditioning Library [43, 44], Modelica Fluid Library [45], TIL [46] and CEEE Modelica Library [47].

One of the important simplifications in modeling of dynamical systems are time scale abstractions. Three of these time scale abstractions are very common [39]:

1. Features of the system that change much slower than the current time scale of interest are treated as constants.

2. Dynamics which settle on a timescale faster than those of main interest in the model are treated as always being in steady state.

3. Changes in conserved quantities which happen in much shorter times than those of interest are treated as jumps.

Thermo-fluid systems use two types of abstractions, which work well for a large class of real process equipment. Large equipment is modeled by storage of mass and energy in a control volume. Equipment with small volumes but high power densities like pumps, turbines, valves and orifices have a negligible mass and energy storage but often large changes in pressure and sometimes kinetic energy. Large volume equipment will be refered to as `control volume`, while the small volume equipment as `flow model`. This separates the basic conservation equations into two model types: the dynamic mass and energy balances are modeled in control volume models and the quasi steady state or dynamic momentum balance is modeled in flow models [39].

The `control volume` can be either lumped or discretized. The models are designed for system level simulation and are thus discretized in one dimension or even lumped parameter approximations [38]. Combining two `control volume` models without a `flow`

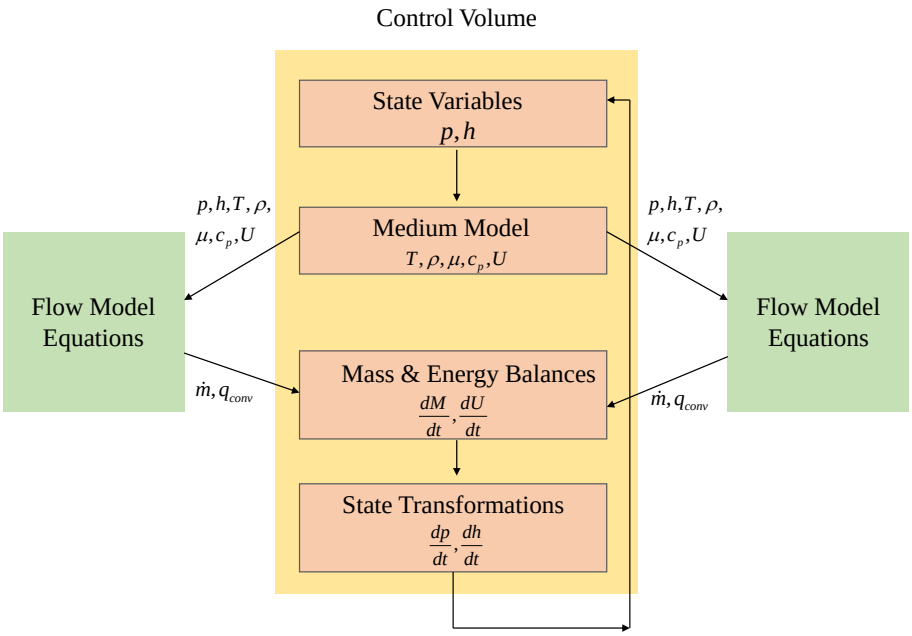

Figure 1.1: Sequence of Operation in a Typical Refrigerant Control Volume [48]

`model` in between leads to an index two differential algebraic equation (DAE) problem. In such cases, creating a unified `control volume` equivalent to the two separate `control volumes` is a simpler and better solution. Combination of two `flow models` can lead to a rather unpleasant non-linear system of equations. This is not a big problem but it reduces robustness unnecessarily [39]. For these reasons, a convention of alternating `flow model` and `control volume` models is followed. If necessary, two `flow models` can be coupled directly by including a zero volume `control volume` between the `flow models`.

The sequence of calculation which is determined automatically by the Dymola tool for such a system is as follows [49]:

1. Initial values of the state variables (p, h or p, T or p, ρ) are supplied by the user in initial equation.

2. Other thermodynamic properties are calculated using the medium model from the state variables.

3. The flow models use the value of these variables for evaluating the mass and energy flows. It accesses these variables through the connectors.

4. Mass and energy flows from the flow models are used to calculate the mass balances (dM) and energy balances (dU) in the control volumes.

5. State transformation is carried out to transform the time derivatives of total mass and internal energy (dM and dU) to time derivatives of state variables (p,h) using functions like *ddph* and *ddhp*.

6. The time derivatives of pressure and temperature are used for evaluating the new values of the states.

1.2.1.2 Stream Connectors

Modelica offers a very powerful software component model that is on par with hardware component systems in flexibility and reusability. Components have well-defined interfaces consisting of ports (refered to as `connectors` in Modelica terminology) to the external world. A component should be defined independently of the environment where it is used, which is essential for its reusability. This means that in the definition of the component, only local variables and connector variables can be used. No means of communication between a component and the rest of the system, apart from the connector is recommended [36].

```
connector FluidPort
  "Interface for quasi one-
dimensional fluid flow in a piping network (incompressible or compressible,
one or more phases, one or more substances)"

  replaceable package Medium = Modelica.Media.Interfaces.PartialMedium
    "Medium model" annotation (choicesAllMatching=true);

  flow Medium.MassFlowRate m_flow
    "Mass flow rate from the connection point into the component";
  Medium.AbsolutePressure p "Thermodynamic pressure in the connection point";
  stream Medium.SpecificEnthalpy h_outflow
    "Specific thermodynamic enthalpy close to the connection point if m_flow < 0";
  stream Medium.MassFraction Xi_outflow[Medium.nXi]
    "Independent mixture mass fractions m_i/m close to the connection point if m_flow < 0";
  stream Medium.ExtraProperty C_outflow[Medium.nC]
    "Properties c_i/m close to the connection point if m_flow < 0";
end FluidPort;
```

Figure 1.2: The FluidPort connector in Modelica Standard Library

`Modelica Standard Library` provides different kinds of connection variables to model connections for different physical domains. Connections between physical devices are generally treated with pairs of potential (equality) and flow (sum to zero) variables.

However for thermo-fluid systems, these two types of variables are not sufficient to describe in a numerically sound way the bi-directional flow of matter with convective transport of specific quantities, such as specific enthalpy and chemical composition. The values of these specific quantities are determined from the upstream side of the flow, i.e. they depend on the flow direction. When using connectors with only potential and flow variables, the corresponding models include non-linear systems of equations with Boolean unknowns for the flow directions and singularities around zero flow [50]. A third type of connector variable called `stream variable` was developed to overcome this shortcoming.

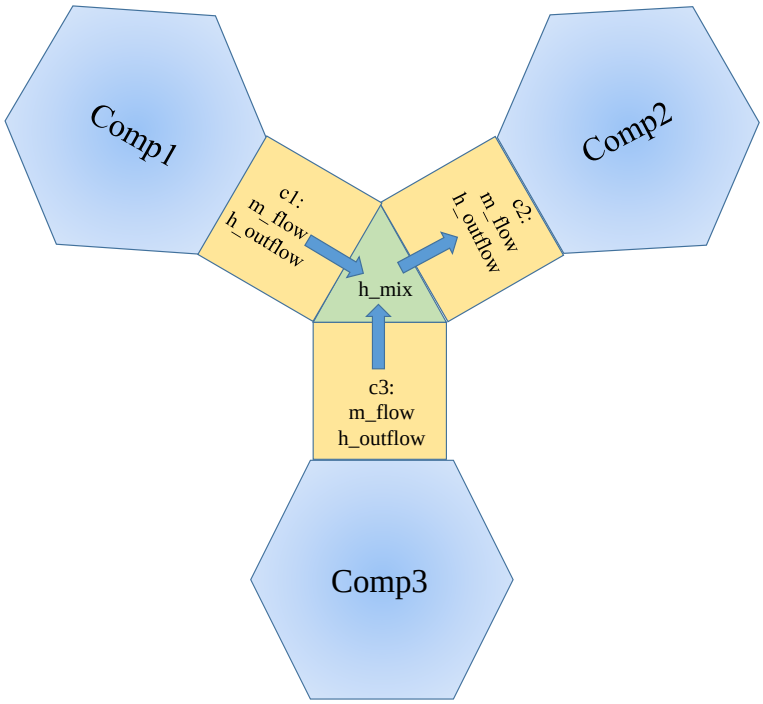

Figure 1.3: Connectors connecting three thermo-fluid components

A built-in operator `inStream`, which when applied to a stream variable in a stream connector returns its value close to the connection point provided that the associated mass flow rate is positive in the direction into the component. A built-in operator `actualStream`, which when applied to a stream variable returns its value close to the connection point regardless of the direction of the associated mass flow.

1.2.1.3 Current State of Art of Modeling VCC

The `ThermoFluid` library [37–41] provides base library for dynamic simulation of thermo-hydraulic processes. Pfafferott [43,44] used the models of the `ThermoFluid` library as a starting point for the development of additional component models to simulate mobile air conditioning system. This Modelica library called `ACLib` [51] was used to simulate mobile R134a and CO2 air conditioning systems. This was later used to in the design process of the `AirConditioning` library developed by Modelon AB and presented in [52]. The `AirConditioning` library is the currently most widely used Modelica library to simulate air-conditioning systems. The structure of components, however, is very complex in `AirConditioning` library due to extensive hierarchy from multiple inheritance and `TIL` library was developed with a structure that is simple to understand for students, developers and simulation specialists [46].

The `AirConditioning` Library is capable of handling both steady state and transient simulations. However, it was mainly developed for automotive air conditioning systems. For detailed modeling of building HVAC systems `CEEE Modelica Library` [47] has been developed. The library includes detailed finite volume based as well as moving boundary based heat exchanger models with capability to model frosting and defrosting.

In all these libraries, there are two commonly used heat exchanger modeling meth-

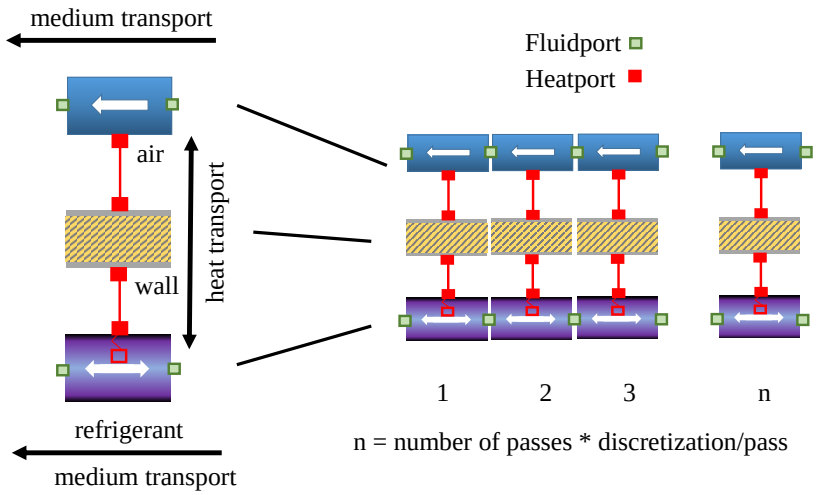

Figure 1.4: Object diagram of heat exchanger

ods: finite volume method (fixed control volumes independent of liquid phase) and moving boundary method (one control volume per phase of the refrigerant). Finite volume method based components allow a numerically robust simulation of thermo hydraulic systems including flow reversal [51] and render more accurate predictions in heat transfer and fluid flow phenomena [53]. The design of controls requires low order models and moving boundary models are more favorable for this purpose.

Figure 1.4 shows a model diagram of a heat exchanger. It comprises of three control volumes, one for each of air, metal (refrigerant tube and fins) and refrigerant. Heat conduction in the solid material is modeled one-dimensional and perpendicular to both fluids. Longitudinal conduction is neglected for efficiency reasons and because no significant loss in accuracy is expected [51]. Transient mass and energy storage is considered in the refrigerant and the metal control volumes but neglected

at the airside. The mass and specific heat capacity of the air are much smaller than that of the metal or the refrigerant. So, the airside control volume is modeled as quasi-steady.

1.2.1.4 Mass Conservation in Dynamic VCC Models

Many dynamic vapor compression system models demonstrate significant variations in the total system charge which does not correspond to observed behavior in experimental systems [54]. This is significant because the dynamics associated with variations in the cycle charge will be coupled to the other system dynamics and introduce aberrant behavior that would not be observed in experimental system. These mass variations are caused by interactions between the numerical behavior of the DAE solver and the thermodynamic properties of the refrigerant in the neighborhood of the saturated liquid line for the conventional choice of pressure and specific enthalpy as state variables [55].

Two-phase refrigerant flows experience large changes in density as the fluid passes from the liquid region into the two-phase region. These large changes in density can be seen in Figure 1.5. At the static quality of zero for the given pressure, it is evident that there is a discontinuous change in the derivative of density with respect to the static quality, and hence with respect to the mixture specific enthalpy. Integration errors that are added to the state variables located barely on the single phase side of the saturated liquid line can therefore cause the resulting refrigerant density to be calculated on the two-phase side of the saturated line [55].

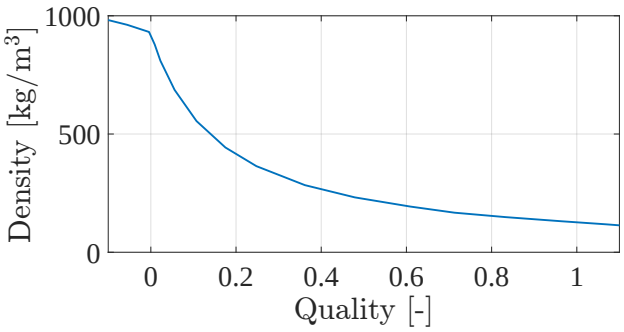

Figure 1.5: Refrigerant density of R410A as the static quality varies from a subcooled liquid to a superheated vapor at a pressure of 2850 kPa [55]

The total mass of the system is obtained by summing all of the masses for the individual control volumes in the pipe models.

The strong coupling between refrigerant mass and other system variables, such as pressures and specific enthalpies, will cause local disturbances to the refrigerant state to quickly propagate throughout the system. Small integration errors can thus accumulate quickly and lead to significant and unexpected changes in the total system mass.

An alternative choice of state variables can reduce these undesirable changes in the refrigerant mass. The selection of density (ρ) as state variable will allow the integrator to minimize the errors in the density directly rather than through ρ (p, h). By choosing p and ρ as state variables, the amplification of the errors observed in the density will be eliminated, resulting in a corresponding reduction in the variation of the total system mass.

However, the selection of density does impose additional costs upon the simulation. Perhaps the most significant of these is that the use of density as a state

variable will cause the solver to take smaller time steps because of large values of derivatives. Also the set of equations that needs to be solved now is non-linear [55].

Another alternative method for describing the dynamics of the differential control volume involves expanding the number of state variables to include pressure, specific enthalpy and density. While this approach does result in a larger number of state variables, it has the advantage of simultaneously minimizing the variations in system charge while enabling the use of pressure and specific enthalpy for calculating other refrigerant properties.

The problems associated with total charge estimation with pressure and enthalpy as state variables can also be minimized by increasing the solver tolerance from 1e-4 to 1e-6. The system simulation is the fastest with pressure and enthalpy as state variables and if the total system charge does not change appreciably with a high tolerance value, this selection should be preferred.

1.2.1.5 Non-homogeneous two-phase flow

The choice of flow model used to describe a vapor compression system is important because some of the systems equilibrium characteristics, such as its total mass inventory, are strongly related to the flow regime. One particularly common type of heterogeneous flow model is known as a slip-flow model, in which it is assumed that mass transfer across the phasic interface takes place without an accompanying momentum transfer. This model can be formulated as a set of equations describing the two-phase mixture with an extra set of closure relations to relate the different

phasic properties to each other and, consequently, is much simpler than a complete multi fluid model [56].

Bauer (1999) [57] developed two different slip-flow models for the dynamics of a evaporator, one of these models used a static relation to describe the interactions between the phases, while the second incorporated an innovative description of the mass, momentum, and energy transfer between the phases without developing a complete two-fluid model. The results from this work demonstrated that the homogeneous flow modeling approach was inadequate to describe the evaporators mass inventory and that the performances of the momentum balance with and without a momentum transfer across the two phase interface were comparable.

The slip-flow cycles simulated by Laughman et al.(2015) [56] had a total evaporator inventory that is 75-85% higher than the homogeneous flow cycle, although the cycles were all initialized at the same operating point. These differences in charge are part to the fact that the liquid phase velocity is much lower than the vapor phase velocity, causing the total residence time of the liquid in the heat exchangers to be much longer for the slip flow cycles than for the homogenous flow cycle.

The differences in charge between the cycles with the different flow assumptions are only relevant to the components with two-phase flows. The components in the cycle that have a single phase flow will have the same charge inventory. The mass inventory in the condenser is also similar, because much of the mass is contained in the sub-cooled section of the condenser and because the length of the two phase region in the condenser is shorter than it is in evaporator.

It is also interesting to note that the different slip-flow correlations correspond to different transient responses. Laughman et al.(2015) [56] found that the transient corresponding to the homogeneous flow assumption is much faster than both the experimental data and the comparable slip flow transients.

1.2.2 Thermosiphon Modeling

Two-phase thermosiphon is also a fairly commonly used thermo-fluid system. A brief review of the modeling effort is presented in this subsection.

The thermosiphon mechanism has been studied by researchers for the past 100 years, starting notably with Lord Rayleigh [58]. Dobran [59] provided the first comprehensive control volume (CV) based model to analyze the steady-state characteristics of a two-phase thermosiphon. Reed and Tien [60] advanced this work by including transient behaviors, analyzing dry-out and flooding. These models [59,60] were created for counter-current two-phase closed thermosiphons, which are essentially wick-less heat pipes. Examples of counter-current thermosiphon analysis can be found in several review articles [61–63]. The development of predictive tools for heat pipe technologies, such as a thermosiphon, remains an active field of research.

Industrial applications typically involve co-current two-phase loop thermosiphons (TPTL) due to their capability of transporting large heat quantities and less liquid-vapor interaction [64]. Several steady-state models are available in literature for TPTL [65–69]. The first model for such a thermosiphon based on the control volume approach for overall performance in transient operation was developed by Vincent

and Kok [64]. The model requires saturation temperature of the evaporator during its steady-state operation as an input and provides transient behavior for perturbations of a thermosiphon from that steady-state condition. Haider et al. (2002) [69] developed a more detailed Engineering Equation Solver (EES) [70] based steady-state model for a co-current two-phase thermosiphon with equations for the riser and downcomer, in addition to the evaporator and condenser. The connecting tubes between the evaporator and condenser, where either the refrigerant liquid trickles down or the refrigerant vapor rises, are called downcomer and riser, respectively. The model involves two iterations: the first calculates total two-phase mass flow rate using overall momentum balance, and the second solves the mass and energy balances on the evaporator and condenser.

Khodabandeh [65, 66] conducted a more comprehensive study with a similar steady-state EES model to provide insights on the accuracy of various pressure drop and heat transfer correlations in predicting the performance of the electronic cooling application. A more sophisticated MATLAB [71] based steady-state model that accounts for differences between fully liquid and partially liquid downcomers was modeled by Zhang et al. (2015) [67]. A fully explicit distributed parameter model was developed by Dobson and Ruppersberg [72] for transient modeling and validation of a thermosiphon used for cooling the concrete containment structure surrounding a nuclear reactor. Most recently, a transient one-dimensional flow model for TPLT considering a two-phase mixture in both mechanical and thermal equilibrium was developed by Bodjona et al. (2017) [73]. This two-phase flow model can describe various states of refrigerant and compute phase transitions. However,

validation of the model is not presented, and the applicability of the model to a practical setup requires additional study. Furthermore, these models Dobson and Ruppersberg (2007) [72] and Bodjona et al. (2017) [73] use transient profiles for the heat input, limiting analysis only to the refrigerant side. Integration of a PCM within a heat pipe is modeled by Srikanth et al. (2016) [74] using CFD. However, this framework is not suitable to capture variation in refrigerant properties.

1.2.3 Phase Change Materials

Phase change materials are increasingly being used in buildings to reduce peak energy consumption. They provide potential for offsetting demand and generation of energy, preventing addition of several power plants if implemented on a wide-scale. This thesis explores integration of phase change materials with vapor compression system and thermosiphon. A brief literature review on phase change materials is provided in this section.

Thermal energy storage (TES) with PCM has been a heavily researched topic for the past 40 years. It has a global appeal as it deals with energy saving, efficient and rational use of available resources and optimum use of renewable energies [75]. As a result, a very rich and varied experimental knowledge [8, 76–80] in applications spanning from small TES for battery cooling to large scale TES in power plants is available.

1.2.3.1 Numerical Modeling

Predicting the melting and solidification of PCM belongs to a class of mathematical problems called the moving boundary problem. It is especially complicated due to the fact that the position of the solid-liquid boundary is not known a priori and forms part of the solution [75]. Analytical solutions are not available except for very few geometric configurations, which are mostly ideal cases. As a result, a very wide range of numerical methods have been developed by researchers over the years for modeling the phase change behavior in PCM and have been summarized by Dutil et al. (2011) [81], Hu and Argyropoulos (1996) [82]. These numerical methods can be classified roughly into the enthalpy method and the effective heat capacity method [83]. Some of the common assumptions adopted by researchers for simplification of the mathematics of the phase-change process are ignoring effects of natural convection [84, 85], isothermal phase change [84–87], constant thermophysical properties for each phase [84, 86, 87], ignoring the density differences between the solid and liquid phases [84, 85] and using symmetry for simplification of control volume [86,88]. When modeling phase change with a temperature glide, various equations [83, 89–91] for estimating the specific heat capacity in the two-phase region have been used. Very recently, Trník et al. (2017) [92] have attempted to model the specific heat capacity behavior in the two-phase region using molecular thermodynamics principles.

1.2.3.2 3-D analysis

Due to the additional mathematical complexity with 3-D conservation equations, most of the numerical studies in literature are available for simple geometries like cylindrical [86, 87, 93–95] or rectangular cross-sections [96–101], which may be modeled with either 1-D or 2-D control volumes. Few numerical predictions of 3-D melting have been reported and, as pointed out by Sharifi et al. (2013) [102], detailed experimental measurements corresponding to 3-D melting and solidification are sparse. With the advances in computational resources and ease of setting up simulations with supporting software, computational fluid dynamics (CFD) is increasingly being used for 3-D PCM analysis.

One of the interesting cases for 3-D PCM analysis involves helical coiled tubes based TES (HC-TES). HC-TES are more compact and have better heat transfer performance than straight tube based TES. This is due to the low values of thermal conductivities associated with PCM. Helical configuration allows increase in surface area for a fixed height of TES and better penetration into the PCM. Experimental evaluations of HC-TES are presented by [103–106]. Numerical research for HC-TES is very sparse. Yang et al. (2017) [107] developed CFD-based numerical models validated with experimental measurements for dynamic melting of PCM in helical coil TES. These experimental and CFD-based researches focus only on the HC-TES and not for the whole system, to which these HC-TES are integrated. Very few studies consider modeling the refrigerant behavior in PCM-HX and the most common approach is to provide an isothermal or constant-heat flux boundary con-

dition to the PCM control volume. The refrigerant side of the PCM-HX used by El Qarnia (2009) [86] and Bakhshipour et al. (2017) [87] is liquid, thus enabling the assumption of incompressible flow and a relatively simple model. It is necessary to point out that the geometries modeled by El Qarnia (2009) [86] and Bakhshipour et al. (2017) [87] are cylindrical enabling them to develop a 2D model for the PCM cross-section.

1.2.3.3 System simulation

Modeling or testing of TES at a component level leads to its improved sub-system performance. However, a dynamic model of the entire system (of which TES is a sub-system) provides several additional benefits like optimization of the entire operation, development of controls, understanding the safety of operation, replacement of time and cost intensive experiments for parametric study. System models magnify human intuition by enabling development of hitherto unseen system behavior patterns, and thus reduce development time and production costs with increased product quality and a more reliable system operation. Sub-system models are modeled using a very high level of detail. Using the same sub-system model to develop a system model will lead to very large complexity, which may not be solved by numerical solvers and significant computational effort [108]. So it is necessary to find a balance between accuracy and level of detail in a system simulation.

The system-level models involving TES in literature are used only for qualitative study and lack detailed validation. Azzouz et al. (2008) [85] modeled a dynamic

model of VCC with a PCM integrated with its evaporator in a domestic refrigerator. The model uses a simplified dynamic model with a rectangular slab PCM, which is validated by comparison with experimental measurements obtained for a refrigerator without PCM and then used to obtain qualitative trends after including PCM. Leonhardt and Müller [90] describe modeling and simulation of a TES integrated in a heat pump system. The PCM model ignores effects of natural convection and is used only for qualitative analysis of system performance. The heat pump model is implemented as a black box model. Another system level model with PCM is developed by Buschle et al. (2006) [91] for qualitative analysis of steam accumulator in power plant application .

1.2.4 Personal Conditioning Systems

Hoyt et al. (2015) [109] demonstrated the energy savings potential from extending building thermostat set-points. They concluded that if it were possible to relax the temperature set-point in either the hot or cold direction, total HVAC energy is reduced at a rate of 10% per °C. To enable expansion of building set-point temperatures without affecting occupant thermal comfort, one option is to provide supplementary Personal Conditioning System (PCS), which consumes significantly lower energy. PCS offers dual benefits of energy saving and increased comfort [110]. Energy is used to modify the local thermal envelope around the human body rather than the building, thus allowing the thermostat to be relaxed without compromising the occupant comfort. This was confirmed in the experimental studies carried out

by several researchers with human subjects using their respective PCS [111–113]. By offering personalized comfort, PCS are able to deliver comfort to every individual rather than the conventional HVAC systems which cater to the average population. Percentage satisfaction as high as 100% has been reported in the literature with well-designed PCS [114]. Some additional benefits of PCS are lower capital installation costs and ease of implementation when compared to novel HVAC solutions.

Due to these benefits, a large number of PCS exist which are summarized in the review articles by Zhang et al. (2015) [110], Veselý and Zeiler (2014) [115].

Task ambient conditioning systems [114, 116–118] are typically space conditioning systems, typically installed in office buildings. The occupants can control the thermal conditions in the small regions surrounding them. Recently, the application of these systems is being explored in bedrooms to increase thermal comfort in sleeping environment and at the same time reduce energy use [116, 119]. There is a lot of variation in design of these systems, but usually they consist of air nozzles to supply air to the upper body and a radiant panel for heating the legs. They provide conditioning only to the limited space surrounding the office desk towards which the air nozzles and radiant panel are directed. Air nozzles pull air from underfloor plenum or ceiling vertical ducts leading to retrofitting costs.

In an evaporative cooling system for air conditioning [120, 121], the air has a direct contact with water. The evaporation of water causes cooling and humidification simultaneously. However, these technologies increase the indoor humidity leading to additional loads on the building HVAC. However, these technologies are excellent for hot and dry climates.

Cooled chairs [122–124] is another type of PCS, capable of providing improved comfort. They may include fans to provide ventilation [123] or thermo-electric devices providing heating and cooling in the surface of the chair [122]. The chairs demonstrated ability to provide thermal comfort at ambient temperatures as high as 29-30°C [122, 123]. However, the occupant needs to be seated in the chair to feel comfortable.

Personal cooling garments [125–127] have been effective in providing comfort in hot environments and have been used in special fields like military training, firefighting, medical operations and sports. They may use liquid cooling [128, 129], air cooling [130], phase change material [127] or a combination of the above methods [125]. For formal office wear, however, they are inappropriate because they are bulky, heavy and have poor ergonomics. The liquid cooled and air cooled vests have other drawbacks like high cost, complexity and non-portability due to the refrigeration system [125].

Thus, despite great energy savings potential the current PCS, they do not have much market value due to factors such as high cost, limited range of comfort, poor thermal performance, low energy efficiency and poor aesthetics. Consequently, except for common desk and ceiling fans, most of these are not commercially available [110]. Except for the cooling jacket, the other PCS, target the occupants' workstations and may not cover all the spaces an occupant might visit or pass through during the day. If the occupant divides his/her time between two locations, there is a need to install two PCS.

1.2.5 Refrigerant Migration

The HVAC systems are normally sized for peak load conditions. These systems operate under off-peak conditions most of the time by on-off cycling. The average efficiency of the system during cycling is lower due to transient losses [131]. Consequently, cyclic test procedures have been conceived to provide credit to the designs that minimize cyclic losses. The relationship between cyclic refrigerant migration and cyclic loss for an HVAC system has been the focus of research for past 30 years some of which are summarized in Table 1.1.

Table 1.1: Cyclic Losses from Refrigerant Migration

Researcher	System	Degradation
Parkens et al. (1976) [132]	Split AC	25-35% reduction in capacity
Wang & Wu (1990) [133]	Small AC	4% reduction in energy consumption
Tassou & Votsis (1992) [134]	Air to Water Heat Pump	11% reduction in COP
Janssen et al. (1992) [135]	Domestic Refrigerator	10-18% losses from cycling
Björk & Palm (2006) [136]	Domestic Refrigerator	11% loss in capacity, 9% in efficiency
Kapadia et al. (2009) [31]	Split AC	18.5 % in capacity
Bagarella et al. (2013) [137]	Air to Water Heat Pump	13% reduction in COP

Kapadia et al. (2009) [31] separated the losses in capacity into two portions: Losses from refrigerant migration contributed to 30% of the cyclic losses while the remaining 70% were from the thermal inertia.

Parkens et al. (1976) [132] were the first to recognize that the the response

of the system at startup and the cycling rate of the equipment could be combined to form a part load correlation. They used this concept to develop the degradation coefficient (C_d) used in the SEER rating procedure to predict the part load effects.

The earliest researchers focused on experimental results to provide insights into refrigerant migration. Mulroy and Didion (1985) [138] conducted experiments to show that during start-up more charge was in the low pressure components, which subsequently migrated to the high pressure components during steady-state operation. More specifically, at the end of the off-cycle, 80% of the total charge was found in the low pressure components - evaporator, vapor line and accumulator. During steady state operation 83% of the total charge was found in the high pressure components - condenser and liquid line.

Table 1.2: Refrigerant Charge Distribution in HVAC Systems

Researcher	System	On Cycle	Off Cycle
Mulroy & Didion [138]	Automotive AC	17%	80%
Belth et al. [139]	Residential Heat Pump	51%	80%
Peuker & Hrnjak [140]	Split AC	42%	89%
Li et al. [141]	Split AC	40%	83%

Regression analysis was carried out on the experimental data to obtain curve fits for the cooling capacity during start-up condition. Similar, studies were conducted by Murphy and Goldschmidt (1979) [142], Kim and Bullard (2001) [143] and Peuker and Hrnjak (2008) [140]. The details of the curve-fits developed by these researchers can be found in the thesis of Peuker [144]. These curve-fits require a sin-

gle or multiple experimentally derived time-constants are parameters to match their respective data. As pointed out in Mulroy and Didion (1985) [138], even though the time constant value is the best representative of the state of the art, it is not possible to determine the range and median values without conducting further experiments. Since, the curve-fits are very much model specific, they do not reduce any experimental burden.

Due to the advancement of computing facilities, it has become possible to model complex systems. There are several publications on transient modeling of vapor compression cycles, but few results are available concerning the modeling of refrigerant migration behavior.

Murphy and Goldschmidt (1985,1986) [145, 146] present simulated refrigerant migration results in some partial system components during start-up and shut-down transients. Ozyurt and Egrican (2010) [147] steady state refrigerant mass distribution of the system model with the experimental data.

Li et al (2011) [148] presented the first refrigerant mass migration prediction in a validated dynamic system model. However, the focus of their research was on development of controls and hence they employed moving boundary models [MBM]. MBM utilize lumped characteristics for each of the control volumes such as single void fraction for the entire two phase section, which could lead to lower accuracy [149]. It is necessary to identify beforehand what possible phase region combinations can exist logically in the heat exchanger and the manner of their transition. As pointed out it Qiao (2014) [47], they employ huge look-up tables for correlating mean void fraction, the refrigerant pressure and the outlet vapor qual-

ity before conducting the simulation. This makes the simulation very application specific. Another disadvantage of moving boundary models is that the mode transitions are such that phase boundaries enter or leave the heat exchanger only from the refrigerant outlet end. The model cannot handle a situation where the phase boundary enters or leaves from the refrigerant inlet end [149]. Thus, phenomena like refrigerant leakage through compressor cannot be modeled using the approach. It is also not possible to model complex refrigerant circuitry on the air-side using MBM with accuracy.

Distributed parameter model permit modeling of space-time variation in properties. It is capable of accounting for the complex tube circuitry of the heat exchanger. A first principles based model for the refrigerant migration dynamics will enable accurate modeling of the complex phenomena associated with the transient behavior of vapor compression cycles in cyclic operation. The insights are expected to aid the improvement of HVAC equipment leading to better cyclic performance.

1.2.6 Current methods for estimating HVAC cyclic performance

The DOE and ASHRAE standards for evaluation of part load performance are based on the experimental work [150] conducted at National Institute of Standards and Technology (then called National Bureau of Standards). The methodology to estimate cyclic degradation is given in standards ANSI/AHRI Standard 210/240-2008 [32] & ASHRAE 116-2010 [151]. The indoor and outdoor ambient conditions are, for a large fraction of the time in regions throughout US, such that an air condi-

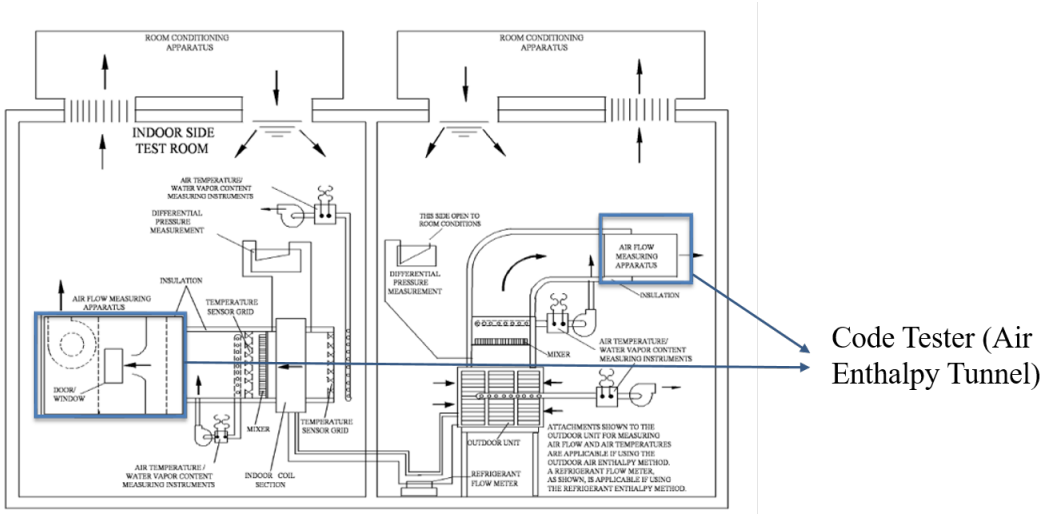

Figure 1.6: Schematic of Environment Chamber showing Code Tester [153]

tioning unit must operate cyclically and with a wet evaporator coil [150]. However, cycling a unit under wet-coil conditions presents both accuracy and redundancy problems due to long time constants of the wet-bulb instrumentation. Both room control and indoor air stream enthalpy measurements are unreliable under periodic conditions [152].

As a result, the cyclic wet coil tests are replaced by simpler and more accurate dry coil tests. Equation 1.1 based on experimental observations [152] is used for evaluation of part load wet coil performance.

$$\frac{COP_{cyc}}{COP_{ss}}\bigg|_{\substack{dry\\coil}} = \frac{COP_{cyc}}{COP_{ss}}\bigg|_{\substack{wet\\coil}} \tag{1.1}$$

The testing of HVAC equipment is carried out in environmental chambers (Figure 1.6). Typically, there are two chambers: one for the indoor unit and the other for outdoor unit. Four tests A, B, C and D are conducted as per ANSI/AHRI

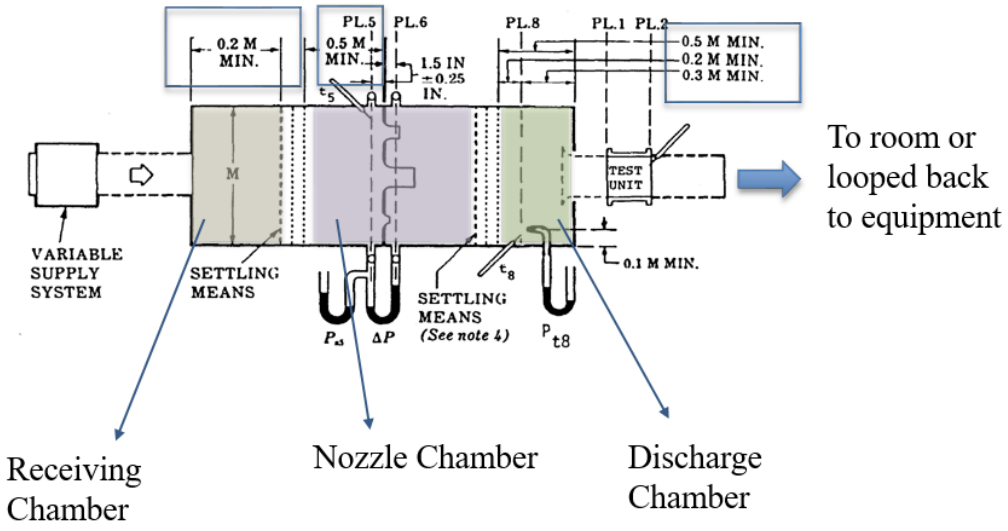

Figure 1.7: Schematic of a Code Tester [154]

Standard 210/240-2008 [32]. Cyclic degradation coefficient is calculated from the cooling capacity of these four tests. The cooling capacity calculation is explained in ASHRAE 37-2009 [153] with the testing equipment description in ASHRAE Standard 41.2-1987 (RA 92) [154].

The airflow measurements involve flow measurement chambers, air flow generating devices, dampers and mixers. ASHRAE Standard 41.2-1987 (RA 92) does not specify the material to be used for each of these components. Only the minimum dimensions of chamber are specified (See Figure 1.7). This permits large variation in the thermal mass of the setup, which in turns affects the air-side cooling capacity. The transient D-test is especially going to have deviations from the variations in the thermal mass of the testing equipment. There are no studies available on the influence of Code Tester (air enthalpy tunnel) on the cyclic performance of the

HVAC unit being tested.

Parken et al. (1976) [132] introduced the non-dimensional forms of efficiency (called part load factor, PLF) and cyclic cooling capacity (called cooling load factor, CLF) as per Equations (1.2) and (1.3).

$$PLF = \frac{COP_{cyc,dry}}{COP_{ss,dry}} \tag{1.2}$$

$$CLF = \frac{\int_0^{t_o} \dot{Q}_{cyc,dry} dt}{\dot{Q}_{ss,dry} t_c} \tag{1.3}$$

The PLF and CLF were related by a linear fit even though there were variations in the PLF data due to the cycling rate, which led to the development of the degradation coefficient, Cd, defined by Equation(1.4). The part load factor in Equation (1.5) [PLF (0.5)] is evaluated for a CLF of 0.5 to estimate the SEER.

$$C_d = \frac{1 - PLF}{1 - CLF} \tag{1.4}$$

This SEER evaluation procedure is based on experimental data available at that time without any significant theoretical research. Starting from Murphy & Goldschmidt [142], Goldschmidt et al. [155] to ONeal & Katipamula [156], in efforts spanning well over a decade, several researchers conducted extensive experimental

and theoretical investigations to understand the validity of the assumptions made in the development of the procedure.

$$SEER = PLF(0.5) * EER_B \tag{1.5}$$

Single time constant models, in which the start-up cooling capacity of the air conditioning system is modeled using an exponential function with the time constant, were used by Katipamula & ONeal (1991) [157], ONeal & Katipamula (1993) [156] to show that the relationship between PLF and CLF is not linear. Henderson et al. [158] realized that use of Cd to evaluate PLF (by substitution in Equation (1.4)) is not accurate and implemented alternate empirical equation in DOE-2, which is a building energy simulation program. Experiments conducted by Bettanini et al. (2003) [159] to evaluate the use of Cd to evaluate PLF from Equation (1.4), show that this approximation is not acceptable. They propose a new parameter Z, which is the ratio of the electric power consumption at part load working condition to the one at full capacity to evaluate PLF. Italian standard UNI 10963 also identifies the shortcoming of Cd and uses the Z-parameter method to evaluate PLF Bettanini et al. (2003) [159]. However, the ISO Standard 16358-1 [160] still uses Cd and defines 0.25 as default value.

The single-time-constant model assumes that the shutdown transients have no direct impact on the startup characteristics. The startup losses can be better predicted by two-time-constant models Mulroy & Didion (1985) [138], with one time

constant capturing the capacity delay due to the mass of the heat exchanger, while the second time constant capturing the delay in reaching steady state refrigerant distribution from the off-cycle refrigerant distribution. Sigmoid and polynomial functions for startup have been used by Fuentes et al.(2016) [161]. However, the behavior of PLF and CLF obtained by integrating these functions has not been investigated.

The heat losses to the test setup have not been considered by any of these researchers. AHRI Standard 210/240 (2017) [162] as well as ASHRAE Standard 116 (2010) [151] recognize the contribution of the code tester in the measured cyclic cooling capacity by introducing a correction procedure. For the discussion of the chapter, since the focus is on air-conditioners, we will focus only on the indoor room apparatus in laboratory testing of split air conditioners. The method is described in the operation manual of AHRI Standard 210/240 (2017) and is summarized here. An electric heater is used as the source for integrated measured capacity and is cycled every 6 minutes with alternating on and off cycles. Ten on-off cycles are carried out over two-hour duration with a fixed airflow of 1200 cfm (0.566 $m^3 s^{-1}$). The temperature at the location of highest thermal mass (typically, the mixer) is measured at the start and end of the off cycle. For the discussion in this section, it will be assumed that this assumption is valid.

The average value of integrated airside capacity ($q_{ts,avg}$) evaluated as per ASHRAE Standard 116 (2010) [151] from last 6 to 8 cycles is calculated using Equation (1.6).

$$q_{ts,avg} = \bar{m}\bar{c}\left(\frac{(\Delta T_1)_{off}}{t_{off}}\right) \tag{1.6}$$

The integrated capacity ($q\prime$) is corrected using the thermal inertia term calculated from Equation (1.6) as shown in Equation (1.7).

$$q = q_{ts,avg}\bar{m}\bar{c}(\Delta T_1)_{off} \tag{1.7}$$

The temperature difference at the beginning and end of either the off cycle is used in Equation (1.6) while that during the on time during the cyclic D-Test (Equation (1.8)) for the mixer.

$$q_{ts} = \int_{off} \dot{Q}dt = \sum_{n=1}^{n} \bar{m}\bar{c}(\Delta T_i)_{off} \tag{1.8}$$

The dampers that circulate air into the code tester may have a different cycling time than the compressor and in such cases, the integration time should be taken from damper cycling. However, this is much closer to the on-cycle time in D-Test and so it is assumed equal in Equation (1.8).

$$\bar{m}\bar{c} = \bar{m}_1\bar{c}_1 + \sum_{n=1}^{n} \bar{m}_i\bar{c}_i\left(\frac{(\Delta T_i)_{off}}{(\Delta T_1)_{off}}\right) \tag{1.9}$$

In the real case, the q_{ts} term should involve heat transfer from all the regions of the code tester. If mixer has the higher thermal mass for a code tester with

n regions arranged in descending order of thermal mass, the thermal inertia term evaluated in Equation (1.6) is given by Equation (1.9). The standard, thus, ignores the second term on the right-hand side of Equation (1.9). It has been observed that this assumption leads to under prediction of thermal inertia effects from a code tester (by as much as 70% as will be shown later), and is one of the reasons for the differences in measured values of Cd for the same system when tested with different code testers.

1.3 Objectives

The thesis discusses modeling strategies for system simulation of complex two-phase refrigerant systems integrated with different thermal masses. This generic modeling framework is applied to improve cyclic performance of such systems. The insights from the thesis are expected to reduce energy consumption for space heating and cooling of buildings.

1. Investigate the influence of PCM on different thermo-fluid systems
    - Water systems, vapor compression systems
    - PCM-heat driven two-phase thermosiphon
2. Model dynamic vapor compression system with thermal inertia of code tester
    - Develop modeling framework to simulate cyclic test
    - Simulate refrigerant migration dynamics
3. Quantify code tester thermal inertia effect on cycling of air conditioner

- Derive equation to evaluate cyclic performance of air conditioner independent of code tester
- Identify influence of design and operation parameters of a code tester on cyclic performance of air conditioner

1.4 Thesis Outline

Chapters 2 to 4 are related to the first objective. Influence of PCM on different thermo-fluid systems is investigated in the context of a personal conditioning system. Experimental data for Roving Comforter (RoCo) is used for validation. RoCo uses VCC to deliver cooling to the occupants and stores waste heat from the condenser into a PCM battery. Thermosiphon operation is used to recharge this PCM battery. Multi-physics modeling of both charge and recharge operations are developed to create a platform for modeling any use-case scenario of the device. An optimization study with various PCM is discussed to understand the influence on performance of VCC.

Chapters 5 and 6 pertain to the second and third objectives. Dynamic modeling of cyclic performance of air-conditioner placed inside an environment chamber is developed and validated with experimental data. Extent of effect of testing equipment on the tested unit are quantified to develop best practices for testing.

Chapter 2: Portable Personal Conditioning Devices

As discussed in Chapter 1, despite the great energy saving potential, the current Personal Conditioning Systems (PCS) do not have much market value due to a combination of factors such as high cost, limited range of comfort, poor thermal performance, low energy efficiency and poor aesthetics. Consequently, except for common desk and ceiling fans, most of these are not commercially available [110]. Except for the cooling jacket, the other PCS, target the occupants' workstations and may not cover all the spaces an occupant might visit or pass through during the day. If the occupant divides his/her time between two locations, there is a need to install two PCS.

A Portable PCS (PPCS) is a personal attendant for thermal comfort and can deliver cooling through robotically-controlled air nozzles. A conceptual PPCS in operation is shown in Figure 2.1. It enables buildings to relax their thermostat by up to 4°F (2.2°C) and provides similar, if not better, thermal comfort with these new temperature settings in a cost-effective and energy efficient manner, leading to energy savings in the range of 10 to 30% depending on climate conditions. Thus, it addresses the issues of current PCS in that it does not require any retrofit, comfort range is not limited to any particular spot and thermal loads on the building do not

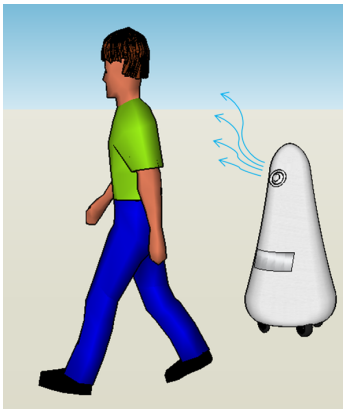

Figure 2.1: Portable Personal Conditioning System in Operation

increase.

This chapter presents four cooling systems (see Figure 2.2), which can be integrated on a robotic platform to function as a portable cooling device and compares their performance through multi-physics modeling. Modelica [163] is used for developing the models due to its ability to model equations from different physical domains, object-oriented programming and acausal modeling capabilities with well-supported libraries permitting re-usability of components.

2.1 Multi-physics Modeling of PPCS

A portable cooling device needs to be both affordable and energy efficient. The four cooling systems considered are modeled for their thermodynamic behavior, weight and battery consumption to understand the trade-offs involved therein. Vapor compression cycle is the predominant cooling technology used currently and a PPCS based on it is shown in the top left schematic of Figure 2.2 (labeled as VCS). In the United States, buildings are typically conditioned using chillers, and

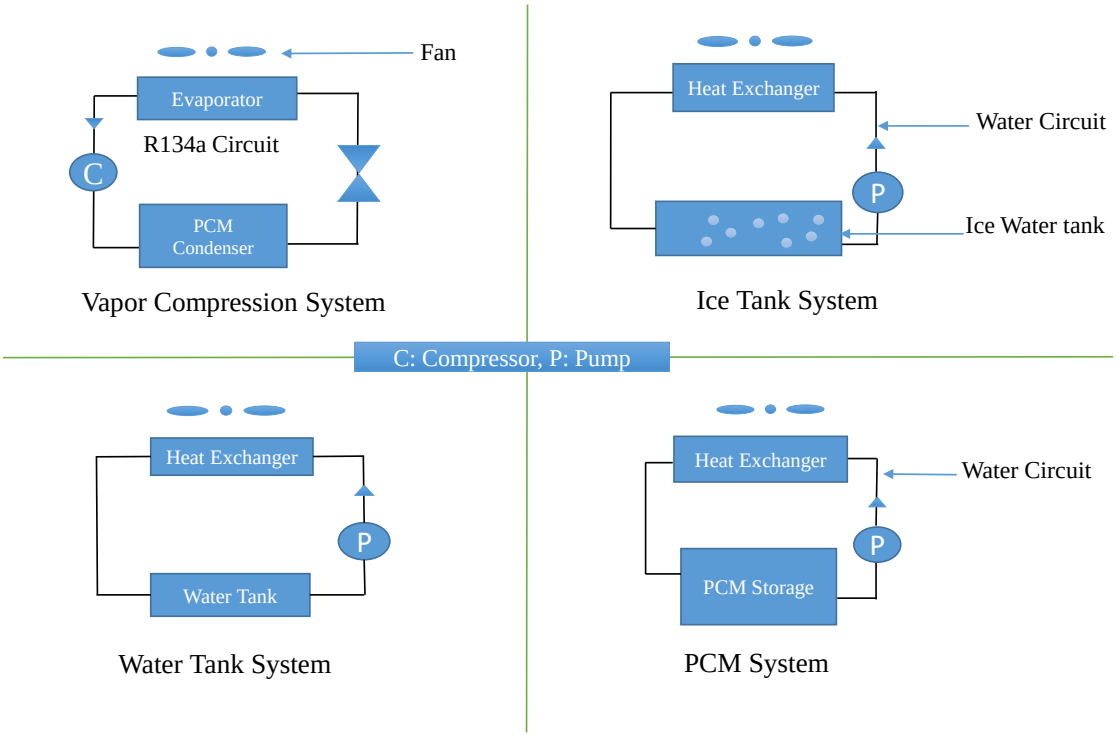

Figure 2.2: Schematics of the four cooling systems compared

therefore, have easy access to chilled water. Hence, a system which uses this water to deliver comfort is conceptualized and described as Water Tank System (WTS). This system is expected to be very cost-effective compared to VCS. Ice stores heat by phase change and results in a compact thermal storage. A system which uses ice to deliver comfort is also considered and is referred to as Ice Tank System (ITS). Phase Change Material (PCM) also has good latent heat capacity and can have a melting temperature higher than ice. A system using PCM at a melting temperature higher than ice may require lower energy for recharging. So, a fourth system based on PCM storage and water loop is considered and referred to as PCM system (PCMS).

The three water-based systems (Water Tank System, Ice Tank System and

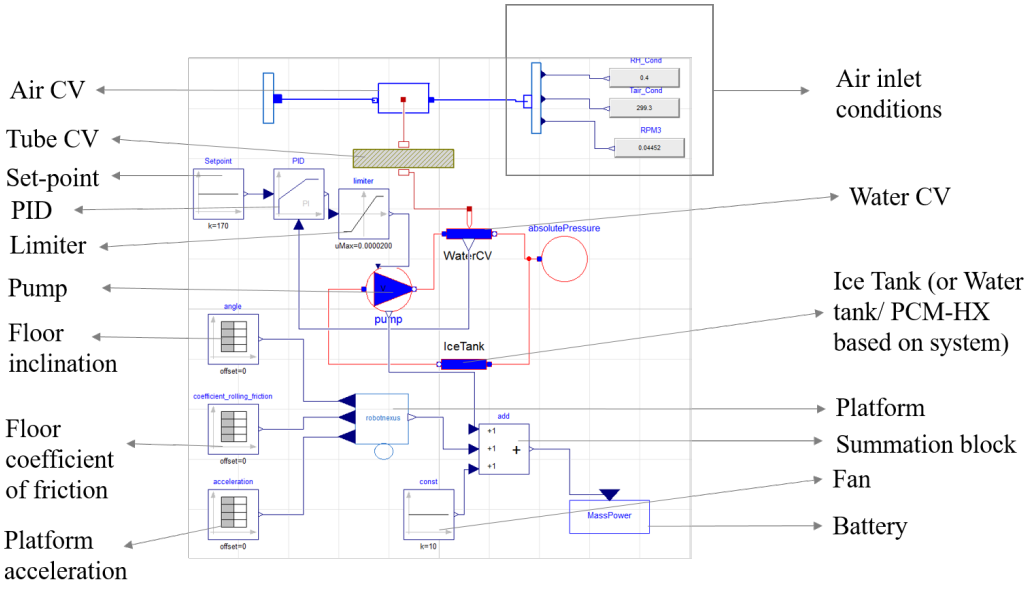

Figure 2.3: Model of Ice Tank System

PCM System) are modeled using the components available from the `FluidHeatFlow` package of `Modelica Standard Library` [164], while the VCS is modeled using the `CEEE Modelica Library` (CML) developed by Qiao et al. (2015) [165].

The system simulation schematic with all the components for ITS is shown in Figure 2.3. The model includes components for transient modeling of heat transfer, motion and battery, leading to a multiphysics simulation. The combination of the tube CV, air CV and water CV models the Air to Water Heat Exchanger (AWHX) discussed in Section 2.1.2.

A PID-controlled pump adjusts the water mass flow rate in the circuit to maintain constant heat exchanger cooling capacity. The AWHX cooling capacity is fed to the PID block, which compares this value with the set-point to regulate the volume flow rate from the pump to achieve cooling capacity. A limiter block is placed after the PID block to ensure that the PID block does not provide non-physical output values.

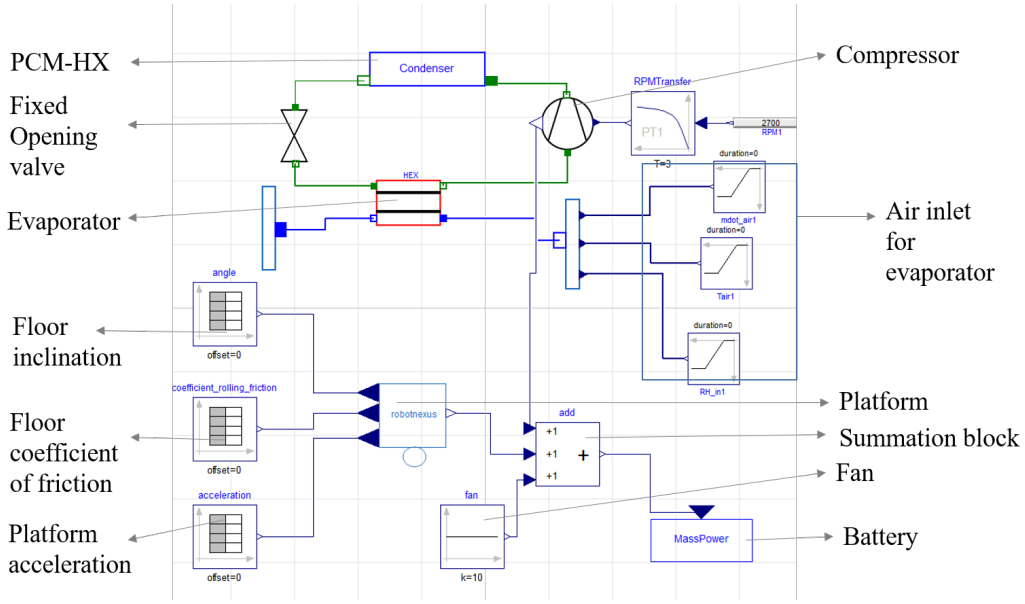

Figure 2.4: Model of Vapor Compression System

For brevity, model diagrams of WTS and PCMS are not included. Their models are similar to ITS model with only the ice tank being replaced by water tank or PCM-HX, respectively. The power consumed by the pump and robotic platform is added to a constant power draw representing the fan power and fed as an input to the battery leading to a multi-physics simulation for all the systems.

Figure 2.4 shows the model for VCS. It involves evaporator, compressor, fixed opening valve and PCM-HX operating as a condenser. The power consumption from the compressor is fed to the summation block of power consumption that is fed to the battery. The components required for modeling the four systems, which are developed specifically for this research are discussed in the following subsections.

2.1.1 PCM Heat Exchanger

The PCM heat exchanger (PCM-HX) is used in two systems: VCS and PCMS. A different PCM is used in each system.

PCM-HX is modeled with three control volumes (CV): PCM, refrigerant tubing, and refrigerant. These control volumes are connected by a `HeatPort` interface, which is the standard connector for heat transfer in the `Modelica Standard Library`. Contact resistance between the refrigerant tube and PCM is neglected. For the VCS, the refrigerant control volume is two-phase control volume and for the PCMS it is single-phase water control volume. The PCM and refrigerant tubing CV are the same for the two heat exchangers. This is a good example of the model re-usability aspect that makes Modelica very convenient for system modeling.

The melting and solidification processes are especially complicated due to the fact that the solid-liquid boundary moves depending on the rate at which latent heat is absorbed or lost at the boundary. So, the position of the boundary is not known a priori and forms part of the solution [75]. The heat transfer during PCM phase change is affected by varying effects of conduction and natural convection, which depend on the amount of PCM that has melted [96, 166]. Modeling of these effects requires three-dimensional modeling of the separate velocity flows of both phases, which heavily depends upon the geometry of PCM-HX.

For the conceptual nature of the present chapter, the model assumes that the dominant mode of heat transfer is conduction in the radial direction. The PCM-HX is modeled as a straight refrigerant tube surrounded by PCM (See Figure 2.5). Cylindrical co-ordinate system with finite volume discretization along the radial direction is used with a fixed grid.

The PCM CV is discretized into 10 finite volumes. The PCM melting is then solved using the enthalpy method for Stefan problems in one dimension as highlighted in Alexiades and Solomon (1993) [167]. Latent heat is released at a fixed phase change temperature, i.e. the temperature glide is ignored. The density of both solid and liquid phases is assumed constant to avoid movement of material during phase change. As discussed in Alexiades and Solomon (1993) [167], since density differences are typically less than 10%, the error arising from this assumption is not significant.

By defining, E as the energy density (per unit volume), $-\vec{q} \cdot \vec{n}$ is the heat flux into the volume V_j with surface area S, $\vec{n}$ being the outgoing normal to ∂V, we obtain:

$$\int_t^{t+\Delta t} \frac{\partial}{\partial t} \left(\int_V E dV \right) dt = \int_t^{t+\Delta t} \int_{\partial V} -\vec{q''} \cdot \vec{n} \, dS \, dt \tag{2.1}$$

Ideal heat transfer is assumed at the inner radius, r_i, of the PCM CV between the PCM and refrigerant tube. The outer radius of the PCM block, r_o, of the PCM CV is assumed to be fully adiabatic. The boundary condition equations for the PCM CV are:

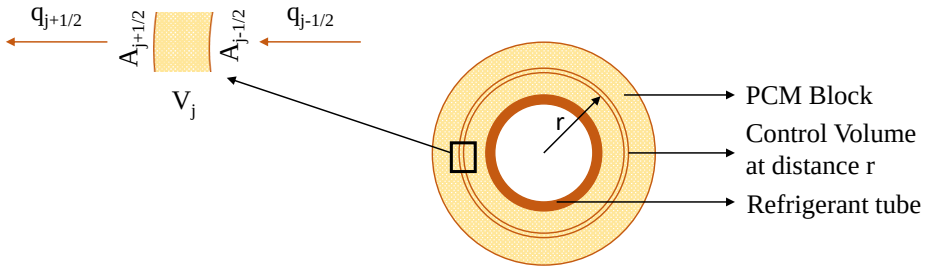

Figure 2.5: Discretization of PCM Control Volume

$$T\left(r_i, t\right) = T_{tube} \tag{2.2}$$

$$\frac{\partial}{\partial r}\left(T\left(r_o, t\right)\right) = 0 \tag{2.3}$$

The temperature at various grid points of the PCM is initialized to ambient temperature.

Equation (2.1) can be discretized as:

$$\frac{dE_j}{dt} = \frac{1}{\Delta V_j}\left(q''^k_{j-\frac{1}{2}} A_{j-\frac{1}{2}} - q''^k_{j+\frac{1}{2}} A_{j+\frac{1}{2}}\right) \tag{2.4}$$

The location of the grid points marked by indices j is shown in Figure 2.5. The index k refers to time step. The surface areas A_j and heat fluxes q_j are calculated at the boundary, while the energy density and volume are at the center of the grid. The areas and volume are calculated by standard formulas for annulus with profile given in Figure 2.5.

The heat flux calculation is carried out by using Kirchoff transformations to replace temperature T with Kirchoff temperature u, for their inherent benefit of isothermal treatment of the mushy layer.

$$u = \begin{cases} k_S\left[T - T_m\right], & \text{if } T < T_m \\ 0, & \text{if } T = T_m \\ k_L\left[T - T_m\right], & \text{if } T > T_m \end{cases} \tag{2.5}$$

$$q''^{k}_{j-\frac{1}{2}} = \frac{u_{j-1} - u_j}{\Delta r} \tag{2.6}$$

The process of melting is handled by a simple switching scheme given by Equation (2.7). Thus, the phases are determined by enthalpy alone. The zero for the enthalpy is set for the point when melting starts.

$$T_j^k = \begin{cases} T_m + \frac{E_j^k}{\rho c_s}, & \text{if } E_j^k < 0 \text{ (solid)} \\ T_m, & \text{if } 0 < E_j^k < \rho L \text{ (interface)} \\ T_m + \frac{E_j^k - \rho L}{\rho c_L}, & \text{if } E_j^k > \rho L \text{ (liquid)} \end{cases} \tag{2.7}$$

The thermal properties of PCM used for PCMS and VCS are shown in Table 2.1. These properties are obtained from the website of a PCM supplier [168].

Table 2.1: Thermophysical properties of PCM

Parameter	PCMS	VCS
Melting Point [°C]	6	37
Latent Heat [$\mathrm{kJ\,kg^{-1}}$]	220	210
Thermal Conductivity (solid) [$\mathrm{W\,m^{-1}\,K^{-1}}$]	0.25	0.25
Thermal Conductivity (liquid) [$\mathrm{W\,m^{-1}\,K^{-1}}$]	0.15	0.15
Density (solid)[$\mathrm{kg\,m^{-3}}$]	840	920
Density (liquid)[$\mathrm{kg\,m^{-3}}$]	760	840
Specific Heat (solid)[$\mathrm{kJ\,kg^{-1}\,K^{-1}}$]	2.12	2.21
Specific Heat (liquid)[$\mathrm{kJ\,kg^{-1}\,K^{-1}}$]	2.22	2.63

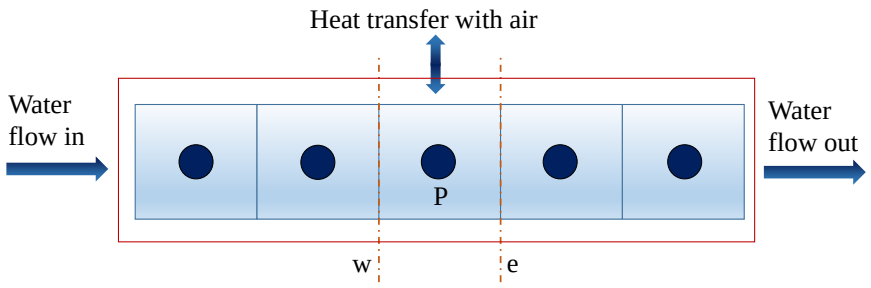

Figure 2.6: Discretization of Waterside Control Volume

2.1.2 Air-to-Water Heat Exchanger

In the three water-based systems (WTS, ITS and PCMS), cold water is circulated by means of a pump to the AWHX. A fan blows room air over the AWHX and onto the occupant to deliver cooling. Modeling of AWHX involves three control volumes: air-side CV, tube CV and waterside CV. The airside CV and tube CV are obtained from `CEEEModelicaLibrary` [165]. Waterside CV is described in this section.

Figure 2.6 shows the discretized waterside CV. The region enclosed by the red rectangle represents the length of the entire refrigerant tube which is discretized into five control volumes with water entering from the left and going out to the right. The outer surface is finned and exchanges heat with air. Enthalpy is calculated at the interfaces of control volumes while temperatures are calculated at the center. In the control volume highlighted in Figure 2.6, the enthalpy is calculated at points e and w, while the temperature is calculated at point P.

Due to a small operating range of temperature, the density and specific heat capacity of water are taken to be constant. The inlet enthalpy of water is an input for the control volume. The enthalpy at all other grid points is calculated using the energy equation (2.8).

$$mc\frac{dT}{dt} + \dot{m}_{out}h_{out} - \dot{m}_{in}h_{in} = \alpha\, A\, (T_{tube} - T_w) \tag{2.8}$$

The heat transfer coefficient is calculated using Churchill's correlation [169] for the transition and turbulent regions of flow. For the laminar region, the constant Nusselt number for constant heat flux condition is used, since the system is modeled to deliver a constant cooling load. The discontinuity in the correlation at the transition region is smoothened out by using a splice function as described in Li et al. (2010) [170].

The friction factor used for the heat transfer correlation is obtained from Churchill and Usagi (1972) [171] as it covers the entire flow regime. The dynamic viscosity and thermal conductivity of water used in calculations of Reynolds number and Prandtl number are calculated at ambient pressure and the temperature of control volume using the WaterIF97 [172] property calls from `Modelica.Media.Water`.

The dimensions for the AWHX are given in Table 2.2. These parameters are chosen by optimization using genetic algorithms in CoilDesigner [173] for maximum capacity and least cost as objective functions.

2.1.3 Water Tank

Recall that the WTS circulates chilled water through its water circuit. The chilled water is stored in a water tank. The water tank is modeled as a stratified tank with discretization along its height. The tank is assumed to be adiabatic.

The tank has discretized into five finite volumes. Each volume is modeled using the heated pipe component (`Modelica.Thermal.FluidHeatFlow.Components.HeatedPipe`) from `Modelica Standard Library`. This component provides a `HeatPort` interface, which is

Table 2.2: Dimensions for the Air to Water Heat Exchanger

Parameter	Value
Number of tubes	8
Number of tube banks	1
Tube length [m]	0.123
Tube outer diameter [m]	0.01588
Tube thickness [m]	0.000889
Fin type	Plate fin
Fins per inch FPI	24

used to model buoyancy effects in case of temperature inversion. The buoyancy component developed by Wetter et al. (2014) [174] for the `Buildings Library` is used for this purpose. It uses a directional diffusion approach to model buoyancy effects with a diffusion time constant and a conduction coefficient.

2.1.4 Ice Tank

The ice tank used in the ITS consists of ice cubes inserted into a tank filled with water. The process is very complex and depends on various factors like the shape of ice cubes, the geometry of the tank and flow characteristics around the ice [175]. For the conceptual nature of the present study, a lumped model is used. The ice tank is modeled as adiabatic. A constant heat transfer coefficient of 1000 $\mathrm{W\,m^{-2}\,K^{-1}}$ (based on results of Hao and Tao (2002) [175]) is used for calculation in Equation (2.9) to obtain the instantaneous rate of melting.

$$L\frac{dm_{ice}}{dt} = \alpha\, A\,(T_w - T_{ice}) \tag{2.9}$$

The ice cubes are modeled as spheres so that its instantaneous size can be calculated from Equation (2.10).

$$n_{ice}\rho 4\pi r^2 \frac{dr}{dt} = \frac{dm_{ice}}{dt} \tag{2.10}$$

The energy equation is then applied to the lumped ice tank control volume to calculate the temperature of the water exiting the tank as shown in Equation (2.11).

$$m_w c\frac{dT}{dt} + L\frac{dm_{ice}}{dt} + \dot{m}_{out}h_{out} - \dot{m}_{in}h_{in} = 0 \tag{2.11}$$

2.1.5 Battery

Battery modeling is necessary to reduce the total weight and cost, which are important parameters in the design of a portable cooling system. Accurate prediction of the state of charge (SOC) of the battery is critical to determine how long the battery will last with a typical user case scenario. The battery capacity should be sufficient to run the whole cooling operation without entering regions of overcharging and over-discharging for longer operation. A single unified battery pack must address all power requirements (cooling, controls, mobility) for a sufficient operating time while also maintaining a reasonable total system weight.

There are many mathematical models of batteries available in literature which vary in complexity, computational requirements and accuracy. The models based on electro-

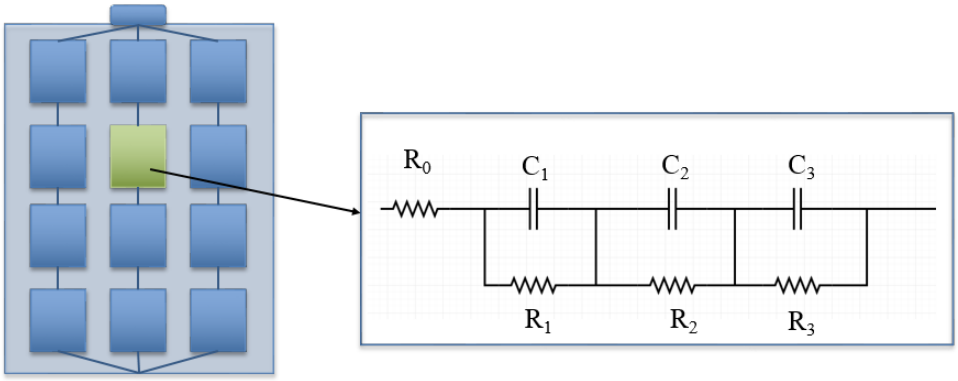

Figure 2.7: Modeling of Battery Pack by Scaling a Single Cell Modeled as an RC Circuit

chemical principles which model first-principle phenomena require significant computational resources and detailed datasets for input [176]. Equivalent circuit models have a good trade-off between exactness, complexity and usability while still providing some insights into the battery state [177]. As a result, the equivalent circuit approach is used. A simplified version of battery model based on the equations of `Electrical Energy Storage Library` [178] is used for the current work.

The values for the constants for the cell used are obtained experimentally using Electrochemical Impedance Spectroscopy. To obtain the performance of the battery pack from the model of a single cell, boundary conditions are applied to the cell model as if it is located inside the battery pack as shown in Figure 2.7. The battery pack consists of 21 cells of type Samsung ICR 18650 26F, with three parallel circuits of seven cells in series (7s3p). The scaling from cell to the full battery pack is done as described by the Equations (2.12) - (2.14). The number of cells in parallel $n_p = 3$ and number of cells is series $n_s = 7$.

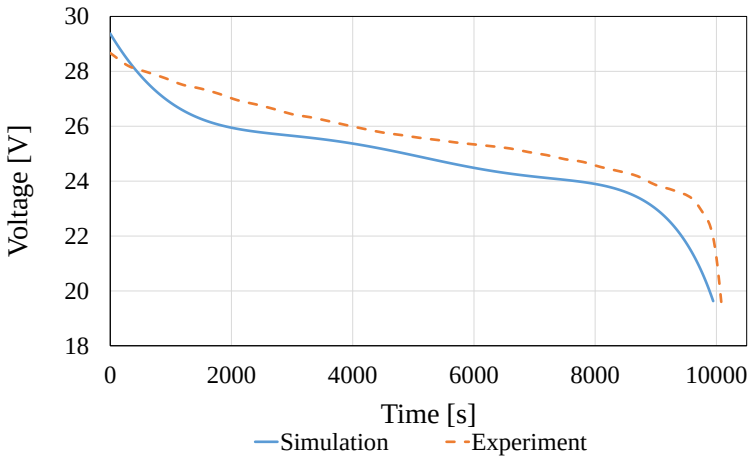

Figure 2.8: Validation of Battery Model

$$P_{cell} = \frac{P_{bat}}{n_s\, n_p} \tag{2.12}$$

$$I_{bat} = n_p\, I_{cell} \tag{2.13}$$

$$\mathbb{V}_{bat} = n_s\, \mathbb{V}_{cell} \tag{2.14}$$

The two primary modes of battery degradation are charge dissipation aging and calendric aging. Typically, the calendric aging is of the order of 8-10 years. Since the device is envisioned for everyday use, it is safe to assume that the primary source of degradation will be charge dissipation. Hence calendric aging is not modeled. Linear aging constant calculated from the battery datasheet is used for charge dissipation aging as shown in Equation (2.15). Kindly note that the equation uses battery capacity in SI-unit of Coulomb. Typically, the battery capacity is listed in Ampere-hour by manufacturers. Conversion, factor for this is 1 Ampere-hour = 3600 Coulombs.

$$C = C_0 + k_C\, Q_{abs} \tag{2.15}$$

During continuous battery operation, the chemical energy is converted to electricity with some energy lost as heat. This energy loss to heat leads to faster dissipation of battery and is calculated using a proportional constant as shown in Equation (2.16).

$$SOC = SOC_0 - K\,\frac{Q_{abs} - Q_0}{C} \tag{2.16}$$

$$I_{cell} = \frac{\mathbb{V}_{cell} - \mathbb{V}_1 - \mathbb{V}_2 - \mathbb{V}_3}{R_{ext} + R_0} \tag{2.17}$$

The voltage across the battery is a function of its state of charge; a correlation connecting voltage and state of charge can be developed from discharge curves found in the battery datasheet. Finally, the current across the equivalent R-C circuit from Figure 2.7, is calculated using Equation (2.17). The model is validated by comparing its results to a 70 W constant power draw circuit. The results of the validation are shown in Figure 2.8 .

2.1.6 Robotic Platform

The power consumption from the motion of robotic platform is estimated from first-principles based approach used by Gonullu [179]. The free body diagram of the platform is shown in Figure 2.9. The total force required for motion (F_t) is the sum of the gravitational force acting along the incline (F_g), the drag force by the air (F_d), the force to overcome friction (F_f) and the force required to produce acceleration (F_a).

$$F_t = F_g + F_d + F_f + F_a \tag{2.18}$$

Since the platform operates at speeds around 1 $\mathrm{m\,s^{-2}}$, drag force can be neglected. If m is the total mass of the portable cooling system, g the acceleration due to gravity,

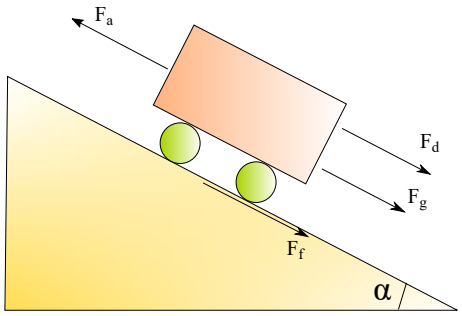

Figure 2.9: Free Body Diagram for Robotic Platform

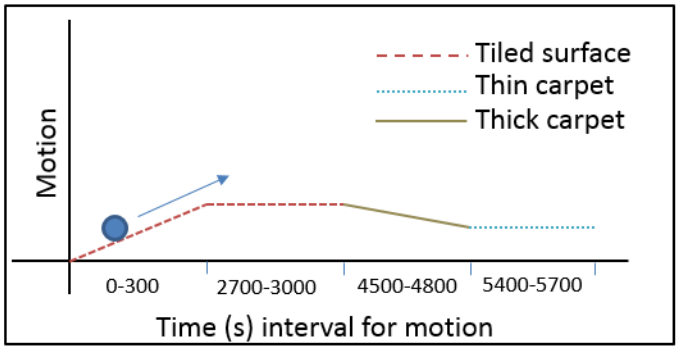

Figure 2.10: Input Set for the Robotic Platform

the remaining forces can be calculated as:

$$F_g = mg\sin(\theta) \tag{2.19}$$

$$F_f = f_r mg\cos(\theta) \tag{2.20}$$

$$F_a = m\,a \tag{2.21}$$

Finally, the net power for the motion of the platform (P) is obtained as:

$$P = F_t\,v \tag{2.22}$$

where v is the velocity of the platform.

Typical variations in motion are changes in velocity, motion over different surfaces and changes in surface inclination. One `TimeTable` block is assigned to each of acceleration

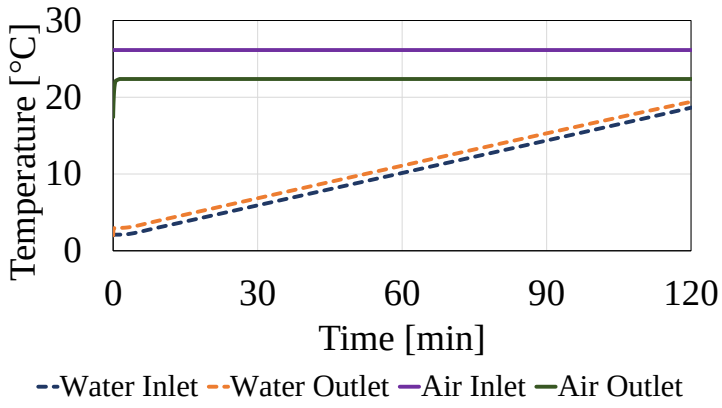

Figure 2.11: Temperatures at various locations in WTS

(a), rolling friction resistance of surface (f_r) and the surface inclination angle with respect to the horizontal (θ) and is used to capture these variations in the motion.

A common motion is assigned for all systems to represent a typical motion of a PPCS. It involves motion on different surfaces at varying inclinations and speed. The total motion is for 20 minutes in the two-hour simulation period. Motion in each of these four intervals is shown in Figure 2.10.

2.2 Results and Discussion

This section discusses the results of system models from the previous section. For the current study, all systems are sized to deliver cooling for two hours. Some additional considerations for modeling of each system and its response are first presented, followed by their comparison.

The water tank system is initialized with 17.2 kg of water at 2°C, divided into five equal control volumes of the stratified water tank. The temperature of water at the end of two-hour operation is 17.3°C. Figure 2.11 shows temperatures on the airside and waterside of the AWHX in the simulation.

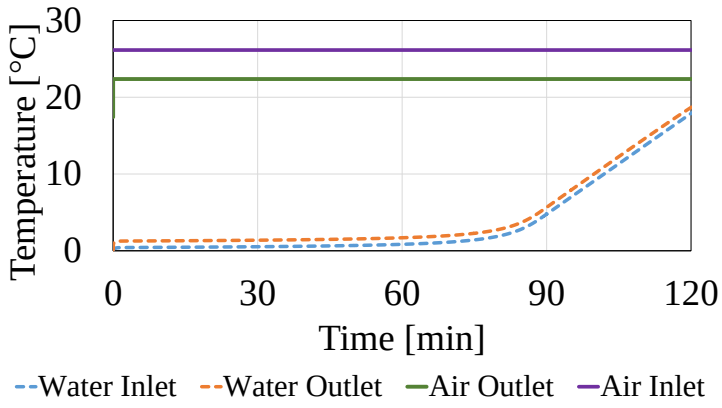

Figure 2.12: Temperatures at various locations in ITS

The ice tank system is initialized with 3 kg of water in thermal equilibrium with 2.45 kg of ice comprising of 185 spheres of 3 cm diameter, which is the typical size of ice obtained from an ice maker. This is the minimum amount of ice that can fulfill the cooling requirements. Figure 2.12 shows temperatures on the airside and waterside of the AWHX in the simulation. Two distinct regimes can be observed. For first 90 minutes, the temperatures on the waterside are close to 0°C. Then the temperatures start to increase rapidly. This is the portion, where the ice is completely melted and the system now operates as a water tank system. Roughly, 25% of the cooling from the ITS is by the operation as WTS. This reduces the amount of ice required for the cooling operation and further reduces system weight further. The weight of cold storage in ITS is only 33% of the WTS.

The PCMS is initialized with 5.2 kg of PCM at an initial temperature of 5.5°C, which is slightly less than its melting temperature. The temperature of water entering the AWHX for PCMS is shown in Figure 2.13. The PCM starts melting from the inside, i.e., where it is in contact with the tube. As the PCM melts, its temperature increases. A higher temperature gradient is required to melt the PCM furthest from the tube. As a

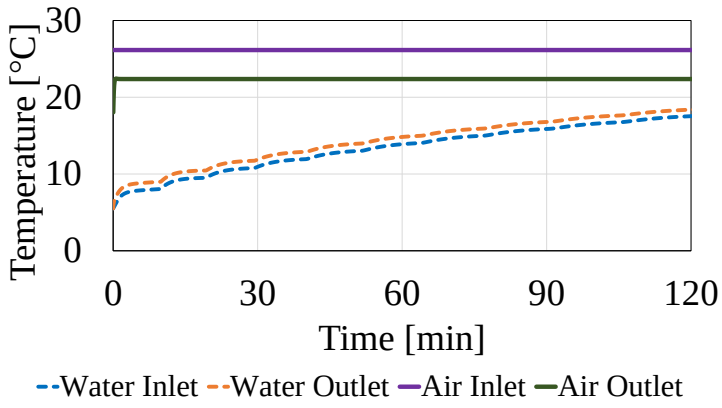

Figure 2.13: Temperatures at various locations in PCMS

result, the temperature of PCM in contact with the refrigerant tube continues to rise and the AWHX receives increased temperature of water progressively. In the real case, the temperature gradient would be slightly smaller due to the effects of natural convection, which are not included in the current model. Reduced temperature gradient equates to lesser sensible storage in the liquid portion of the PCM. However, sensible storage amounts to 10% of the total storage and the contribution of natural convection in that portion would lead to much lesser deviation.

For the VCS, a paraffin-based PCM with melting temperature of 37 °C is selected to capture the condenser heat (See Table 2.1). The minimum amount of PCM required for the purpose is 5.9 kg. Note that this amount is higher from the PCM required for the water based system because the PCM is storing the condenser load. Secondly, the latent heat of the PCM used for VCS is slightly smaller than the one used for PCMS. As can be observed from Figure 2.14, the evaporator temperature is 16°C while the condenser temperature is rising till 55°C. The continuous increase in condenser temperature is attributed to the lack of modeling of natural convection in PCM. The thermal resistance on the PCM side increases with time as the solid melts, since the liquid PCM has lesser conductivity than

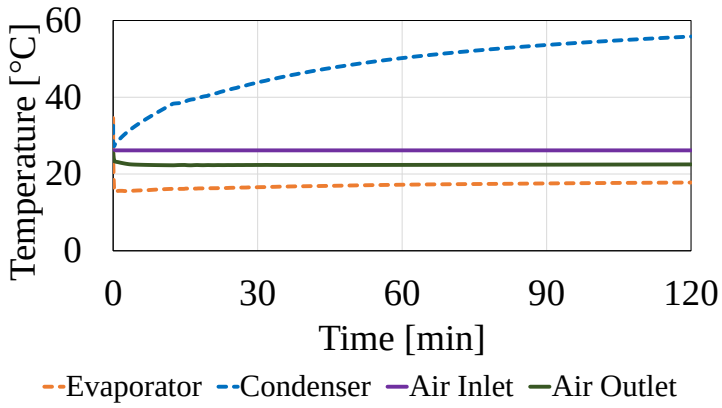

Figure 2.14: Temperatures at various locations in VCS

the solid. In the real case, however, there will be increases and decreases in thermal resistance as the melting progresses.

The following values of compressor efficiency are assumed for the simulation: volumetric = 83%, isentropic = 70% and motor = 80%. The displacement volume is taken as 1.4 cc, with RPM = 2700. The values are taken for the smallest compressor available in the market [180]. The breakdown of energy consumption from individual components of VCS is shown in Figure 2.15. The coefficient of performance of the system is evaluated as the ratio of net cooling delivered to the net power consumed by the compressor, fan and the robotic platform. The COP evaluated for the VCS simulation = 2.97.

2.2.1 System Comparison

Weight, power consumption and cost are the main driving factors behind the design of portable air conditioning devices. This subsection gives a comparison of the four systems based on these parameters.

The weights of all the four systems are plotted in Figure 2.16. The first legend *Heat Storage* refers to the weight of the minimum storage required for two-hour operation

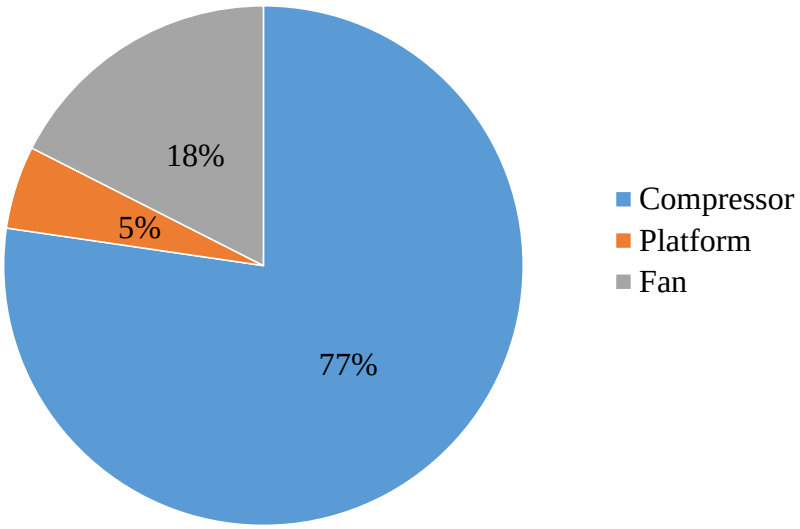

Figure 2.15: Breakdown of Power Consumption in VCS

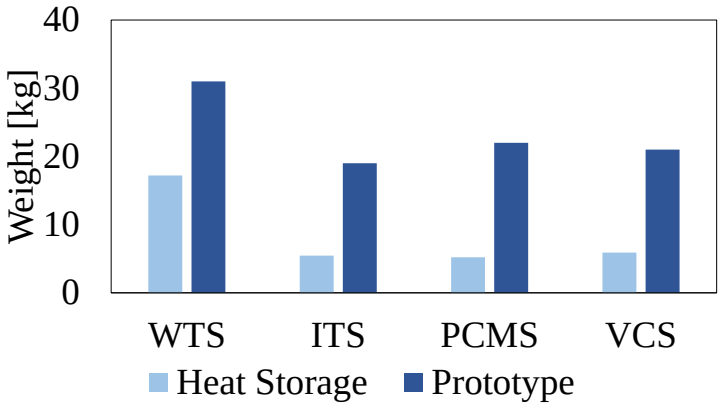

Figure 2.16: Comparison of Weight

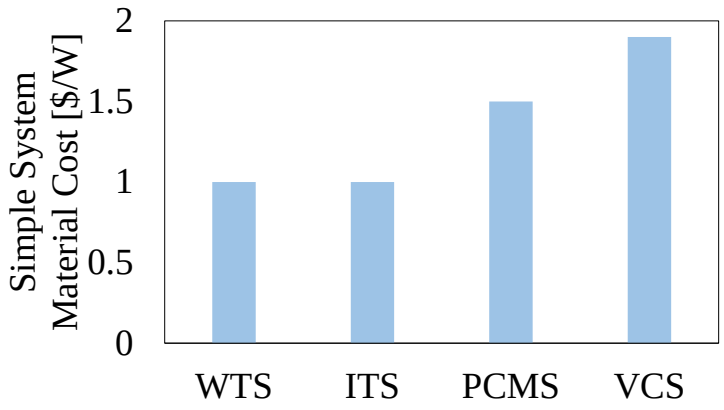

Figure 2.17: Comparison of Price

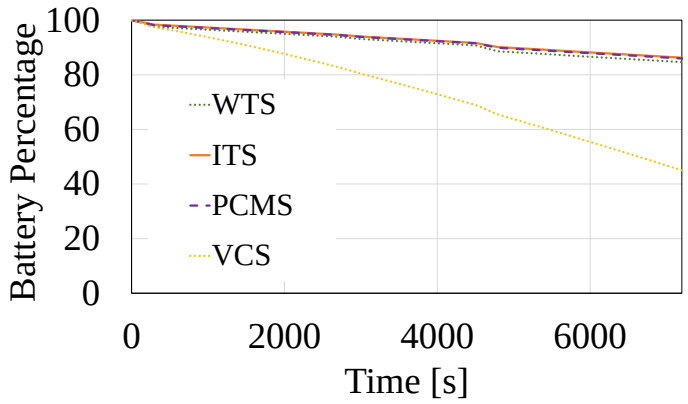

Figure 2.18: Comparison of Battery

of each system. For the water tank system, this term is the weight of water = 17.2 kg. To obtain total system weight, data from the [181] prototype is used: Battery = 1.1 kg, Platform = 4.2 kg, Structural components = 3.5 kg, Heat exchangers and tubing = 2.2 kg, container = 1.7 kg and electronic components = 1.1 kg. These are assumed to be constant across all systems. For PCMS, 3 kg of water is added to fill up the tubing and heat exchangers. For VCS, additional component weights for the compressor, expansion device and refrigerant charge are added. The prototype weight calculated using these values is also plotted as the legend *Prototype* in Figure 2.16. As can be seen, the WTS weighs roughly 10 kg more than the other three systems. ITS, which was expected to be the most compact is only 2 kg lighter than the vapor compression system.

Figure 2.18 shows battery consumption from all the four systems. The simulation is initialized with a completely charged battery. The transient power draws from the various sources leads to consumption of the battery. At the end of the two-hour operation, the VCS ends up consuming much more battery than the others. This can be attributed to the operation of a compressor instead of a water pump. The water based systems (WTS, ITS and PCMS) can therefore operate with a smaller battery pack compared to VCS.

A cost database for components is developed to make rough cost estimates for system mass production. Figure 2.17 shows the price per watt of cooling for the four systems. We can observe that VCS is much more expensive than the other systems. This is primarily due to the higher price of the phase change material and also the compressor.

2.2.2 Air Flow Rate

The environment of the occupant plays an important factor in determining the operating conditions of the PCS. For thermal comfort, different amount of cooling is

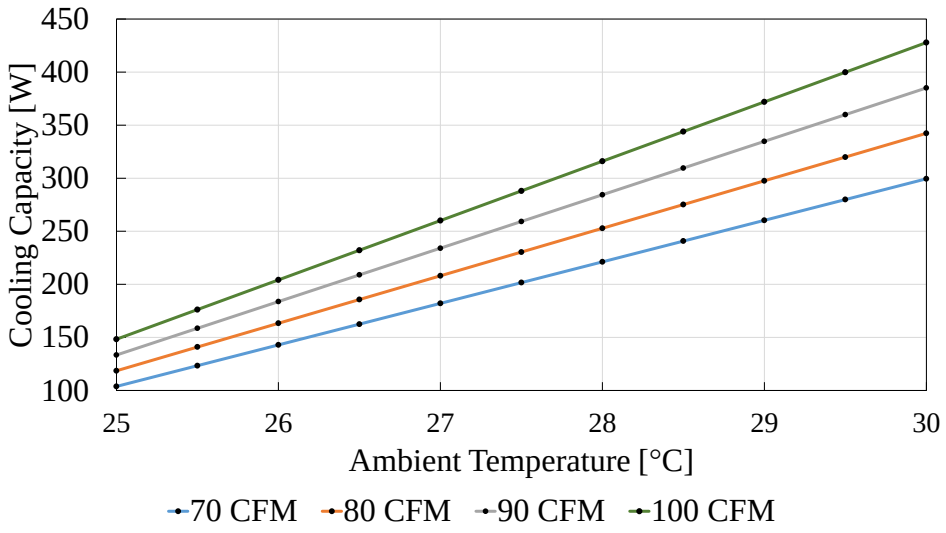

Figure 2.19: Cooling Capacity Required to Obtain the Same Supply Air Temperature at Different Ambient Conditions

required at different ambient conditions. For a fixed cooling capacity, increasing air flow rate from the PCS will increase its supply air temperature. The air flow rate can be increased by increasing the fan speed or by selecting a nozzle with a smaller diameter.

The air inlet mass flow rate for the simulated case = 0.04452 $\mathrm{kg\,s^{-1}}$. This corresponds to a fan with 80 CFM (0.038 $\mathrm{m^3\,s^{-1}}$) of volume flow rate. If we assume a constant specific heat capacity of air = 1005 $\mathrm{J\,kg^{-1}\,K^{-1}}$, the temperature difference between the supply air and room air = 3.8 K for a cooling capacity of 170 W. The ambient temperature for the operation is taken as 79 °F (26.15 °C), giving the supply air temperature = 22.35 °C. For a fixed air mass flow rate, to deliver a constant supply air temperature of 22.35 °C, variation in required cooling capacity for different ambient conditions is plotted in Figure 2.19. At ambient temperature of 30 °C, for air volume flow rate of 100 CFM, the cooling capacity required = 428 W. This operating condition will require a very heavy thermal storage.

The supply temperature of the PCS, however, may not be the correct design parameter for sizing the air flow rates. Zhu et al. [182] carried out a CFD-based analysis to investigate the cooling efficiency of a PCS (ratio of the sensible heat removal to the cooling capacity). Their study involved a 100 W cooling capacity PCS placed at a distance of 1 m from the occupant, in a room with 3 ACH (Air Changes per Hour Ventilation Rate) and air temperature of 26°C. They found a positive linear correlation between sensible heat loss and air flow rate, indicating that the personalized airflow with higher airflow rates could effectively remove additional heat from human body. Additionally, at the same air flow rate, a smaller nozzle could remove more sensible heat from the human body. Thus, the effect of local forced convection overcame the opposing effect of temperature increase for their set of operating conditions. So it may be possible to keep occupants in higher ambient conditions comfortable at higher supply air temperatures (and thus a much lower cooling capacity). The correct design conditions for operation at all these variations of ambient conditions will require experimental thermal comfort study and is part of future research.

2.2.3 Phase Change Material

The selection of PCM is an important design criteria for PCS. The PCM has to go through both melting and solidification in a reasonable amount of time. Secondly, PCM manufacturer may not have a good resolution of melting temperature range. In the VCS, the PCM is used to capture the condenser heat. This is done to prevent additional heat loads to the building. PCM with following melting temperatures are available at one of the manufacturers [168](29°C, 37°C, 42°C and 48°C). For vapor compression cycle, a lower PCM melting temperature would result in a higher COP. If the melting temperature

is very close to the ambient temperature, the solidification of PCM after the cooling operation will take a very long time due to a low temperature gradient available for heat exchange. Among the range of temperatures available, 37°C is selected from both COP and solidification time point of view.

The PCMS uses water to extract cooling from the frozen PCM. The melting temperature of PCM selected for this application is 6°C. PCM with following melting temperatures are alternate options for this application [168](4°C, 7°C, 8°C and 15°C). The latent heat of the PCM melting at 6°C is 220 $\mathrm{kJ\,kg^{-1}}$ is much higher than the latent heat of the other candidates available in its neighborhood (178 to 187 $\mathrm{kJ\,kg^{-1}}$). To make the thermal storage lightest, the current choice is the best option.

2.2.4 Price Considerations

Hoyt et al. (2015) [109] simulated HVAC energy savings by varying cooling setpoints in 7 different climates and 5 different HVAC model types. The averaged results from their work is listed in Table 2.3. In 2011, total primary energy consumption per person in the United States was about 310 million Btu [1]. Building sector accounts for 41% of the primary energy consumption, with 11.8% of that fraction taken up by space cooling. Hence, energy spent on cooling per person =(0.118*0.41*310 million Btu)= 15 million Btu = 15.8×10^{10} J. Assuming symmetrical heating and cooling seasons, time duration for cooling = 0.5 year = 0.5*365*24*60*60 sec = 15.768×10^{10} sec. Thus, average cooling power per person = (cooling energy per person)/(cooling time duration) = 1002 W.

The average price of electricity in the United States is approximately 12 cents per kWh [183]. For a setpoint of 25.6 °C, mean saving = 31%. Thus, cost saving for each hour = $ 0.12*0.31*1002/1000 = $ 0.037. For the cooling duration of half year, net saving for

Table 2.3: Total HVAC energy savings when varying cooling setpoints [109]

Cooling Setpoint [°C]	Mean Savings [%]	Maximum Savings [%]
23.3	13	26
24.4	23	45
25.6	31	58
26.7	37	66
27.8	42	70
28.9	46	73

this case = 0.5*365*24* ($ 0.037) = $ 163.26.

Power consumption for all the systems is shown in Figure 2.20. All the PPCS have the same inputs for motion which have been described in Figure 2.10. The PPCS moves with uniform velocity in the intervals of motion with acceleration and deceleration at the beginning and end of its motion, respectively. WTS, being the heaviest consumes much more power during its motion than the other systems. By averaging the net power consumed by each PPCS in the two-hour interval, we can arrive at the total cost savings by setpoint elevation with the PPCS in operation. The average power consumed by WTS, ITS, PCMS and VCS are 16.43 W, 14.72 W, 14.99 W and 55.47 W, respectively. For elevation of temperature setpoints as per Table 2.3, the reduction in building energy cost is shown in Figures 2.21 and 2.22 for the cases of mean savings and maximum savings.

The estimated mass production price of WTS, ITS, PCMS and VCS for 170 W cooling and a two-hour operation are $173, $173, $256 and $324, respectively. These numbers are obtained by private correspondence with suppliers. One of the benefits of PPCS is that it has zero retrofitting costs. However, there will be additional costs associated

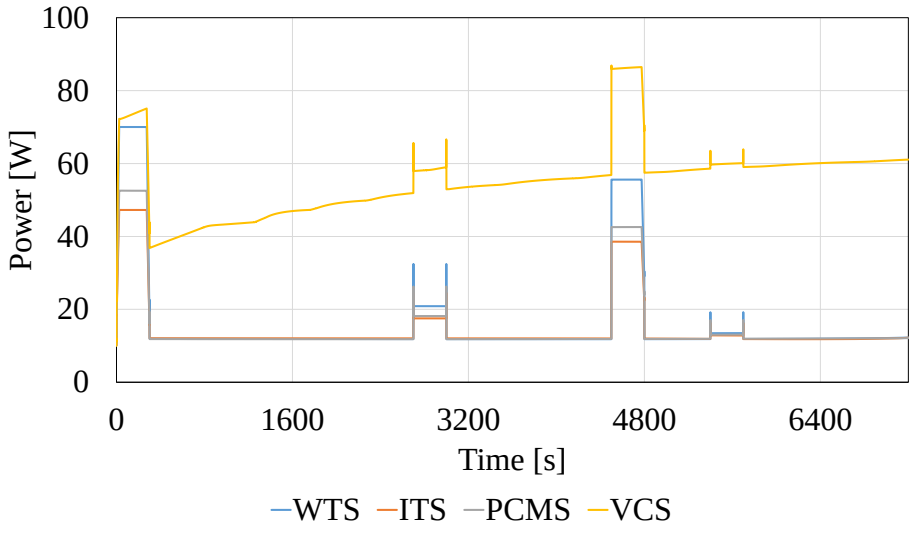

Figure 2.20: Power Consumption by the Four PPCS

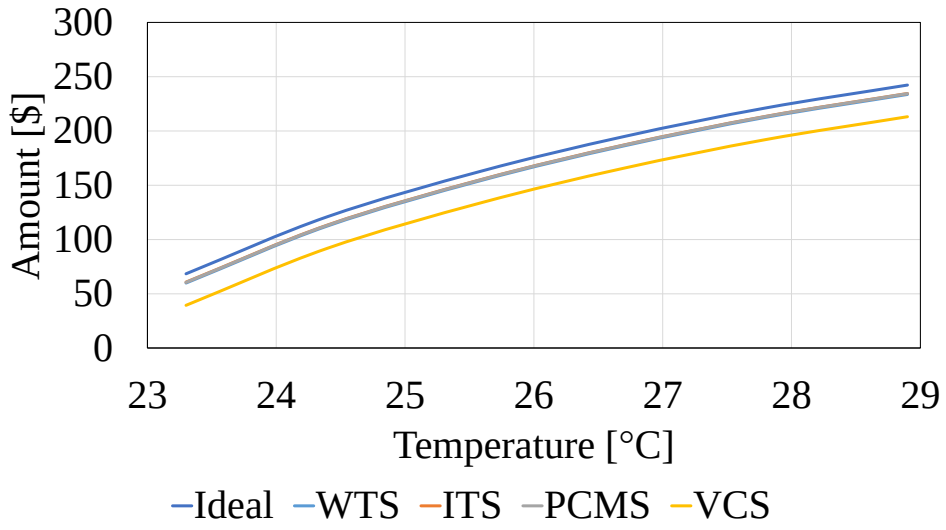

Figure 2.21: Mean Yearly Savings from PPCS Operation

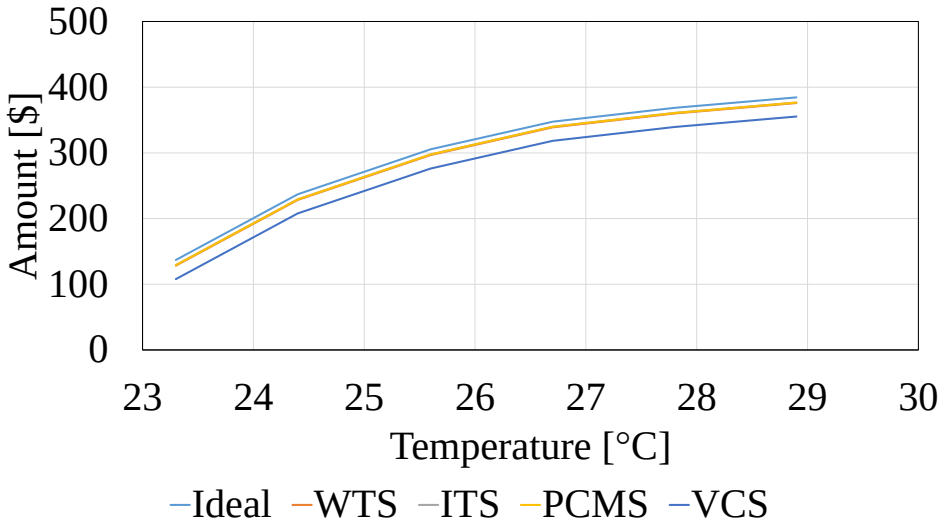

Figure 2.22: Maximum Yearly Savings from PPCS Operation

with labor and shipment. For the purpose of this preliminary analysis, let us consider the economics of a PPCS when its selling price varies from $200 to $600 in steps of $100. Payback period for each of these systems as a function of setpoint temperature can now be evaluated at these selling prices for each of the systems. For brevity, only the case of VCS is shown. WTS, ITS and PCMS will have lower payback, due to higher savings than VCS. The results for the calculations with both the mean savings and maximum savings are shown in Figures 2.23 and 2.24. It can be observed that the payback period varies significantly based on operating conditions.

The calculation assumes that the PPCS is being operated for the entire duration of the cooling season. However, in the real case the device will need to take breaks to recharge its thermal storage. Secondly, there will be some energy spent on recharging the thermal storage. These details are not accounted for in the present investigation due to its conceptual nature. When the conditioned space is unoccupied, there is no need for PPCS to operate. This will lead to higher savings than those shown in Figures 2.21 and 2.22.

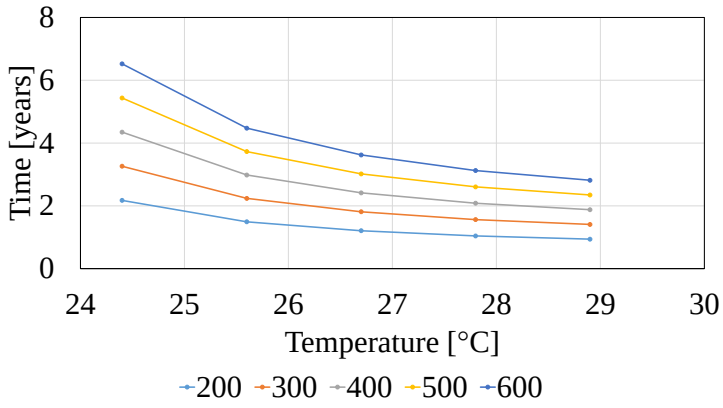

Figure 2.23: Payback Evaluation from Mean Savings for VCS

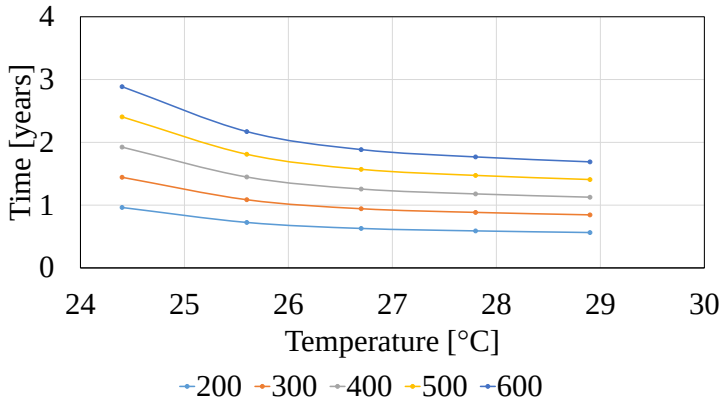

Figure 2.24: Payback Evaluation from Maximum Savings for VCS

These details will become clearer with development and testing of real devices and is part of future research. A more realistic payback period may be in the range of 5-10 years.

The price of PPCS is being around $500 for the consumer makes this a very attractive option for saving building cooling energy. Personalized conditioning also provides better cooling than the conventional systems.

Chapter 3: Development of Vapor Compression Cycle based Personal Conditioning System

3.1 Introduction

The previous chapter highlighted benefits of using personal conditioning systems. Water based PCS require more user attention for continuous usage like refill chilled water or ice, re-solidify PCM. From user's convenience perspective, the vapor compression system based PCS is the most desired and so, a prototype based on this idea called the Roving Comforter (RoCo) has been developed [181]. The present chapter briefly discusses its operation and then discusses development of a dynamic model for its thermal storage recharge, which was identified as an important factor for improvement.

RoCo uses a compact R134a based vapor compression system for cooling. Following its cooling operation, during which waste heat from the condensing refrigerant is stored in a phase change material (PCM), a two-phase loop thermosiphon is used to discharge (solidify) the PCM to enable its next operation. The transient operation of this thermosiphon is the focus of the present chapter.

Use of a PCM as the storage medium provides high energy density due to the ability to store thermal energy as latent heat during the phase transition; however, the discharge rate is limited by the low thermal conductivity of the PCM. Insertion of a graphite foam

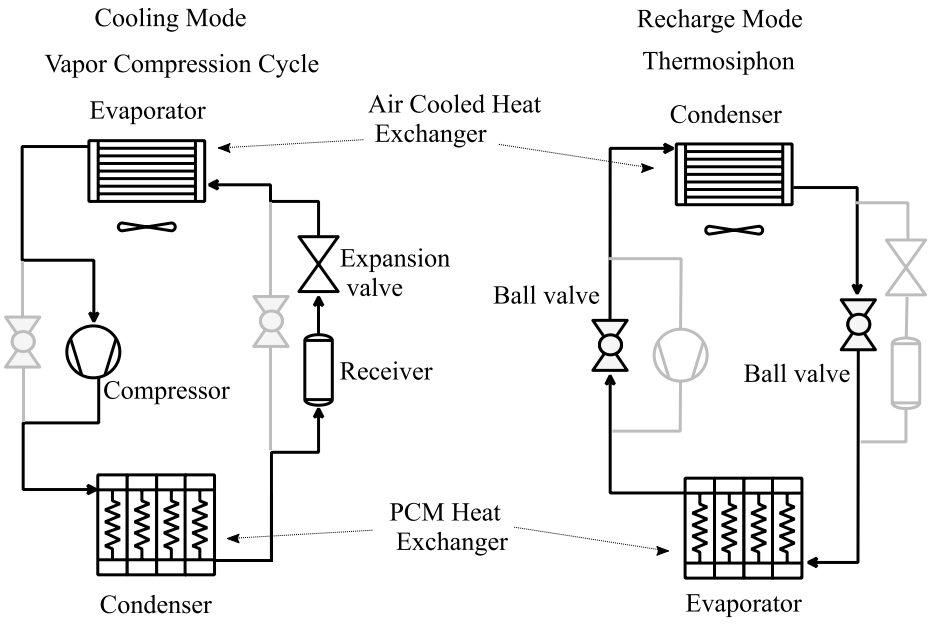

Figure 3.1: Schematic of two modes of operation of RoCo

within the PCM can increase the rate of discharge and decrease the downtime of the cooling device. Since graphite enhancement involves a tradeoff between improving the discharge time at the expense of PCM volumetric latent heat, the impact of graphite foam density on the PCM discharge rate is investigated by using a Modelica-based transient model of the thermosiphon.

The two alternating operating modes of RoCo are shown in Figure 3.1. The cooling operation (Figure 3.1, left) is reliant on an R134a based vapor compression cycle (VCC). Heat removed from the condensing refrigerant during the VCC operation is captured by a commercial, paraffin-based PCM (PureTemp 37, Tmelt = 37°C, k = 0.2 $\mathrm{W\,m^{-1}\,K^{-1}}$ [168]) surrounding the condenser refrigerant tubing to avoid an addition to the building heat load. This PCM was chosen since the phase transition temperature enables high COP in the VCC operation due to the low melting temperature, but does not liquify by heat transfer

with the surroundings since the transition temperature is 9°C higher than the weighted mean of the US summer dry bulb temperature [152]. Stability of this material has been demonstrated over 65,000 thermal cycles [168].

The cooling operation terminates when the PCM is completely melted since the condenser can no longer store rejected heat from the refrigerant as latent energy, leading to elevated condenser temperatures and decreased cycle efficiency. Thus, there is a need for re-solidification of the PCM (PCM discharge) before the next cooling operation. Since the PCM is insulated from the ambient to minimize heat loss to the conditioned space during cooling, a thermosiphon operation in the same refrigerant circuitry is employed to enable a controlled discharge process.

In the thermosiphon operation, liquid refrigerant in the PCM-HX absorbs heat from the PCM and vaporizes. The thermosiphon operation is used to discharge the heat stored during the cooling operation. Typically, the cooling is required during the day time and thermosiphon is at night time. This also facilitates peak load shifting from the electricity grid as the discharge is done during the off-peak hours and provides cost savings to customers. There are two methods to reject the heat during night time: (1) reject heat to the internal spaces during the night when the building is unoccupied and the building load is insignificant (2) reject heat outside the conditioned space by moving the RoCo [184]. The vapor rises and condenses in the air-cooled heat exchanger (AC-HX). The condensed liquid flows back by gravity to the PCM-HX. A receiver is included in the circuit to ensure that the PCM-HX is filled with liquid refrigerant to prevent dry out during the thermosiphon operation. The initial PCM-HX prototype provided 2 hours of cooling operation and required 8 hours for discharge [181], limiting RoCo to a single cooling operation per day. The long discharge time can be attributed to the low thermal

conductivity of the PCM.

The present chapter focuses on modeling a thermosiphon used to recharge the PCM battery of an innovative personal air conditioning device called the Roving Comforter (RoCo), which is described in detail in Du et al.(2016) [181]. Figure 3.1 shows the schematic for the two alternating operating modes of RoCo. During the cooling operation shown in the left image of Figure 3.1, the heat released by the condenser is captured by the surrounding PCM to avoid addition to building heat loads. The cooling operation is terminated when the PCM surrounding the condenser is completely melted. Before the next cooling operation, there is a need for re-solidification of the PCM (PCM recharge). The right image in Figure 3.1 shows RoCo operating in thermosiphon mode. The compressor and the expansion valve are bypassed by operating a pair of ball valves to reduce pressure drops in the refrigerant circuit. A receiver is included in the circuit to ensure that the PCM based heat exchanger (PCM-HX) is always completely filled with liquid refrigerant during the thermosiphon operation to prevent dryout. The system provides more than two hours of cooling operation with 8 hours for recharge [181]. This essentially limits RoCo to a single cooling operation per day, which is not desirable. The long recharge time can be attributed to the low thermal conductivity of the PCM.

One method to increase the thermal conductivity of PCM is to create a composite of pure PCM and a highly conductive porous compressed expanded natural graphite (CENG) foam [185–187]. The amount of CENG in the composite PCM is measured as graphite bulk density, or mass of graphite in the sample volume. As the graphite bulk density increases, the thermal conductivity increases, but the composite latent heat decreases. The saturation of CENG foams with PCM has been shown to increase the thermal conductivity by more than an order of magnitude; however, this reduces the latent heat storage of the

PCM up to 35% due to the displacement of PCM by graphite as well as air contained within closed pores formed during the fabrication process [185–187]. The reduced latent heat of the PCM composite leads to increased weight and volume of the thermal battery, which is not desireable for a portable device like RoCo. Thus, there is a tradeoff between the reduced recharge time and increased volume in the material selection. A transient analysis of the thermosiphon mechanism is carried out to evaluate the most suitable material among the CENG developed by Mallow et al. [188].

This chapter presents a semi-empirical model for a thermosiphon with transient equations not only for the refrigerant side but also the thermal storage. The state of the PCM is part of the solution, adding further to the complexity of the model. Modelica [33] is used for modeling because of the object-oriented, declarative, and acausal modeling approach, reusable libraries for two-phase flow, refrigerant media property packages [189] based on REFPROP 9.0 database and differential algebraic equation solvers. This enables development of the model with similar detailing on the refrigerant side as Bodjona et al. [190], without the need to write equations for refrigerant properties and solvers.

3.2 Component Modeling

This section discusses equations and assumptions used in the component models for the thermosiphon system model. The component models will be combined to form the system model, which will be first validated with experimental data and then used to evaluate the thermal storage performance of graphite enhanced PCM.

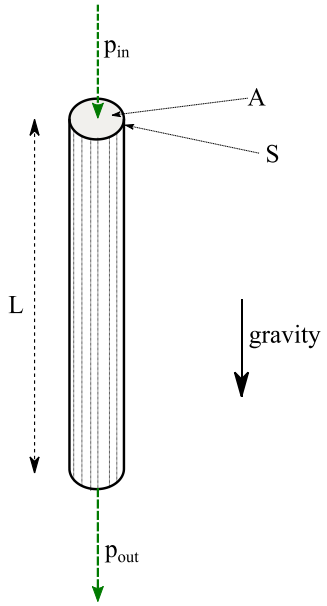

Figure 3.2: Control volume for downcomer

3.2.1 Downcomer and Riser

The connecting tubes between the evaporator and condenser act as the downcomer and riser. Their dynamics is expected to be on a timescale faster than those of the heat exchangers. One of the important simplifications in the modeling of dynamic systems is the time scale abstraction in which faster timescales are treated as a steady state. The mass and energy storage in these components is hence neglected based on this assumption. The momentum equation is used to evaluate the mass flow rate in the system. Such components are referred to as flow models in Modelica terminology.

The finite volume discretization of the momentum equation for flow model type components is described in Elmqvist et al. (2003) [41]. For the lumped control volume of the downcomer (Figure 3.2), equating mass flow rates at the inlet and outlet leads to 3.1

$$L_t \frac{d\dot{m}}{dt} = A_c(p_{in} - p_{out}) - \frac{1}{2}\frac{\dot{m}^2}{\rho A^2} f S L_t - A_c \rho g L_t \tag{3.1}$$

For the downcomer, the outlet is below the inlet in height and this leads to 3.2.

$$L_t \frac{d\dot{m}}{dt} = A(p_{in} - p_{out}) - \frac{1}{2}\frac{\dot{m}^2}{\rho A^2} f S L_t + A \rho g L_t \tag{3.2}$$

Since the the model assumes single phase refrigerant flow in the riser and downcomer, the Fanning friction factor is calculated using a function developed by combining Hagen-Poiseulle and Blasius [191] equations to account for both laminar and turbulent flows for single phase refrigerant. The objective of the current investigation is the heat transfer characteristics of the thermosiphon for which the assumption is valid (the sensible heat of R134a is very small compared to its latent heat). However, for an investigation focused on fluid flow characteristics, it may be necessary to develop a more detailed model for the downcomer and riser. Interpolation is necessary to avoid chattering issues encountered in transient simulations with equations that are not continuous and differentiable.

3.2.2 Phase Change Material Control Volume

Several models exist in the literature for modeling the melting and solidification of PCM [192–194]. The enthalpy method [195] is used in the current study due to the advantage of carrying out calculations on a fixed grid with an implicit treatment of the phase change boundary.

The energy equation applied to the PCM control volume gives rise to Equation (3.3). The PCM-HX involves helical tubes surrounded by PCM, which results in very complicated 3D mathematical equations involving phase change and refrigerant flow. For the

purpose of current research, two primary assumptions are made to obtain equations for system level simulation. First, the PCM control volume is modeled as a lumped system. This eliminates the need for 3D momentum equations for natural convection flow within the molten PCM. Secondly, since the density difference between the solid and liquid phase of PCM is less than 10%, the average value of densities of both the phases is used in the calculations. These two assumptions enable modeling a simpler form of the energy equation shown in Equation (3.4).

$$\rho \frac{\partial h}{\partial t} + \nabla(\rho v h) = \nabla k(\nabla T) \tag{3.3}$$

$$m_{pcm} \frac{dh}{dt} = \dot{Q} \tag{3.4}$$

The PCM modeling consists of two components: one to model its heat storage and a second to model its rate of heat transfer.

3.2.2.1 PCM Heat Storage

The PCM heat storage is modeled using a component named PCM Capacitor. It models the left-hand side of Equation (3.4). The only unknown variable in the enthalpy method formulation is the enthalpy-temperature dependency of the PCM which is calculated using Equation (3.5). The PCM solidifies over the temperature range from TL to TS. DSC measurements were taken using a TA Instruments Q2000 with a heating and cooling speed of $5\,^{\circ}\mathrm{C\,min^{-1}}$ to obtain the variations of the effective specific heat capacity,

c(T), in the interface region. The point where the PCM just starts to melt is taken as the zero reference for the enthalpy function.

$$h(T) = \begin{cases} \int_{T}^{T_A} c_s dT, & \text{solid} \\ \int_{T_B}^{T_A} c(T) dT, & \text{two phase} \\ h_{sl} + \int_{T}^{T_B} c_L dT, & \text{liquid} \end{cases} \tag{3.5}$$

3.2.2.2 PCM Heat Transfer

The heat transfer from the PCM is modeled using the PCM Conductor block. To enable modeling of any heat exchanger geometry, either with a helical or straight refrigerant tube, the heat transfer coefficient as a function of melt fraction, λ, is set as an input and evaluated by experimental or numerical methods. This enables modeling varying effects of conduction and natural convection, which occurs in the case of a non-enhanced PCM with helical refrigerant tubes. The conduction dominant heat transfer in a graphite enhanced PCM with straight refrigerant tubes can also be captured using the same component.

The melt fraction is calculated from PCM enthalpy by using Equation (3.6) in the PCM Capacitor block. It is then provided as an input to the PCM Conductor block. The use of the heat transfer coefficient, pcm, simplifies the right-hand side of Equation (3.4) as shown in Equation (3.6). Calculation of α_{pcm} will be discussed in the subsection 3.2.2.3 for the case of pure PCM and in Section (3.4) for the graphite enhanced PCM. The net value of net heat transfer is calculated using the temperature difference between PCM Conductor and lumped refrigerant CV (Equation (3.8)).

$$\lambda = max(0, min(1, \frac{h}{h_l})) \tag{3.6}$$

$$\dot{Q}_{pcm} = \alpha_{pcm} A \left(T_{tube} - T_{pcm}\right) \tag{3.7}$$

3.2.2.3 Empirical heat transfer coefficient function

The empirical heat transfer coefficient as a function of melt fraction, which is an input for the PCM Conductor (Equation (3.8)), is not available in the literature and is, hence, obtained by an experiment. The heat transfer coefficient evaluation procedure is similar to the one adopted by Merlin et al. [196] and is only briefly explained for the sake of brevity. The experimental setup (see Figure 3.3, left image) includes a single helical coil (see Figure 3.3, right image) placed inside a cylinder filled with PCM. It is representative of one quarter of the PCM-HX. A peristaltic pump is used to circulate water through a PID-controlled heater to melt the PCM at a constant water inlet temperature. During solidification, the heater is turned off. The pump continues to circulate water through the circuit during solidification. An air to water heat exchanger cools the water temperature at the inlet to a constant value. This value can be adjusted by changing the temperature of the environmental chamber where the setup is placed. The entire PCM-HX is insulated with foam to minimize heat losses to the surroundings.

The instrumentation used for the evaluation of the heat transfer coefficient is summarized in the Table 3.1. The experiment is repeated three times to ensure repeatability of the data. The standard deviation in the RTD measurements is 0.04°C. The uncertainty associated with the heat transfer coefficient is estimated to be 13%, when the temperature

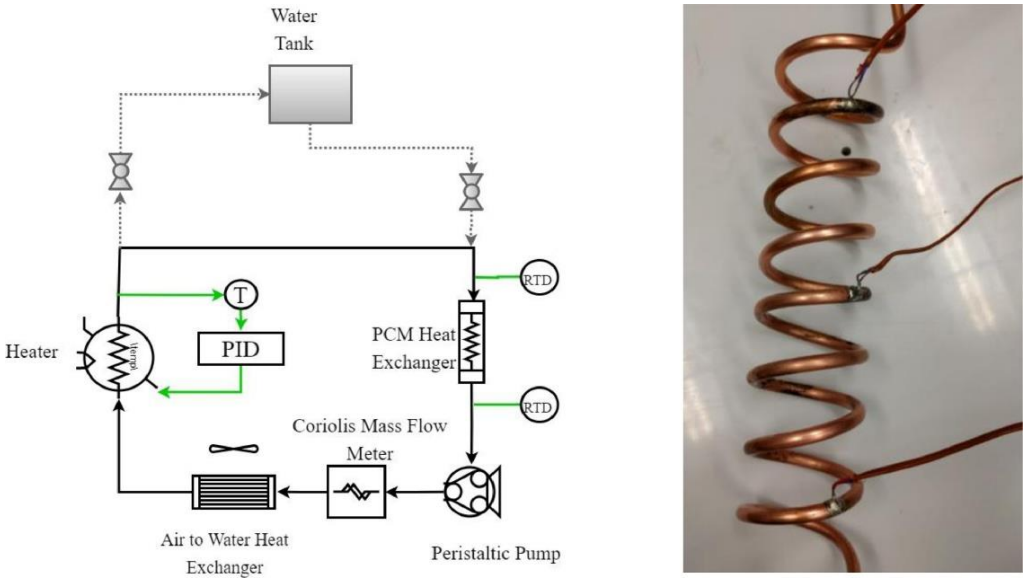

Figure 3.3: Schematic of the setup for evaluating heat transfer coefficient on the shell side of PCM storage and the helical coil used for the experiment

difference between the RTD values is 1.2°C. Three thermocouples are soldered to the helical coil to measure the helical coil temperature, while ten thermocouples are evenly distributed inside the PCM. The average values of these thermocouples provide the tube temperature and lumped PCM temperature used in the determination of the heat transfer coefficient.

Table 3.1: Evaluation of Ideal Cd for CT-A and CT-B

Manufacturer	Device	Accuracy Range	Accuracy Specification
Omega	RTD	0 to 100°C	(0.03)°C
Omega	T-type	-200 to 350°C	0.5°C
Emerson	Coriolis flow meter	0-100 $g\,s^{-1}$	0.2% of flow rate

The results of temperatures measured in the experiment are shown in the Figure 3.4 and 3.5. The flow rate of water is constant during the experiment. Mean value of this

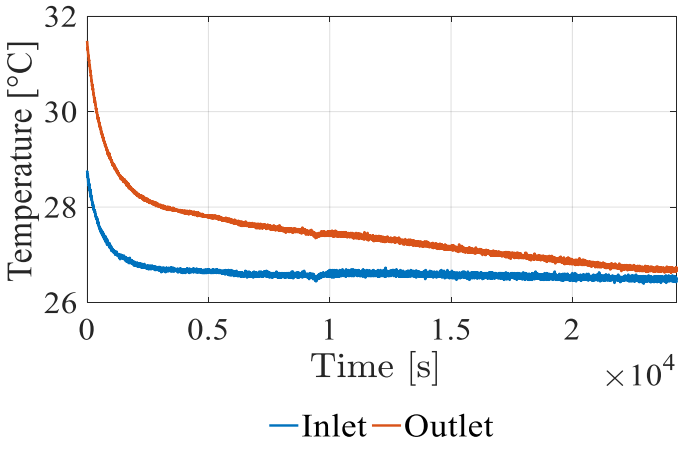

Figure 3.4: Temperatures measured by RTDs (resistance temperature detector) located on the water-side at inlet and outlet of PCM-HX

water flow rate is 3.11 $\mathrm{g\,s^{-1}}$ with a standard deviation of 0.03 $\mathrm{g\,s^{-1}}$.

$$\dot{Q}_{pcm} = \alpha_{pcm} A \left(T_{tube} - T_{pcm}\right) \tag{3.8}$$

The net heat transfer from the PCM to the water is evaluated by Equation (3.9). The temperatures at the inlet and outlet are both provided by the RTD's. The averaged values of the temperatures from Figure 3.3 are used to evaluate the heat transfer coefficient. Equations (3.6) and (3.8) are used to obtain melt fraction as a monotonic function of the lumped PCM temperature (see Figure 3.6).

$$\dot{Q} = \dot{m} c \left(T_{out} - T_{in}\right) \tag{3.9}$$

Finally, the empirical relationship between the heat transfer coefficient and melt fraction is obtained (Figure 3.7). The profile shows that the heat transfer rate decreases as the PCM solidifies from liquid (melt fraction = 1) to solid (melt fraction = 0). This

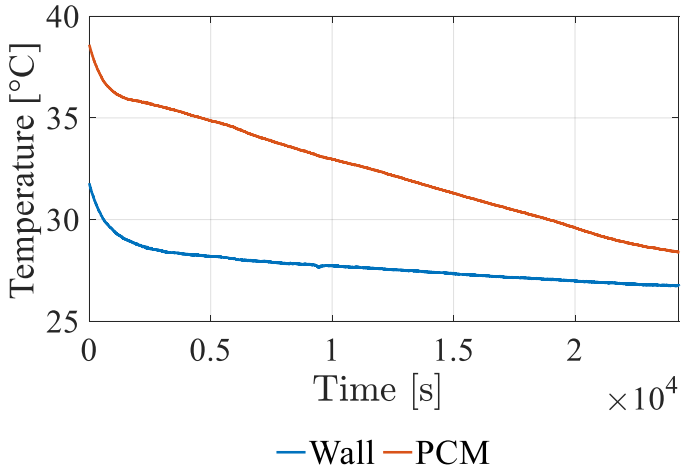

Figure 3.5: Temperatures averaged from the three thermocouples for wall, and ten thermocouples located inside PCM

can be attributed to the decrease in temperature accompanying the phase change, also known as the temperature glide. As the PCM solidifies, its temperature decreases. As a result, the water entering the PCM-HX at a fixed temperature has less heat transferred to it.

3.2.3 Thermosiphon Evaporator Control Volume

The state of refrigerant leaving the PCM-HX is assumed to be saturated vapor since it is a TPTL. After the liquid levels are balanced in the downcomer and riser tubes, the mass flow rate of the thermosiphon depends on the rate of evaporation from the PCM-HX. The mass flow rate in the circuit is calculated from the rate of evaporation of the refrigerant from the PCM-HX. Nominal values of pressure drops are added to various component models to obtain a mass flow rate comparable to the value calculated by back calculation from the airside data. This is done because the mass flow meter is

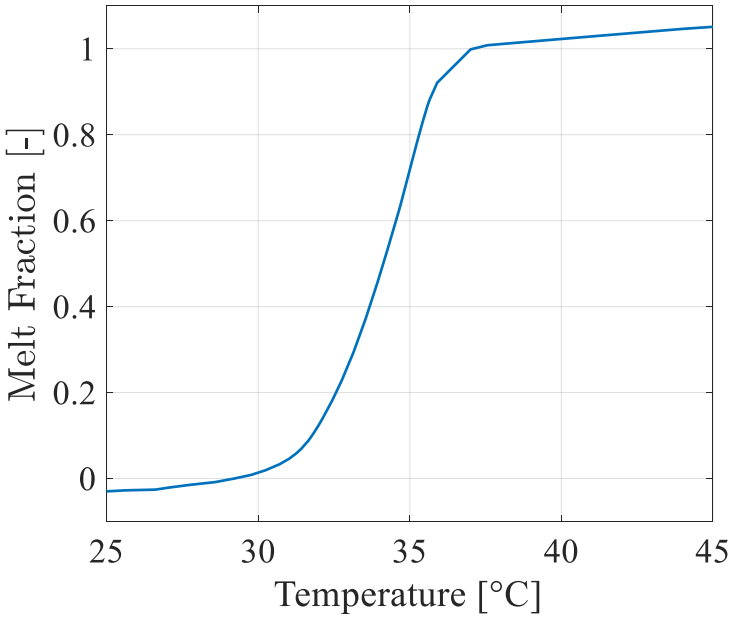

Figure 3.6: Melt fraction as a function of temperature

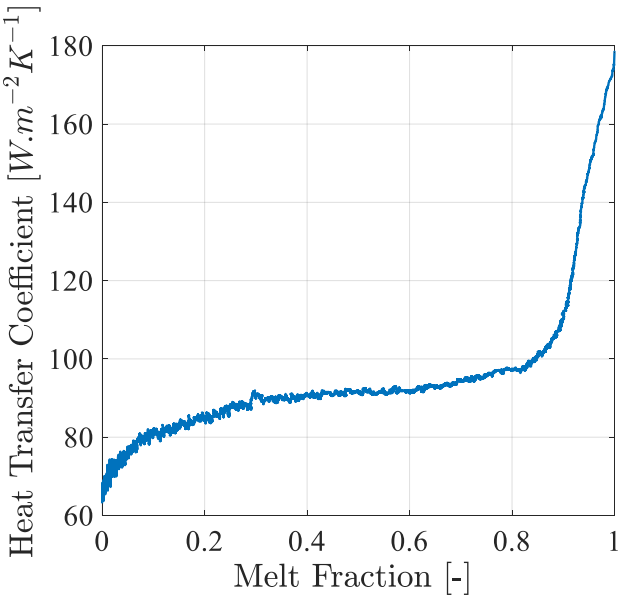

Figure 3.7: Heat transfer coefficient as a function of melt fraction

bypassed in the experimental setup to reduce the pressure head for the refrigerant flow in the thermosiphon operation. Since no experimental measurement of mass flow rate is available, the uncertainty of mass flow rate prediction from the current approach cannot be determined.

Figure 3.8 shows the experimental PCM-HX (left) and the control volume used to model its refrigerant side (right). The lengths of various geometrical parameters are given in Table 3.2. The PCM fills the empty space in the container. The control volume inlet and outlet are modeled using fluidports, while the heat transfer is modeled using the heatport connector. Since the control volume is lumped, the black dot at the center of Figure 3.8 (right) represents the location of the fluid element.

Table 3.2: Geometric parameters of PCMHX

Parameter	Value
Height between Headers [m]	0.315
Length of Header [m]	0.32
Diameter of helix turn [m]	0.41
Number of turns [-]	9
Header tube outer diameter [m]	0.0127
Helix tube outer diameter [m]	0.00635

The total volume of the refrigerant tube (V_{tot}) consists of the volume occupied by the vapor (V_v) and the volume occupied by the liquid refrigerant (V_l). Out of the two properties required to determine the refrigerant state, the first (the average density, ρ_{cv})

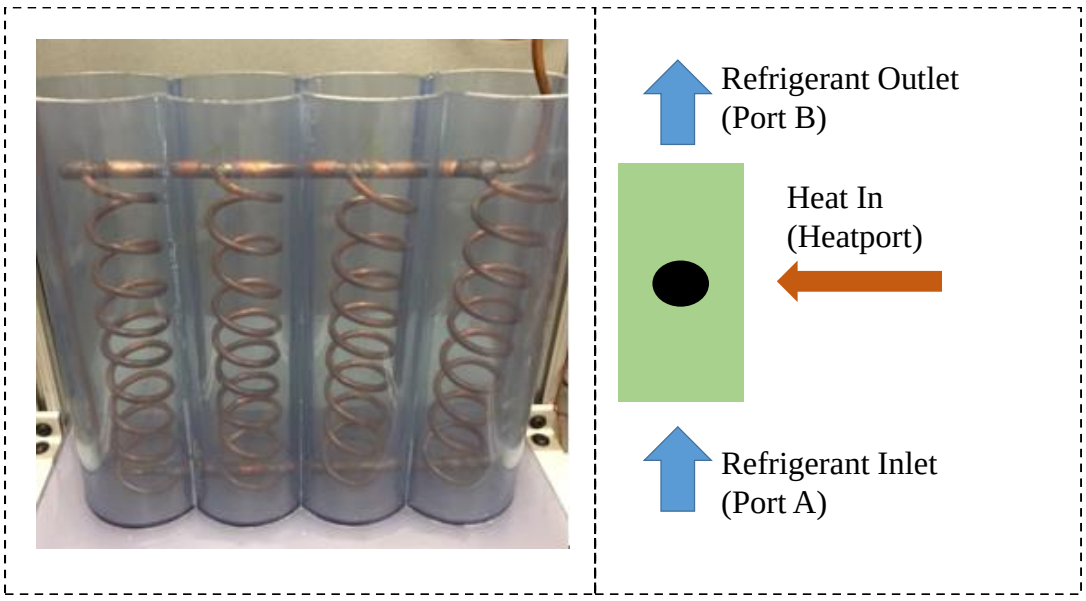

Figure 3.8: PCM-HX used in RoCo and the control volume used for modeling

can be calculated as follows:

$$V_t = V_V + V_L \tag{3.10}$$

$$m = \rho_V V_V + \rho_L V_L \tag{3.11}$$

$$\frac{dm}{dt} = \dot{m}_{in} - \dot{m}_{out} \tag{3.12}$$

$$\rho_{cv} = \frac{m}{V_t} \tag{3.13}$$

The second property (pressure, p_{cv}), can be obtained by averaging the pressure at the inlet and outlet as shown in Equation (3.14).

$$p_{cv} = \frac{p_{in} + p_{out}}{2} \tag{3.14}$$

These two properties are sufficient to determine the state of refrigerant, and all the remaining properties are calculated. Functions are available from the in-house REFPROP 9.0 based library [189] for refrigerant media.

The energy conservation equation (Equation (3.15)) and chain rule of derivatives applied to the partial derivative of density with state variables (Equation (3.16)) are used to update pressure and specific enthalpy, which are the state variables. The partial derivatives of density are also functions of state variables [165] and evaluated using property functions [189].

$$V_t \frac{dh_{cv}}{dt} + h(\dot{m}_{out} - \dot{m}_{in}) + (\dot{m}_{out} h_{out} - \dot{m}_{in} h_{in}) = \dot{Q}_r + V_t \frac{dp_{cv}}{dt} \tag{3.15}$$

$$\frac{\partial \rho_{cv}}{\partial t} = \frac{\partial \rho_{cv}}{\partial p_{cv}}\bigg|_{h_{cv}} \frac{dp_{cv}}{dt} + \frac{\partial \rho_{cv}}{\partial h_{cv}}\bigg|_{p_{cv}} \frac{dh_{cv}}{dt} \tag{3.16}$$

The heat transfer coefficient for heat transfer from the heatport, $\alpha_{r,e}$ in Equation (3.17), is calculated from Shah's correlation [197] with Schmidt correlation [198] for helical coils used for calculating liquid-only heat transfer coefficient. Since enthalpy in the `FluidPort` is defined as a stream variable [199], outflow enthalpies need to be set for both the inlet and outlet. The outflow enthalpy at the outlet, h_{out}, is set as saturated vapor enthalpy, $h_{v,cv}$ in Equation (3.18), while the outflow enthalpy at the inlet port is set as saturated liquid enthalpy, h_{in} in Equation (3.19).

$$\dot{Q}_{r,e} = \alpha_{r,e} A \left(T_{tube} - T_{cv}\right) \tag{3.17}$$

$$h_{out} = h_{V,cv} \tag{3.18}$$

$$h_{in} = h_{L,cv} \tag{3.19}$$

3.3 System Modeling

The nature of PCM-HX model used in the study is relatively simple to reduce the complexity of dynamics of thermosiphon assisted solidification for a system level sim-

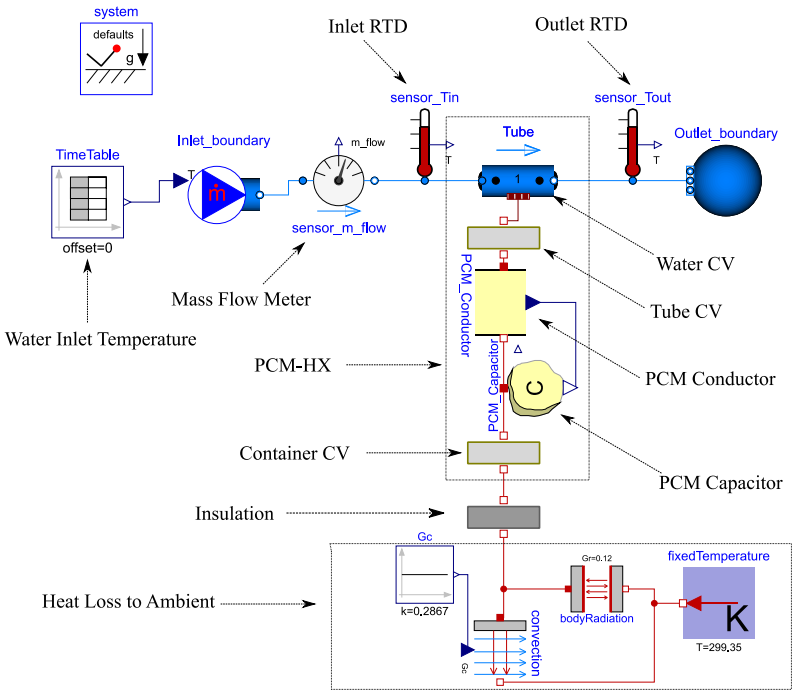

Figure 3.9: Model diagram for solidification experiment with water

ulation. To check the level of accuracy of the PCM-HX model for solidification, the experiment described in Section 3.2.2.3 is simulated. The inlet water temperature from Figure 3.4 and mass flow rate of water is given as input to predict the water outlet temperature. The model diagram for this simulation is shown in Figure 3.9.

Validation plots for solidification experiment with water are shown in Figure 3.10, which compares the temperatures at the inlet and outlet of PCM-HX for the simulation the experimental data. The outlet temperature predicted is within 0.5°C of the experiment. The cumulative error from integrating the temperature difference over the entire time duration is 13.4%. Thus, the PCM-HX model is able to predict the solidification to a reasonable accuracy.

Figure 3.11 shows the model diagram for a thermosiphon using the components developed in the previous section. The experimental data for validation of the model is taken

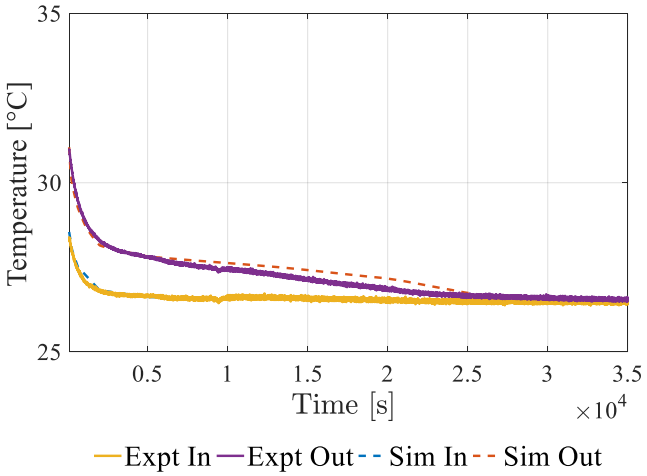

Figure 3.10: Water temperatures at the inlet and outlet of PCM-HX

from Du et al.(2016) [181]. The refrigerant side two-phase heat transfer coefficient values of AC-HX are calculated using Shah [200] correlation, and the heat transfer coefficients for the airside are evaluated using Wang et al. (2000) [201] correlation.

Heat loss from the PCM Container to the surroundings by both natural convection and radiation is modeled. A `TubeWall` is used for modeling the PCM container, and thermophysical properties of PVC (density=1300 $\mathrm{kg\,m^{-3}}$, specific heat capacity=900 $\mathrm{J\,kg^{-1}\,K^{-1}}$, thermal conductivity=0.19 $\mathrm{W\,m^{-1}\,K^{-1}}$) are given as inputs. The heat transfer coefficient for natural convection from the PCM Container wall to the surroundings is calculated using Churchill-Chu correlation [202] for natural convection from vertical plates. For modeling radiation, it is assumed that the PCM Container is a small convex black-body in a large room.

The model is simulated using Radau IIa order 5 stiff solver with a tolerance of 1e-06. Radau IIA is a single-step 3-stage implicit Runge-Kutta method. The details of various available solvers and comparison of their performance can be found in Liu et al. (2010) [203]. The experimental temperature of the PCM at the axis of the helical coil

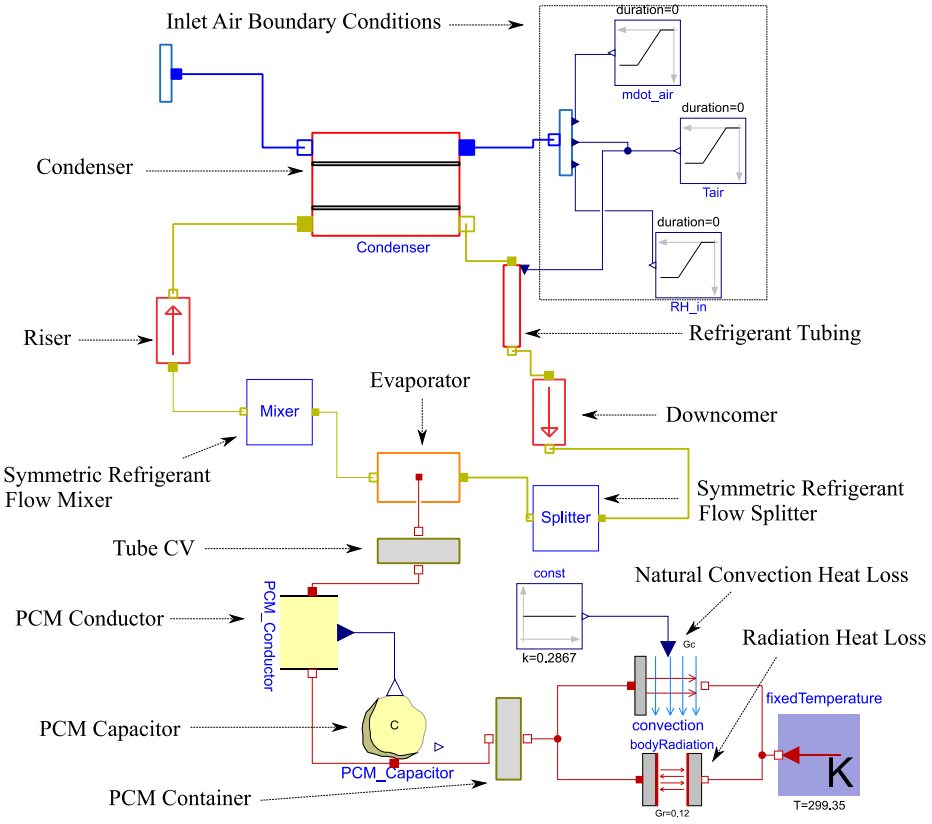

Figure 3.11: Modelica model used for the thermosiphon simulation with pure PCM

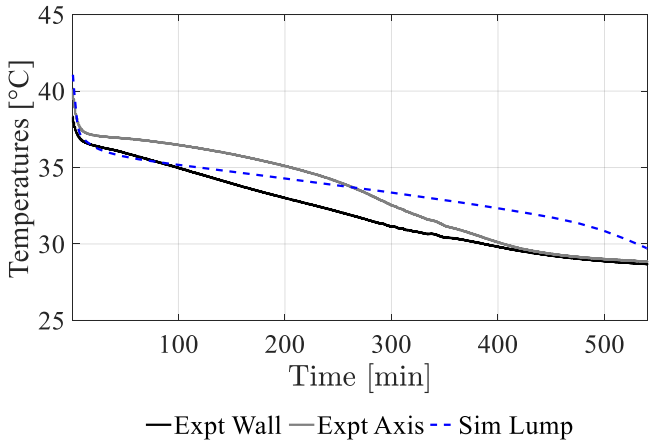

Figure 3.12: PCM temperature comparison between experimental data and simulation

and at the wall (Figure 3.8, left) is compared with the lumped CV temperature from the model in Figure 3.12.

T-Type thermocouples were used for the temperature measurement with the uncertainty of temperature measure of 0.5°C. The thermocouples were calibrated between 0-80°C with 10°C increments. The PCM wall temperature refers to the temperature measured by the thermocouples between the PCM container wall and outside the helical coil. This is lower than the temperature in the axis region of the helical coils because the axis region gets heated from all sides, while the region outside the helical coil dissipates heat to the ambient. The thermocouple temperature falls faster than the simulation temperature because the thermocouples are located close to the helical coil, and they may not be exact representation of volume averaged temperature of the entire lump of PCM.

Figure 3.13 shows the comparison of the condenser airside temperatures to the experimental data. Though there is a slight mismatch in the initial part of the cycle, which can be attributed to lack of a receiver model in the simulation model, the model can

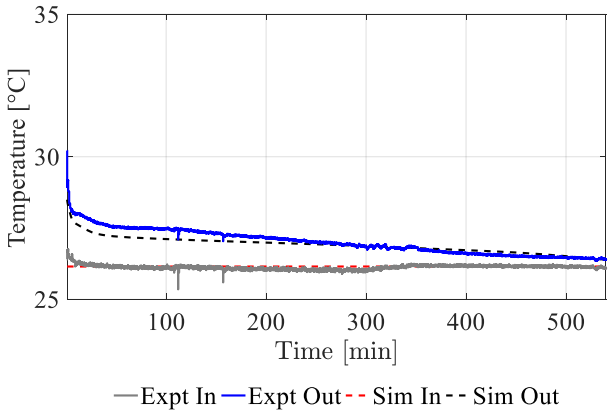

Figure 3.13: Condenser airside temperature comparison between experimental data and simulation

accurately predict the discharge time and can be used for the material selection study. Four T-Type thermocouples were installed each at the inlet and outlet of the condenser to measure the airside temperatures. Details of installation and uncertainty of the measurement are available in [204]. The heat losses from both convection and radiation to the surroundings contribute to 22% of heat losses. Thus, it is important to model these heat losses for accurate simulation of solidification.

3.4 Evaluating Performance of Graphite Enhanced PCM

Thermal conductivity enhancement of the PCM enables faster discharge than a pure PCM system. Compressed expanded natural graphite (CENG) foam is of interest due to the low density and high thermal conductivity of the material. Recall that the `PCM Conductor` component requires the heat transfer coefficient vs melt fraction as an input. Consequently, the heat transfer coefficient for the composite can be evaluated using the 2-D finite element model. Details of the assumptions and calculations involved in calculation

of the heat transfer coefficients are presented in Dhumane et. al (2018) [205] and only the results are presented here.

Table 3.3: Properties of PCM and PCM composites

CENG Vol. Fraction %	Solid Density $kg\,m^{-3}$	Liquid Density $kg\,m^{-3}$	Solid Sp. Heat $J\,kg^{-1}\,K^{-1}$	Liquid Sp. Heat $J\,kg^{-1}\,K^{-1}$	Latent Heat $J\,kg^{-1}$	Thermal Conductivity $W\,m^{-1}\,K^{-1}$
0	920	840	2210	2630	210	0.2
0.5	927	847	2192	2605	208	1.1
1.0	934	854	2173	2578	205	2.3
2.2	950	871	2131	2520	200	4.7
4.4	979	903	2057	2417	187	9.6
6.3	1005	930	1997	2335	178	20.2

The thermo-physical properties of the PCM used in comparison are shown in Table 3.3. Heat transfer coefficient evaluated from simulation are presented in Figure 3.14.

The inlet air temperature for discharge operation is 79°F (26.15°C). The thermal storage consists of four PCM cylinders with a height of 1.2 m. Thus, the total surface area for heat transfer is kept same across all the evaluated PCM's for performance comparison. The air flow rate of the fan blowing on the AC-HX is 80 cfm ($0.038\ m^3\,s^{-1}$). The discharge time for the pure PCM is calculated from the pure PCM simulation to be 554 minutes with the final 10% taking up 114 minutes. For good cyclic efficiency, it does not make sense to solidify the material to 0% liquid, and so the discharge time for the baseline case is taken to be 440 minutes. Consequently, due to the poor thermal conductivity of pure PCM, the thermal storage needs to be slightly oversized since the PCM residing at further ends of

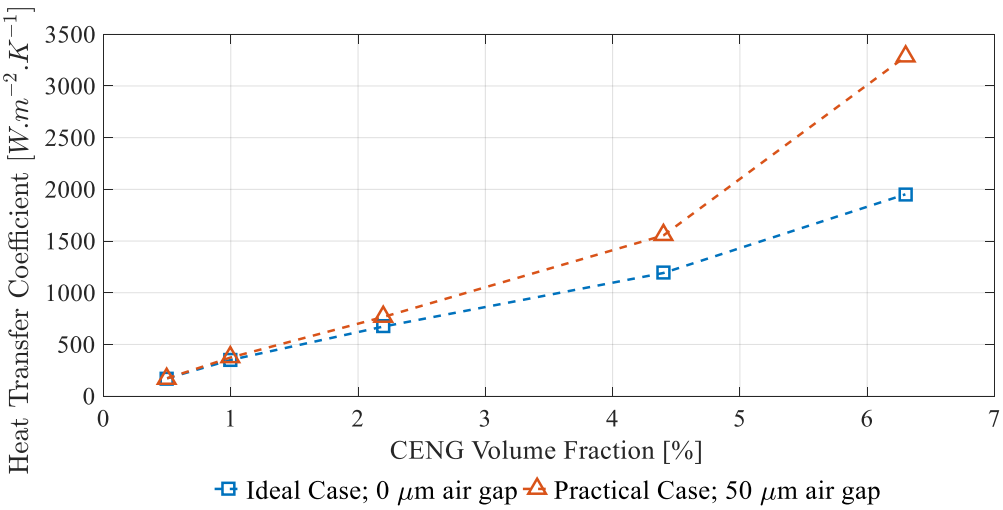

Figure 3.14: Average heat transfer coefficient as a function of CENG volume fraction

the storage from the heat source or sink are difficult to melt or solidify. The heat transfer coefficient for boiling in straight tubes is evaluated using Shah correlation [197]. The total thermal storage capacity is maintained constant across all PCM's. The CENG thermal storages are assumed to be four cylindrical blocks with refrigerant flowing through the axis. The cross-section details evaluated with these considerations are shown in Table 3.4. Discharge time, weight, and volume are normalized to that of RoCo (440 minutes) and plotted in Figure 16 using the heat transfer coefficients for the practical case shown in Figure 3.15.

The temperature profile of the PCM for the CENG PCM is plotted in Figure 3.16. The initial sharp drop in temperature corresponds to sensible heat in the liquid phase. The amount of heat stored as sensible heat is much lesser than the latent heat and is easily released. The next portion corresponds to latent heat while the PCM solidifies from liquid to solid. The slope increases with the increased amount of graphite in CENG. Finally, the sharp drop corresponds to sensible heat in the solid phase of the PCM. As the PCM

Table 3.4: CENG thermal storage geometry

CENG Vol. Fraction	CENG Bulk Density	PCM OD Ideal	PCM OD Measured
%	$kg\,m^{-3}$	mm	mm
0.5	11	75	75
1.0	23	75.4	75.4
2.2	50	76.1	76.1
4.4	100	77.4	81.1
6.3	143	78.7	91.9

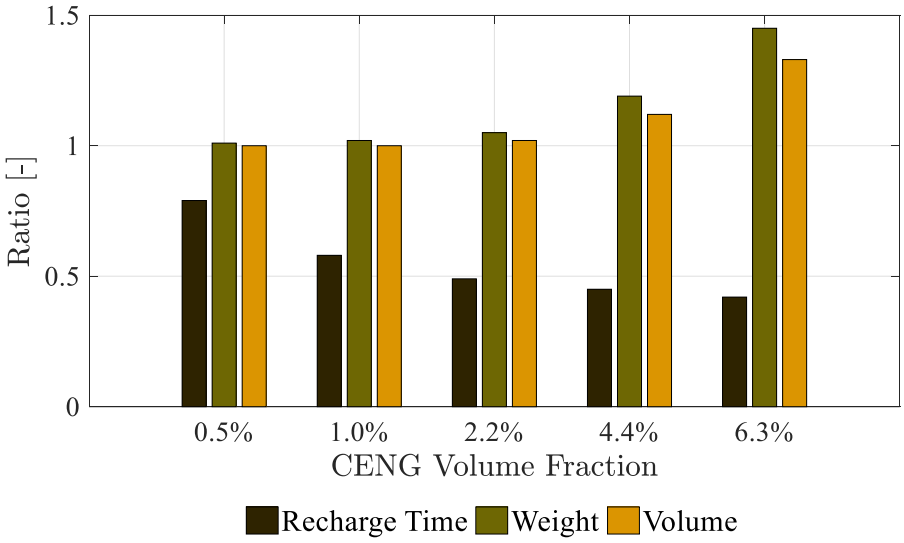

Figure 3.15: Relative performance of various CENG composites capable of a two-hour operation time

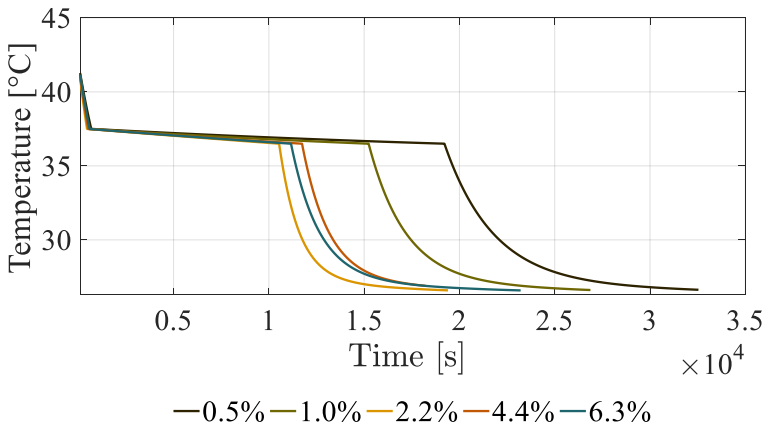

Figure 3.16: Temperature profile during thermosiphon operation with enhanced graphite thermal storage

reaches the ambient temperature, the heat release rate decreases and so the temperature of PCM approaches the ambient temperature asymptotically.

Figure 3.17 shows the different rate of heat release from the PCM. As expected, the higher graphite content leads to increased heat release rate. This leads to the faster recharge time since the net heat stored is the same for all the thermal storages. The temperature profiles are much different than the pure PCM case shown in Figure 3.12. This can be attributed to the lack of natural convection in CENG. The graphite foam blocks passages for liquid PCM to develop convection current. Additionally, the higher thermal conductivity reduces the temperature gradient that drives natural convection.

The results obtained in the previous section suggest that there is a significant reduction in the discharge time if the thermal storage is made from CENG. The thermosiphon operation requires continuous operation of a 10-W fan for the duration of the discharge process. Thus, shortening the process results in an increased coefficient of performance (COP) for the operation. Du et al. (2016) [181] reported the COP of the VCC equal to

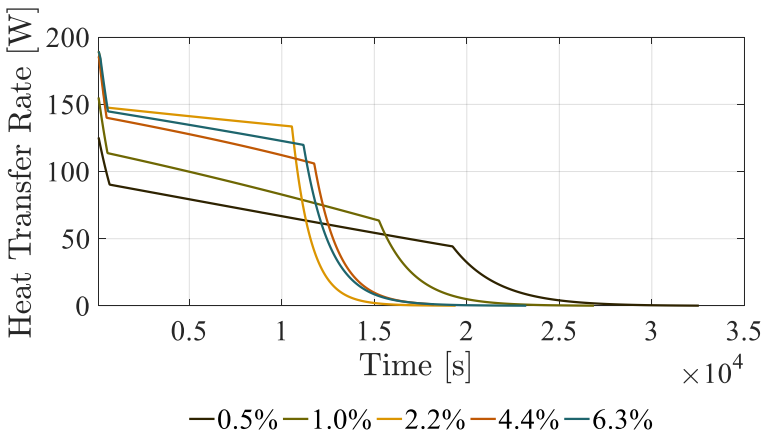

Figure 3.17: Heat removal rate during thermosiphon operation with enhanced graphite thermal storage

2.85. The system COP for RoCo should incorporate the power consumed during both the cooling as well as the recharge process.

For the present analysis, the COP for the VCC will be assumed constant for all the variations of thermal storage. In reality, the CENG thermal storage will have lower condenser temperature due to improved thermal conductivity and will further enhance the COP. The evaporator capacity reported by Du et al.(2016) [181] is 165.6 W for a period of two hours. This value is averaged value over the two hour period. Average power consumption for the two-hour interval can be calculated from Equation (3.20) = 58.1 W.

$$COP_{vcc} = \frac{\bar{\dot{Q}}}{\bar{\dot{W}}_{vcc}} \tag{3.20}$$

$$COP_{tot} = \frac{\bar{\dot{Q}}\Delta t_{vcc}}{\bar{\dot{W}}_{vcc}\Delta t_{vcc} + \bar{\dot{W}}_{ts}\Delta t_{ts}} \tag{3.21}$$

Equation (3.21) can be used to evaluate the overall COP for RoCo. This incorporates the energy consumed during both recharge and discharge processes. The results for all the cases are presented in Figure 3.18. It can be observed that the COP is in the range

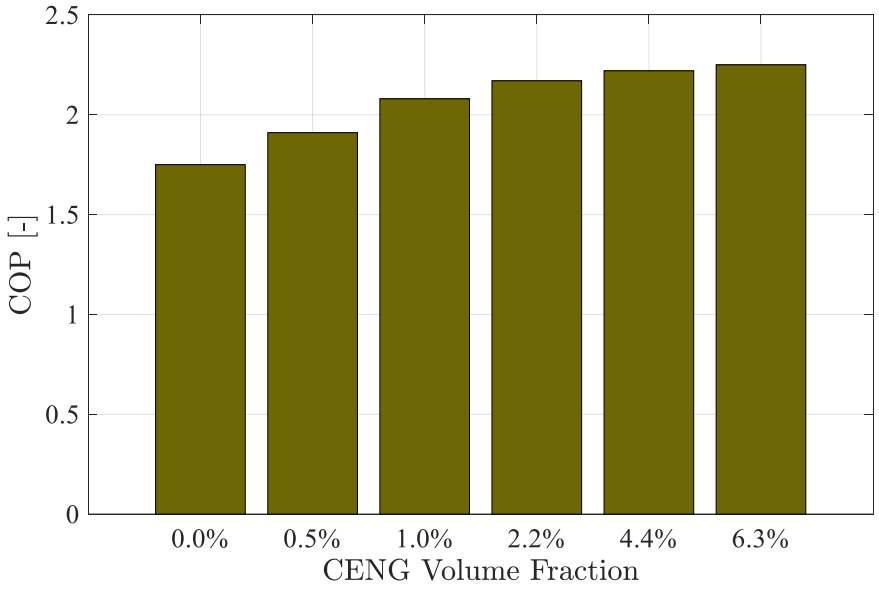

Figure 3.18: COP of RoCo for the different thermal storage options

of 1.75 to 2.25 for all the PCM composites. The COP can be increased by as high as 29% for the CENG with the volume fraction of 6.3%.

Recharge time may also be increased by using a PCM which solidifies at a higher temperature. This will provide a larger potential for the temperature gradient to solidify the PCM at a faster rate. Increasing the phase change temperature of thermal storage will, however, decrease the COP of VCC operation. Dynamic simulations of both VCC and thermosiphon will be used to find the appropriate set of phase change material and enhancement options for a longer cooling operation for RoCo.

Chapter 4: Performance Improvements of Personal Conditioning Systems

4.1 Introduction

The present chapter seeks to provide design insights for increased overall coefficient of performance of Roving Comforter. Dynamic model for modeling the thermosiphon based recharge was developed in the previous chapter and used to understand performance improvement from graphite enhancement to phase change material. Two other ideas for improvement of the performance are discussed: one is switching to a natural refrigerant R290 and second is using a heat pump based recharge.

4.2 Performance with a natural refrigerant

The current RoCo prototype uses R134a as the refrigerant, primarily due to lesser safety concerns related to the flammability, enabling development in a university laboratory. Secondly, the wider experience of development of systems with R134a enables the researchers to focus on improving the novelty aspects of the prototype and fewer design challenges. R134a is a hydrofluorocarbon (HFC) and has zero ozone depletion potential, however, its global warming potential (GWP) is 1300 [206]. Thus, it is a potent greenhouse gas and is thousands of times more potent than carbon dioxide in contributing to

climate change. If HFC growth continues on the current trajectory, the increase in HFC emissions is projected to offset much of the climate benefit achieved by phasing out the ozone-depleting substances which were replaced by the HFCs [207].

As R134a is affected by the Kigali Agreement under the Montreal Protocol [208], it should be gradually phased out and replaced by low-GWP alternatives. The miniature hermetic rotary compressor [180] used in the Roving Comforter is compatible with R134a, R404A, R600a and R290. Hydrocarbon (HC) refrigerants have equal or better heat transfer performance and lower pressure drop compared to R134a [209]. Other expected benefits from switching an HFC to HC are higher efficiency, lower charge quantity and lower compressor discharge temperature [210].

The cooling operation of RoCo is modeled using `CEEEModelicaLibrary` [165]. The model is validated with experiment data for RoCo working with R134a and then used for comparing system level performance of the Roving Comforter with propane (R290) as a refrigerant in comparison with the current R134a.

4.2.1 Empirical PCM heat transfer coefficient

Experiment is conducted to obtain the heat transfer coefficient of PCM for melting in helical coils. Unlike the solidification, melting of PCM involves heat transfer by both conduction and natural convection.

The schematic of the experiment for evaluating the heat transfer coefficient for melting is the same which was used for solidification (see Figure 3.3). The equations and procedure for calculation of heat transfer coefficient is presented in 3.2.2.3 and skipped here for brevity.

The thermal conductance on the water-side is calculated using water flow conditions.

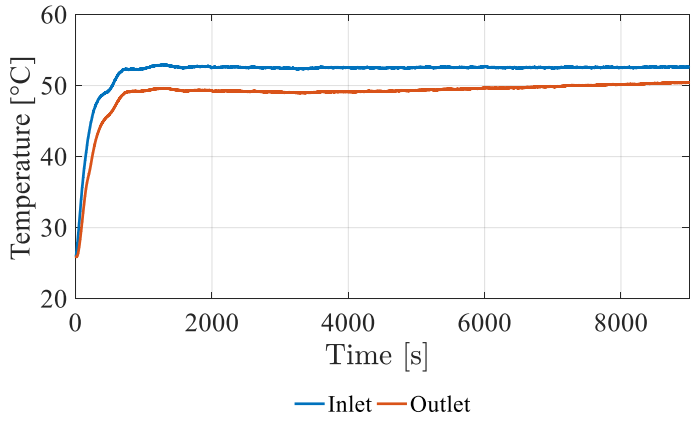

Figure 4.1: Temperatures at the inlet and outlet of PCM-HX

During the modeling of PCM-HX, the refrigerant flow conditions are used to estimate refrigerant side thermal conductance. The water inlet temperature equals the temperature of condensation of refrigerant in PCM-HX. The temperature drop of water during the test is negligible and can represent the isothermal melting conditions in condenser. The empirical equation captures the variation of the heat transfer coefficient on the shell side of PCM storage as a function of liquid fraction. The uncertainty in the evaluation of the heat absorbed by the PCM is 8.3%, while the uncertainty in the measurement of the heat transfer coefficient is 10.2%.

The temperature of water entering the PCM-HX is selected as 50°C to provide melting at temperature similar as the condenser of RoCo. The temperature difference between the RTD's is shown in Figure 4.1. It can be observed that the temperature difference is small enough to make assumption of isothermal melting. A peristaltic pump is used for circulating water through the water loop shown in Figure 3.3. Reducing the water flow rate produces oscillations in the flow, while increasing it reduces the temperature difference between RTD's leading to lesser uncertainty in the value of the heat transfer

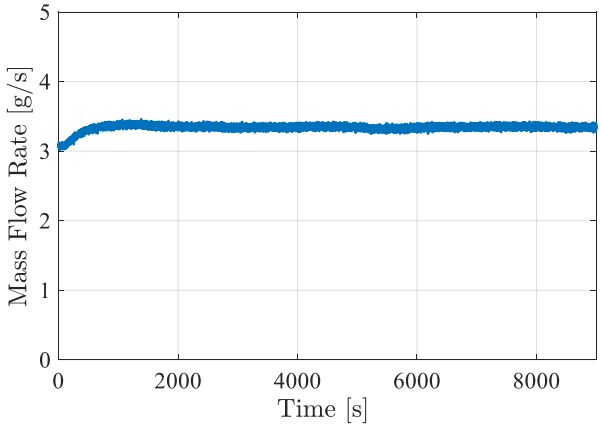

Figure 4.2: Mass flow rate of water flowing through PCM-HX

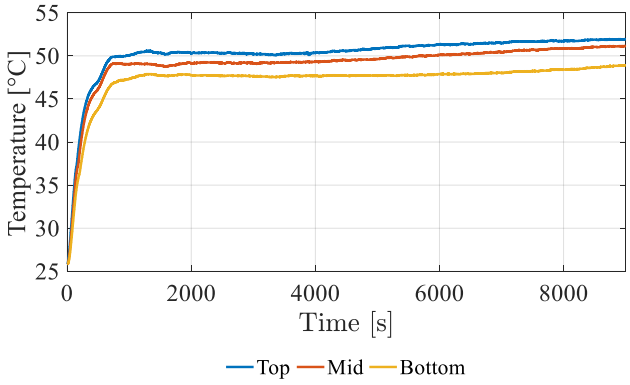

Figure 4.3: Temperatures of the thermocouple on PCM-HX tube

coefficient. The mass flow rate of water shown in Figure 4.2 is the optimal point accounting both these considerations.

The temperature of thermocouples located on the tube (see Figure 3.3) are shown in Figure 4.3. Even though thermocouples were placed at various locations inside the PCM, they do not provide good estimates of volume averaged PCM lumped temperature. Consequently, the net heat absorbed by the PCM over time is integrated to obtain PCM enthalpy. DSC curve provides enthalpy temperature profile for the PCM, and it can now be used to evaluate lumped PCM temperature from the enthalpy. For the material

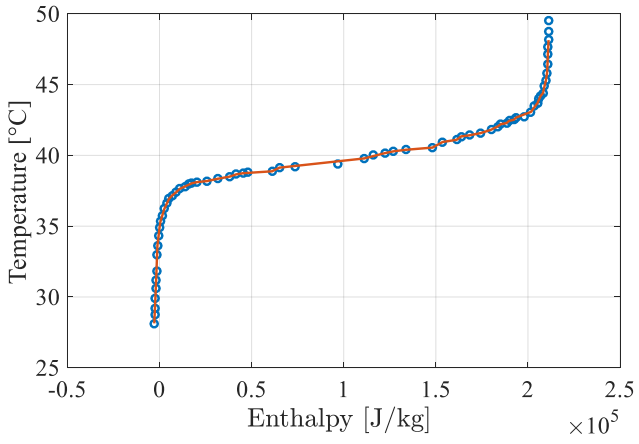

Figure 4.4: Enthalpy temperature function obtained from DSC data

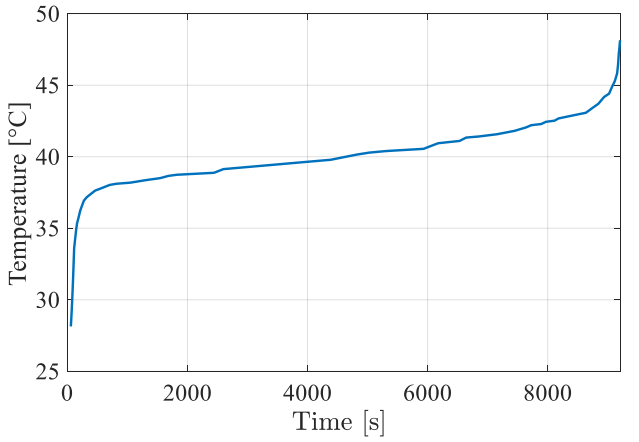

Figure 4.5: Lumped PCM Temperature obtained from Enthalpy

PureTemp 37 [168], the DSC temperature profile from Mallow et al. (2018) [211] is used. The enthalpy temperature function obtained from it is shown in Figure 4.4. It is obtained by using Equation (3.5).

The lumped PCM temperature obtained from the enthalpy temperature function is shown in Figure 4.5. It can be noted that the temperature is increasing during the melting process, showing that the glide is successfully captured. Finally, the heat transfer coefficient relation with melt fraction is obtained (Figure 4.6).

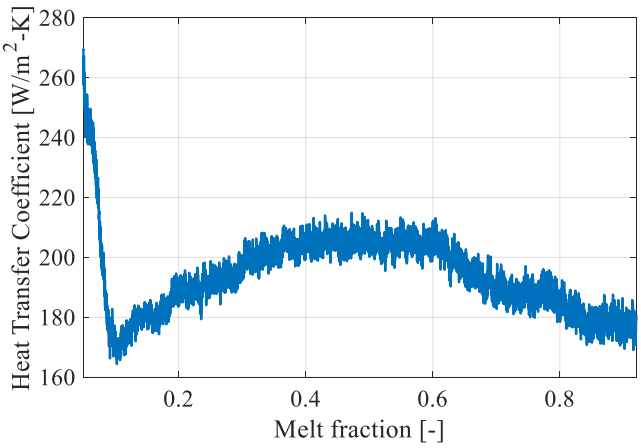

Figure 4.6: Melting HTC as a function of melt fraction

The profile provides insight on the melting of PCM in helical tubes. In the lower melt fraction region ($\lambda < 0.1$), as the solid starts to melt, the heat transfer is reduced because the liquid PCM has less space to circulate leading to poor natural convection. The heat transfer coefficient rises in the middle portion due to the increase in the velocity of PCM from the availability of increased space for liquid PCM flow. After reaching the peak ($\lambda = 0.5$), the heat transfer coefficient decreases. This decrease is due to a more uniform temperature developed by the natural convection stirring. The uniformity in temperature leads to a decreased buoyancy force for convection and lesser heat transfer. Similar profile has been observed during the melting of PCM in a tall enclosure heated by wall and also a straight tube immersed in PCM by [212] and [96] respectively.

4.2.2 Simulation of Cooling Operation of Roving Comforter

With the component model available for PCM-HX, the complete system model can now be developed as shown in Figure 4.7 and simulated. The system contains a compressor, expansion valve, evaporator (an air to refrigerant heat exchanger), refrigerant tubes and

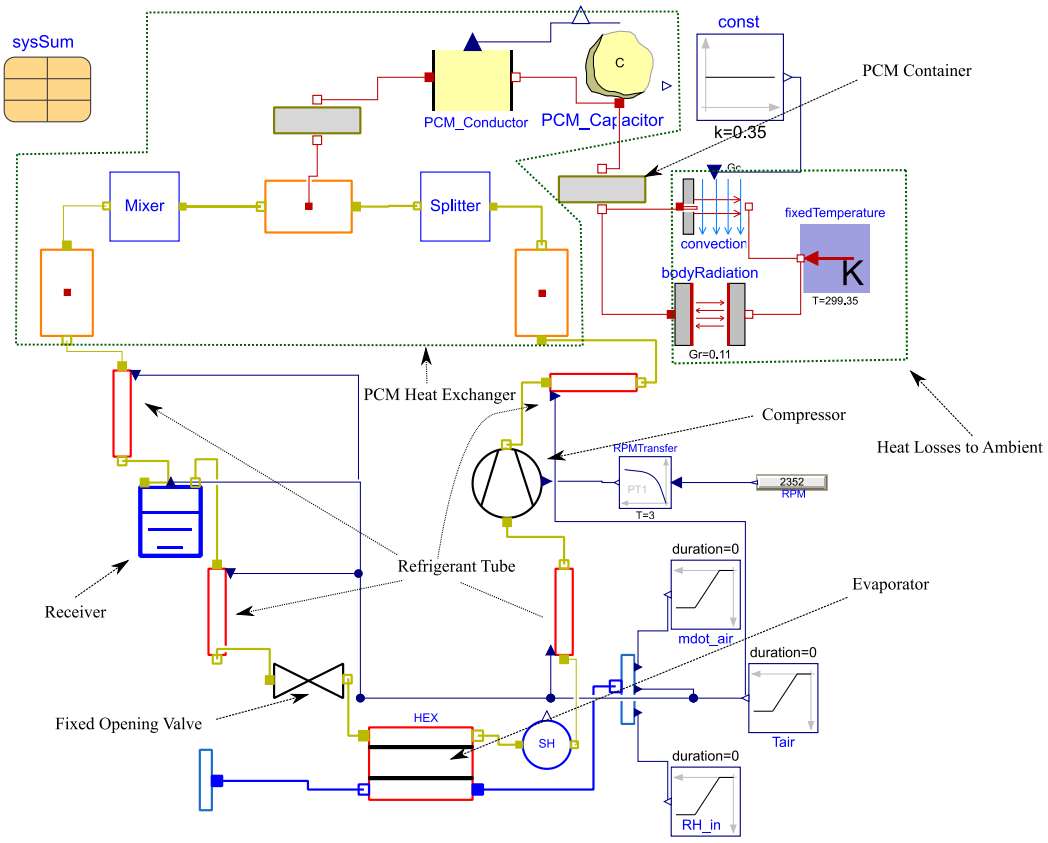

Figure 4.7: Model diagram for cooling cycle of Roving Comforter

a receiver. The models for these components were developed by Qiao et al. (2015) [165] and the discussion is skipped here for brevity. However, the method of selecting input parameters for a few of these parameters is discussed here.

The different control volumes discussed in Section 3.2.2 are marked inside the green box in Figure 4.7. The flow in each of the four helical coils of the PCM-HX (see Figure 3.8) is assumed to be symmetric. So, only a single section is modeled. The refrigerant flow is divided by four by `Splitter`, and then scaled back by `Mixer`. Lumped refrigerant control volumes are used to model the headers of the PCM-HX. The headers are assumed to be adiabatic and the entire heat transfer to the PCM is modeled from the helical coil. In

reality, there is a definite heat transfer between the headers and the PCM. However, it is difficult to evaluate the exact heat transfer from the headers to the PCM in the presence of helical coils. The headers have straight refrigerant tubes and the heat transfer from straight tube to PCM is much lesser than helical coils. This is due to the low thermal conductivity of PCM. As can be observed in the validation, the error arising from this assumption is insignificant.

The heat losses from the PCM container are also modeled for improved accuracy. The total heat transfers involved between the refrigerant and PCM are of the order of 200 W and the heat losses by radiation and natural convection need to be accounted. The PCM container is modeled using the `TubeWall` volume component. The material properties of PVC are provided as input for it, instead of copper when modeling the refrigerant tube using the same component. This demonstrates the benefits of versatility and re-usability of Modelica models in development of complex systems and the resultant faster model development time is one of the reasons for its preference for current investigation. Finally, `Convection` and `BodyRadiation` components from the Modelica Standard Library `Modelica.Thermal.HeatTransfer.Components` are used to model the natural convection and radiation losses, respectively. These models require the thermal conductance as input, and use linear and fourth power difference respectively to calculate the required heat transfer. For estimating the natural convection heat transfer coefficient [202] is used.

The evaporator is a round tube plain fin heat exchanger. It is modeled using a finite volume discretized model. The airside heat transfer coefficient is estimated using [213] correlation. The refrigerant side for evaporator is modeled using [214] correlation. The refrigerant side modeling follows the similar approach of alternating control volume and flow models. Some tubes may have single phase refrigerant, which is estimated using [215]

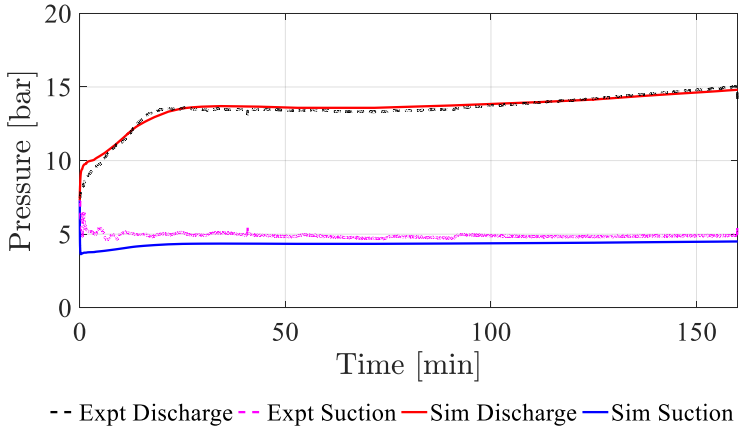

Figure 4.8: Validation of Suction and Discharge Pressure of RoCo

correlation. The refrigerant flow in tubes is expected to be single phase and again estimated using [215] correlation. Pressure drop on the air-side of the evaporator is ignored, since it is negligible. The refrigerant single phase pressure drop is estimated using [216] correlation. The two phase pressure drops are estimated using [217] correlation.

The model is simulated using Dymola 2018 (Dassault systemes, 2018) Radau IIa solver and tolerance setting of 1e-6. The comparison of the pressure prediction of the model and the experiment conducted by Du et al. (2016) [181] is shown in Figure 4.8. The regions of low melt fraction (<0.1) have higher heat transfer coefficients (See Figure 4.6) and so the discharge pressure is less in this region. The natural convection effects start to increase the heat transfer coefficient in the region of 0.1-0.5. This bring about a small dip in the discharge pressure profile. Finally, as the melt fraction increases from 0.5, the heat transfer coefficient decreases and the discharge pressure keeps on rising.

The mass flow rate comparison is shown in Figure 4.9. The poor heat transfer to the PCM in this region also increases the compressor power. The compressor power is plotted in Figure 4.10. The R134a compressor efficiency is tuned to match the power

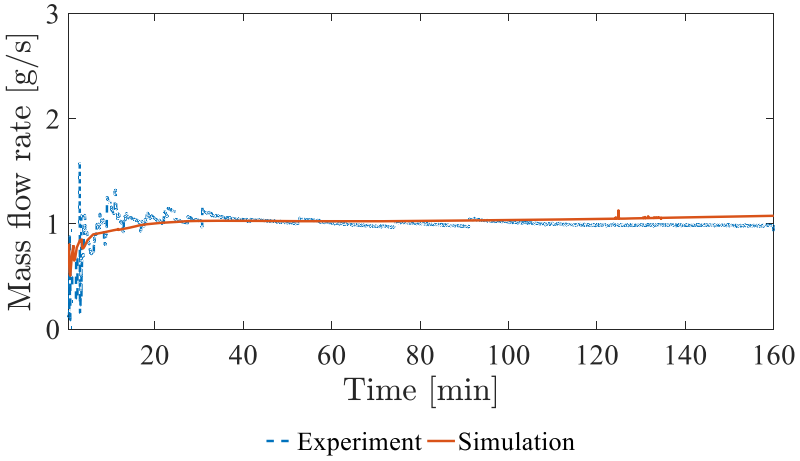

Figure 4.9: Validation of Mass Flow Rate of RoCo

profile obtained from the experiment for R134a. The values that provided good fit are (isentropic efficiency = 0.75, volumetric efficiency =0.95, motor efficiency = 0.85).

The experiment involved the use of a variable opening valve which was modulated throughout the experiment to maintain a fixed superheat. However, this phenomenon is not modeled in the simulation. The heat transfer from headers inside phase change material is ignored in the model. This would lead to a slightly lesser quality at the inlet of evaporator leading to higher evaporator cooling capacity in the experiment (Figure 4.11).

4.2.3 Comparison of RoCo performance with R134a and R290

For comparison with R290, it is assumed that these values remain the same. The R290 simulation is initialized with same saturation temperature and quality distribution as the R134a system. The valve opening and compressor RPM are adjusted to match the cooling capacity, superheat and subcooling of the R134a system. The total cooling capacity is shown in Figure 4.12.

The suction and discharge pressures for operation of RoCo with the R134a and R290

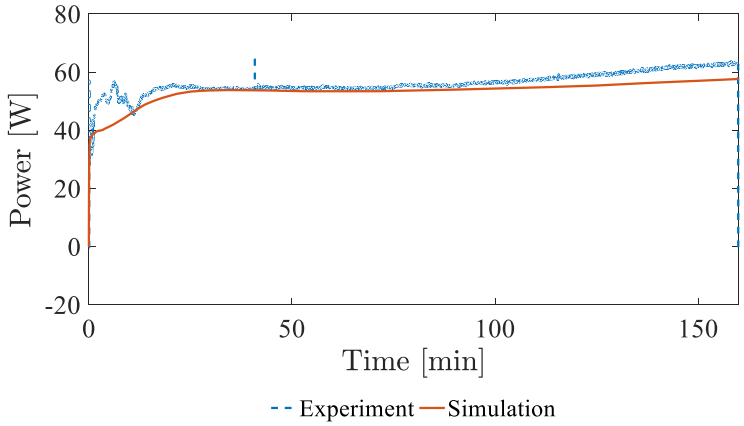

Figure 4.10: Validation of Compressor Power of RoCo

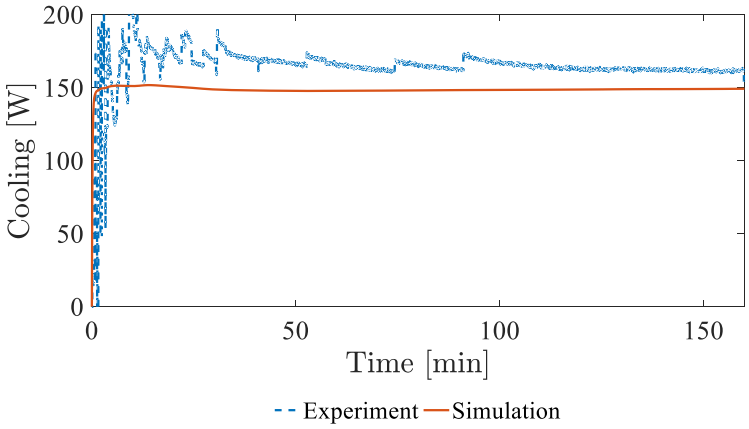

Figure 4.11: Validation of Measured Cooling Capacity

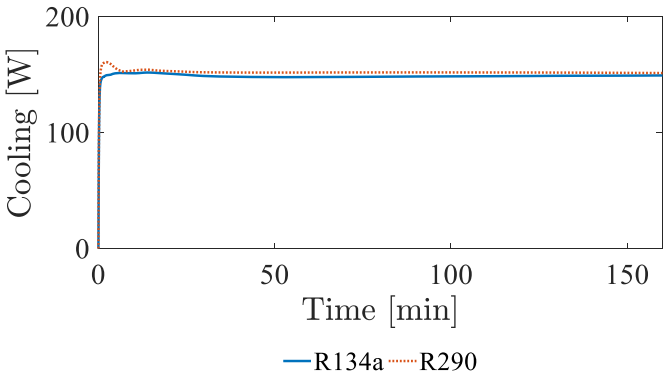

Figure 4.12: Comparison of cooling capacity

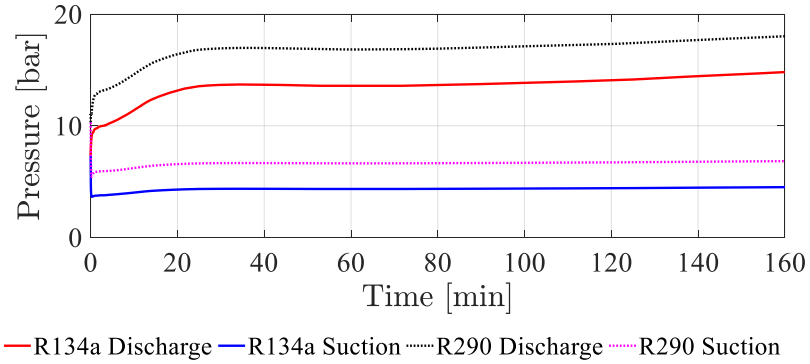

Figure 4.13: Comparison of operating pressures

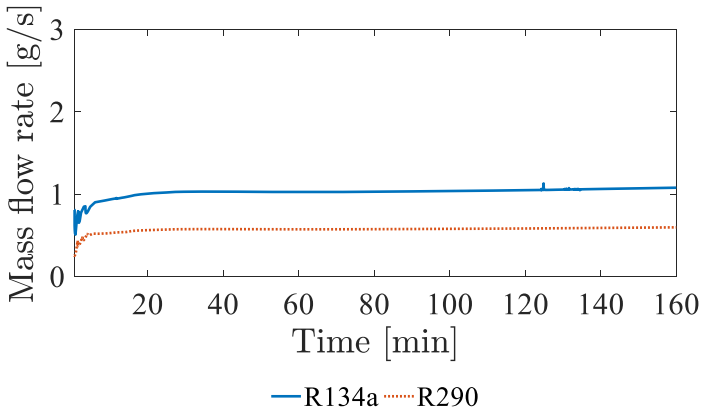

Figure 4.14: Comparison of mass flow rate

are shown in Figure 4.13. The R134a system operates between 5 bar and 14 bar pressure, while the R290 system operates between 7 bar and 17 bar.

The refrigerant flow rate for the R134a system is 1 $\mathrm{g\,s^{-1}}$, while that for the R290 system is 0.6 $\mathrm{g\,s^{-1}}$ as shown in Figure 4.14. The high latent heat of R290 enables operation of the similar capacity system at lower mass flow rate. This reduces the compressor power and increases the coefficient of performance (COP) of the R290 system.

The compressor efficiency is assumed to be the same for the case of both R134a and

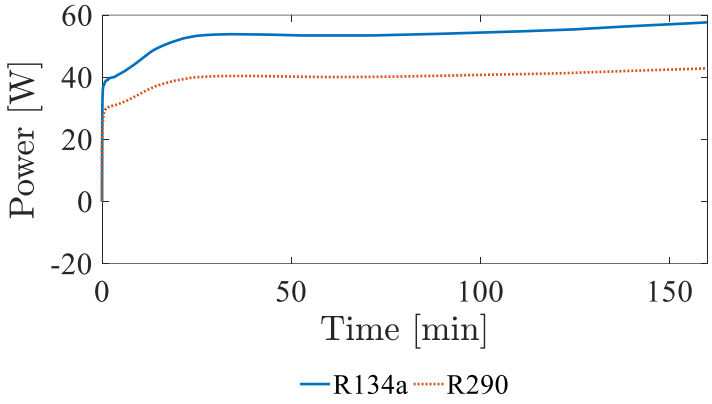

Figure 4.15: Comparison of compressor power

R290. Compressor power comparison is shown in Figure 4.15.

The COP of the system is evaluated as the ratio of integrated cooling capacity and the integrated compressor power during the time interval of operation. The COP for R134a cycle evaluated from the simulation is 2.55, while for the R290 cycle is 3.40. The benefits in COP for the R290 system primarily arise from the higher latent heat of R290, combined with improved heat transfer and pressure drop performance of the system. At 40°C, the latent heat capacity of R290 is 306 $\mathrm{kJ\,kg^{-1}}$, while it is 163 $\mathrm{kJ\,kg^{-1}}$ for R134a [209]. Additionally, the lower RPM of compressor for the R290 system will result in lesser noise during its operation.

The homogenous void fraction model used for prediction of refrigerant charge in the system. The R290 system requires 36% of the refrigerant charge of R134a system. The less amount of charge may lead to smaller size of refrigerant tubing, leading to a smaller weight of RoCo, which will benefit its portability. For a fixed maximum weight, more phase change material can be added to the R290 RoCo leading to a longer cooling operation.

4.3 Analysis of heat pump based recharge

The thermosiphon operation period may be reduced significantly by enhancing the thermal conductivity of PCM using graphite. To achieve more savings from the use of RoCo, the cooling operation period needs to be increased and the recharge time decreased. With this objective, the PCM storage in newer versions of RoCo are developed using the graphite enhanced PCM. The amount of PCM is increased to support four hour cooling operation. Another option for solidification is to reverse the refrigerant flow in circuit and solidify the PCM by making the PCM-HX as an evaporator. This mode of operation will be referred to as heat-pump mode for recharge. The air-cooled heat exchanger now operates as a condenser and rejects heat to the ambient. Heat pump mode utilizes the compressor for its operation resulting in higher power consumption, but is expected to solidify the PCM much faster. The focus of the present section is to explore the advantages and disadvantages of thermosiphon and heat pump operation for solidification of PCM.

4.3.1 Heat Pump System Description

The schematic of the two operations for recharge of RoCo is shown in Figure 4.16. Recall that the refrigerant circuit of RoCo using thermosiphon for recharge involves two ball valves, which by-pass the compressor and expansion device from the refrigerant circuit for cooling cycle. Details of this thermosiphon operation is available in Chapter 3 and omitted here for brevity. As discussed in the Section 3.4 the recharge time of the thermosiphon can be significantly enhanced by addition of graphite to the phase change material (PCM). The systems discussed in the current research use these graphite enhanced PCM. For further value addition from RoCo, the cooling operation duration for

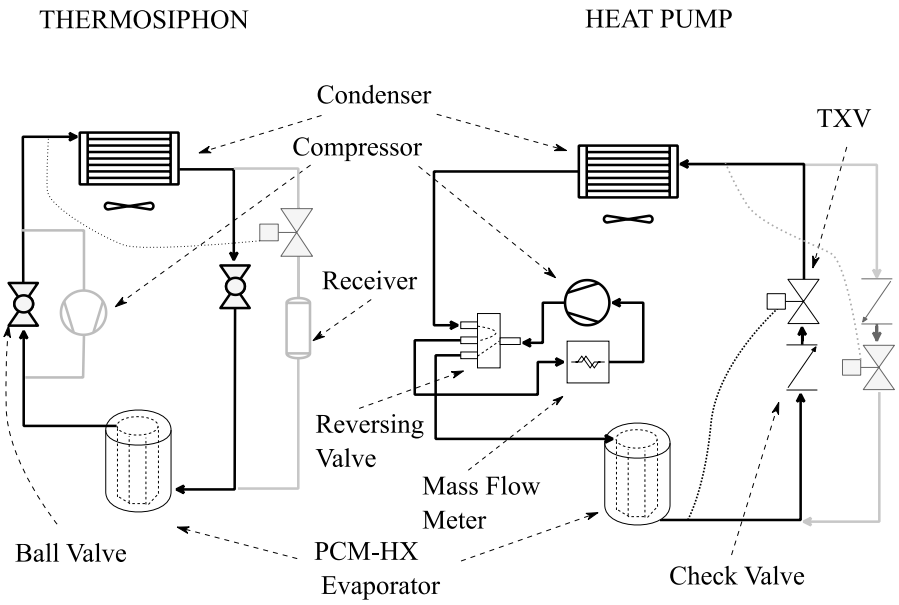

Figure 4.16: Schematic showing both thermosiphon and heat pump mode of recharge

the system is twice than those considered in the first prototype (discussed in Chapter 3) and this is achieved by increasing the weight of the PCM used in the thermal storage. The higher weight of PCM leads to addition of recharge time.

Consequently, a second mode of recharge called the heat pump mode is considered. A reversible four-way valve can be used to change the refrigerant flow direction from the compressor and recharge the PCM by operating the PCM storage as an evaporator. The compressor used in RoCo is of the variable-speed type and the recharge time may be controlled by adjusting its RPM. There are two TXV in the circuit for heat pump, each protected by a check valve. The bulbs of the TXV are connected to outlet of either the air to refrigerant heat exchanger or the PCM-HX. During the cooling operation, the outlet of air to refrigerant heat exchanger (marked as condenser in Figure 4.16) is connected to the bulb of TXV, while the outlet of PCM-HX is connected to the bulb of the second TXV. This second TXV is operational during the heat pump operation.

4.3.2 Modeling graphite enhanced PCM storage

The cross-section of the graphite enhanced PCM is shown on the left of Figure 4.17. It consists of a cylinder of diameter 10 inches and height 12 inches. Eight 0.25 inch copper tubes are inserted at a distance of 2 inch from the outer diameter, with headers connecting at bottom and the top. The symmetric location of the refrigerant tubes is exploited to allow simplification in modeling. Only a single tube may be modeled and the behavior of the entire thermal storage may be captured by scaling the behavior of this single section by eight. The PCM surrounding each refrigerant tube is in the shape of a $\frac{1}{8}$ pie. However, it is assumed to be a cylinder for modeling as shown on the right of Figure 4.17. Thermocouples located on the top and bottom surfaces of the cylindrical PCM negligible differences. Thus temperature variation along the length as well as the radius are ignored for the PCM control volume. This allows modeling of PCM as 1-D control volume. The radius of this imaginary cylinder (r_o) is taken such that the sum of the volumes of the eight cylinders equals the total volume of PCM in the experiment.

The graphite matrix present in the PCM prevents the circulation of liquid PCM by natural convection. As a result, the only mode of heat transfer for the phase change is conduction. The entire PCM behavior can be modeled without any empirical equations in this case. Finite volume method is used to model the cylindrical control volume of the PCM (Figure 4.17, right). A staggered grid is adopted with the mass and energy of the PCM assumed to be concentrated at the center (dotted lines in Figure 4.17, right), while the heat fluxes calculated the boundary (solid lines in Figure 4.17, right). The number of discretization for the control volume is 5.

The thermal conductivity of enhanced PCM is same for both solid and liquid phase,

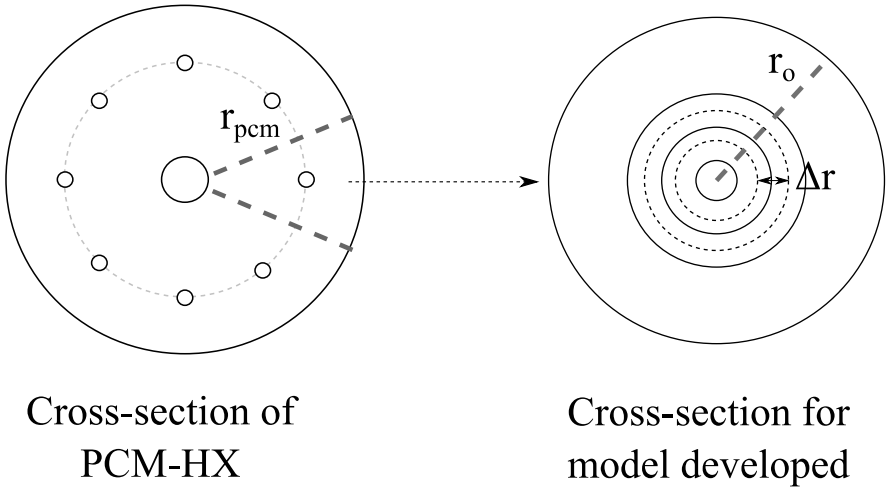

Figure 4.17: Cross section for modeling PCM

since it is primarily driven by the graphite [205]. As a result, thermal conductivity (k) is treated as a constant and not a function of melt fraction.

The staggered grid approach employed in discretization involves having mass and energy evaluations at the center of volumes while the heat flux evaluations are at the border. The heat storage is modeled using the `PCMCapacitor` (discussed in Section 3.2.2.1). The heat transfer between adjacent control volumes is evaluated using Equation (4.1). The index i = 1, for the refrigerant tube outer diameter and for discretization of 5, the outer diameter of PCM cylinder control volume gets i = 6. The solid lines at the border of control volume get integer indices 2,3,4 and 5, while the dotted lines at center have index of 1.5, 2.5, 3.5, 4.5 and 5.5. The thermal conductance between the refrigerant tube and first control volume is evaluated by Equation (4.2).

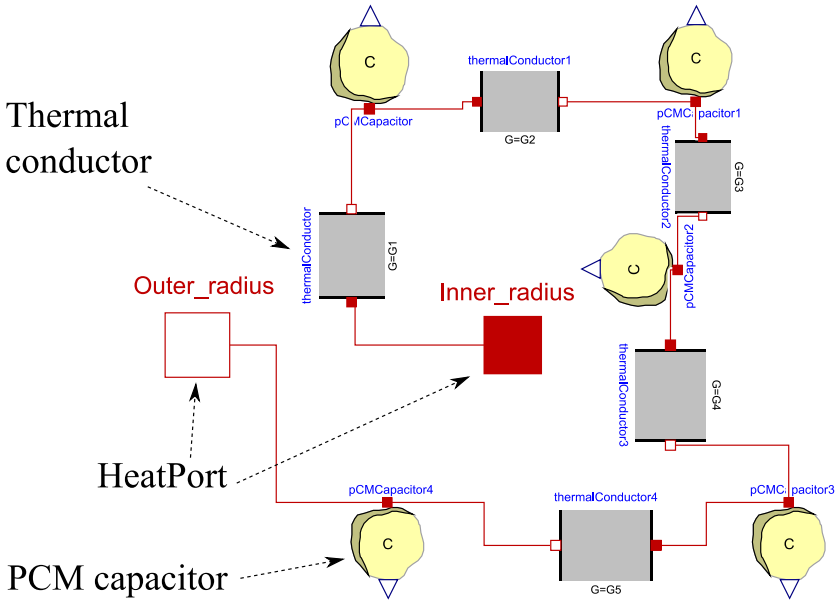

Figure 4.18: Model diagram for discretized PCM control volume

$$G_i = \frac{2\pi r_i L_t k}{\Delta r} \tag{4.1}$$

$$G_1 = \frac{2\pi \left(\frac{r_1 + r_{1.5}}{2}\right) L_t k}{\frac{\Delta r}{2}} \tag{4.2}$$

The discretized model of PCM is implemented in Modelica. The model diagram for it is shown in Figure 4.18. It consists of alternating grid of `PCM capacitor` and `ThermalConductor` components. The thermal conductance evaluated from Equation (4.1) and Equation (4.2) is given as a parameter input to the thermal conductor. The model has two `HeatPorts` at inner radius and outer radius of the cylinder, which enables heat transfer connections with refrigerant control volume and heat losses to ambient respectively.

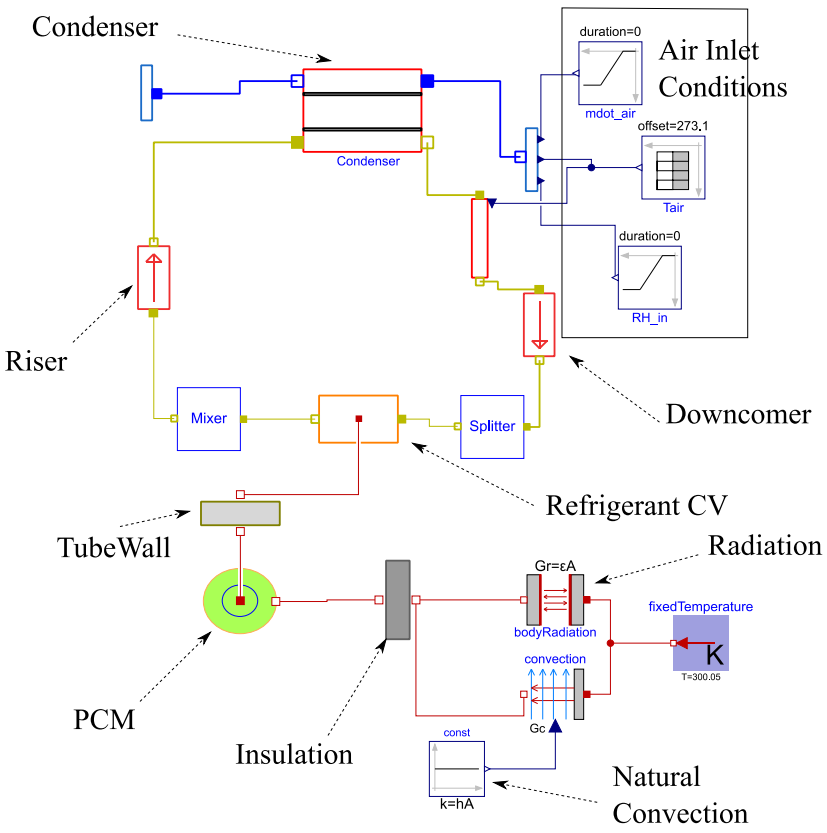

Figure 4.19: Model diagram for thermosiphon

4.3.3 Validation of graphite enhanced PCM model

The combination of all these components is then wrapped up as a component with a model diagram for easy visualization in system simulation. This PCM model is used in thermosiphon system model (Chapter 3) for validation (see Figure 4.19). The details are skipped here for brevity.

The PCM is enclosed by insulation foam wrapped with tin foil. The heat losses by natural convection are estimated using Churchill correlation [202], and an emissivity of 0.04 is used to model heat losses by radiation through the tin foil. Properties of Buna-

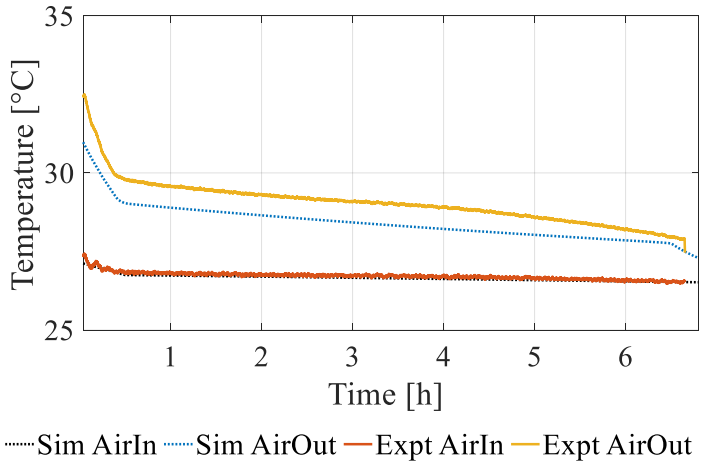

Figure 4.20: Comparison of airside temperature across condenser

N rubber (density = 72 $\mathrm{kg\,m^{-3}}$, thermal conductivity = 0.25 $\mathrm{W\,m^{-1}\,K^{-1}}$, specific heat capacity = 1350 $\mathrm{J\,kg^{-1}\,K^{-1}}$) are used to evaluate the thermal resistance offered by the insulation foam. Insulation foam is modeled as a circular pipe wall with capacitance. The heat transfer is assumed to be 1-D along the radial direction. The properties of CENG are given in Table 3.3 with volume fraction 6.3%.

The airside outlet temperature (see Figure 4.20) from condenser has two different slopes, the steeper one for the heat release during the sensible cooling of liquid PCM, which is initialized at 50°C. The temperature glide is given as 6°C. This is obtained by model calibration.

The DSC profile of PureTemp 37, which is enhanced for the current application can be seen in Mallow et al. (2018) [211] and shows similar glide. However, the specific heat capacity is not evenly distributed as a function of time for the real case and is modeled by the temperature transforming model.

The refrigerant pressure in the PCM-HX evaporator shows a good match with ex-

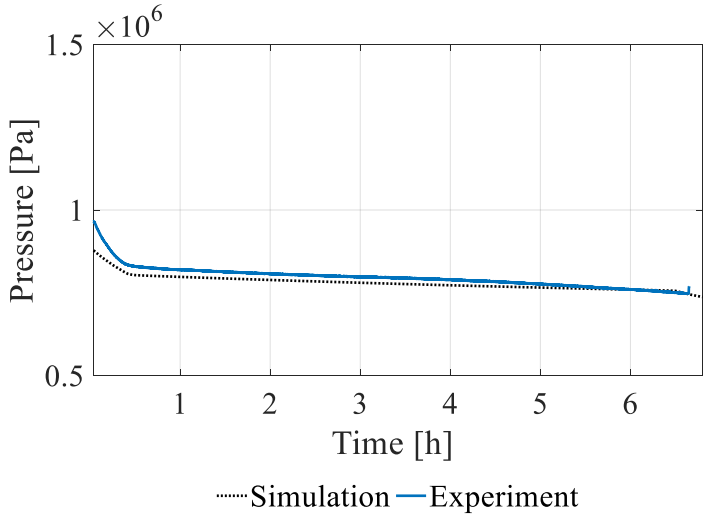

Figure 4.21: Refrigerant pressure inside PCM-HX

periment data (see Figure 4.21). The pressure gradient generated by gravity is used for circulation of refrigerant in the thermosiphon. These gradients are small and refrigerant pressures at all locations in the circuit have similar values.

The thermocouples are located at inlet and outlet of PCM-HX evaporator and are compared with the temperature inside the refrigerant control volume (See Figure 4.22). The model is able to predict the temperatures fairly accurately.

Finally, thermocouples are located on the top and bottom faces of the PCM storage. Average value of all these readings is plotted versus the value of the PCM temperature obtained from the model. The model matches the trends qualitatively (Figure 4.23). The temperatures are slightly higher for the simulation as it represents averaged temperature over the entire length of the cylinder as compared to the top face where the thermocouples are located. Heat losses by convection and radiation from the surface may result in slightly lower measured temperature.

The total recharge time by thermosiphon operation for PCM starting at 50°C to

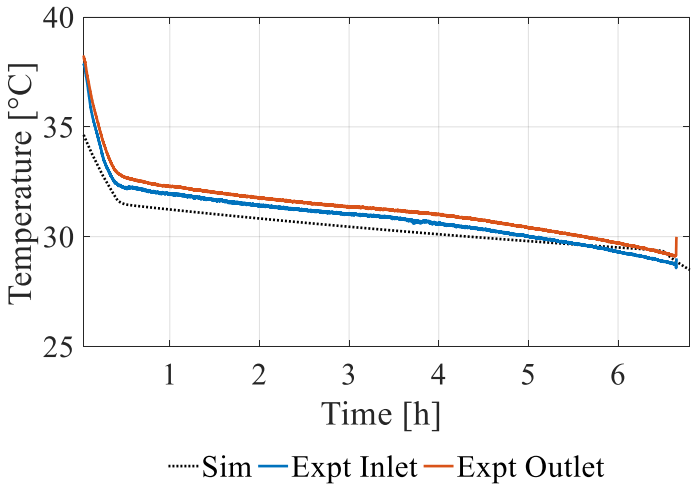

Figure 4.22: Refrigerant temperature inside PCM-HX

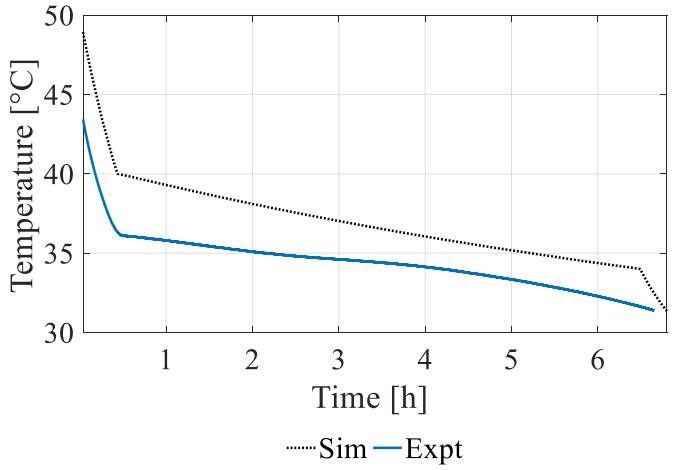

Figure 4.23: Temperature of PCM

the point of complete solidification is 390 minutes. Time taken by sensible portion of the recharge (liquid at 50°C to 40°C) is 28 minutes. Fan running at 7 W is used for the entire operation. The energy required for the recharge = 45 W-hr.

4.3.4 Heat Pump based recharge

The total recharge time for thermosiphon is 6 hours even after enhancing the heat transfer of PCM with graphite for a 4-hour cooling operation. Ideally, RoCo should be able to operate the entire length of a typical office day of 8 hours. It may be desirable to operate a heat pump cycle and use the compressor for a faster recharge of PCM. The dynamic behavior of the heat pump operation is investigated by simulation. The compressor used is of variable speed type and a parametric study of its RPM is conducted to extent of trade-offs involved.

The model diagram for simulation of heat pump operation is shown in Figure 4.24. The PCM model from Figure 4.18 is used in the simulation. Other components like compressor, thermal expansion valve (TXV), refrigerant tube and condenser are discussed in Qiao et al.(2015) [165]. The pressure and temperature at the outlet of PCM-HX evaporator are given as input to the TXV model. The compressor efficiencies and valve parameters are available from model calibration with cooling operation experiment data (see Section 4.2.2). The compressor RPM is varied and simulations are conducted at RPM values of 2100, 2600, 3100 and 3600.

The melt fraction and compressor power consumption during the recharge operation at four different compressor RPM is shown in Figure 4.25 and Figure 4.26. It can be observed that higher RPM leads to faster recharge, but the power consumption by the compressor to deliver the high RPM is large. Since the time duration of recharge is

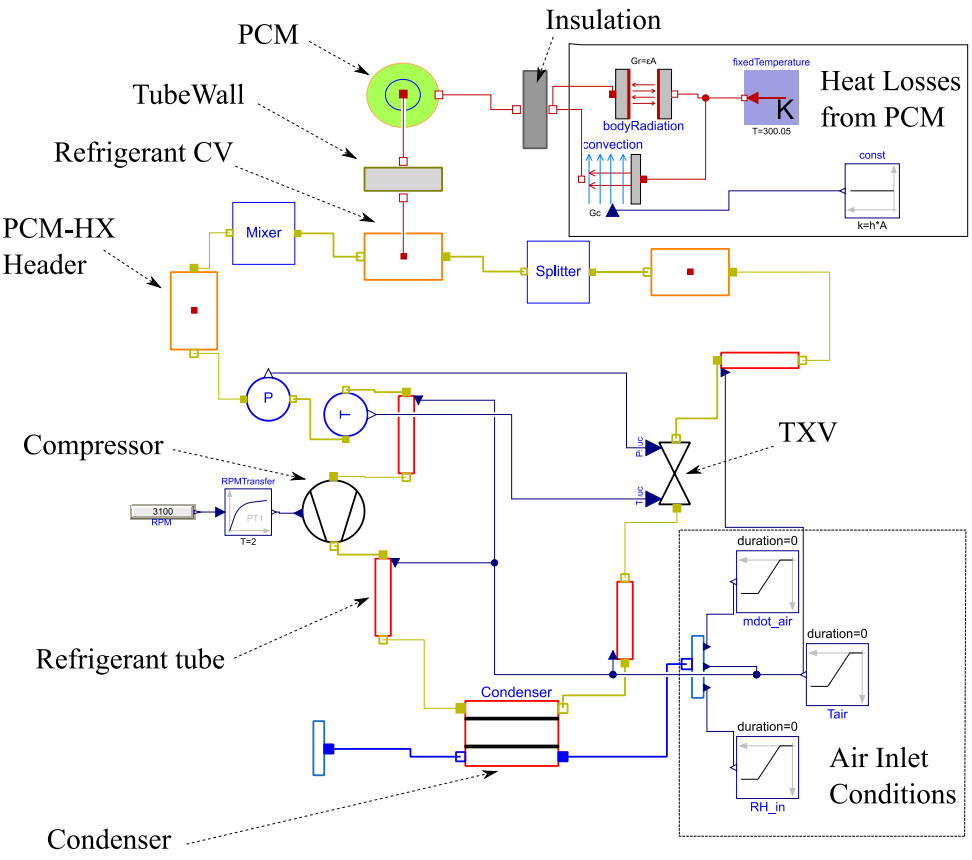

Figure 4.24: Model diagram for heat pump recharge

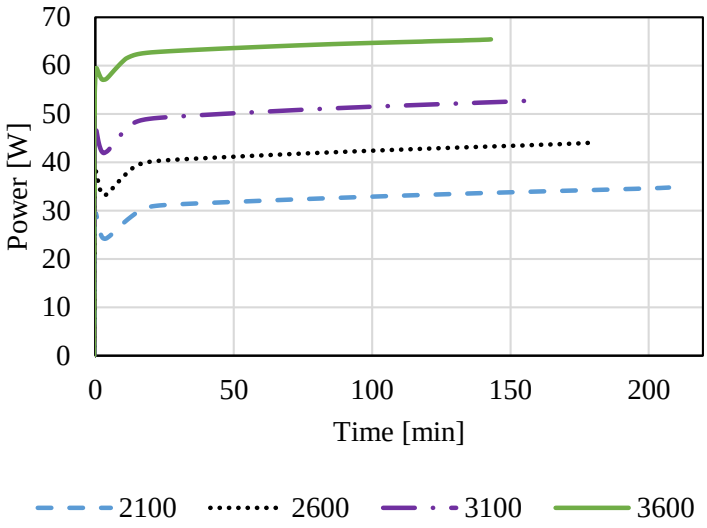

Figure 4.25: Power consumption of PCM at different RPM with heat pump recharge

different, it is necessary to compare integrated power consumption during the recharge time duration.

A fan is also operational during the entire recharge cycle and so a 7-W power usage needs to be added to the power consumed by the compressor. These values are plotted in Figure 4.27. The increase in energy consumption for the entire recharge operation is increased by 3-4 times that of the thermosiphon.

From experiment data, the coefficient of performance (COP) for just the vapor compression cycle is obtained to be 4.25, with 754.0 W-hr of cooling delivered at energy consumption of 177.4 W-hr. For a complete cycle COP, the energy consumption of recharge cycle also needs to be added to the energy consumption during cooling operation. The energy additions for thermosiphon = 45 W-hr, while for heat pump recharge is shown in Figure 4.28. We can observe 35-55% reduction in recharge time duration in comparison with the thermosiphon operation from the heat pump operation. The COP for complete cooling and recharge operation decreases by 30-35% on switching from thermosiphon to

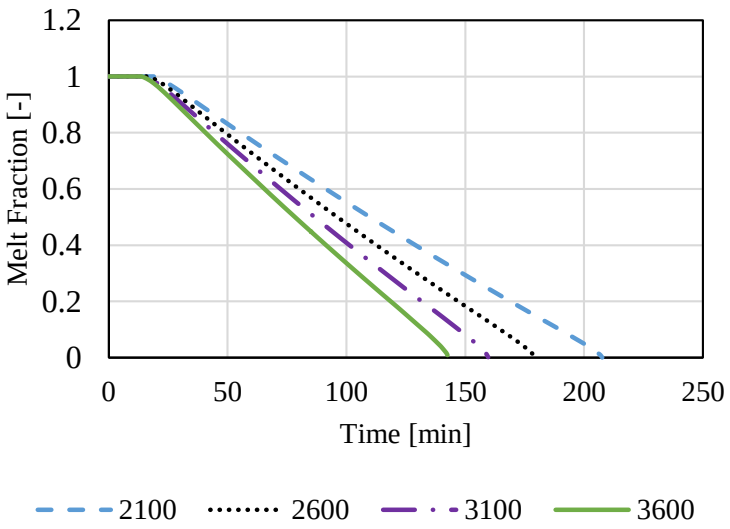

Figure 4.26: Melt fraction of PCM at different RPM with heat pump recharge

heat pump operation.

RoCo enables elevation of set-point temperatures of buildings without compromising occupant thermal comfort and can provide savings in the range of 10-30% on the building air conditioner. The building air conditioners typically consume power in the range of kW-hr. Faster recharge from heat pump operation will provide longer cooling operation of RoCo and consequently higher energy saving on the building air conditioner. Thus, heat pump recharge shows promise in comparison to the thermosiphon and will be used in future prototypes.

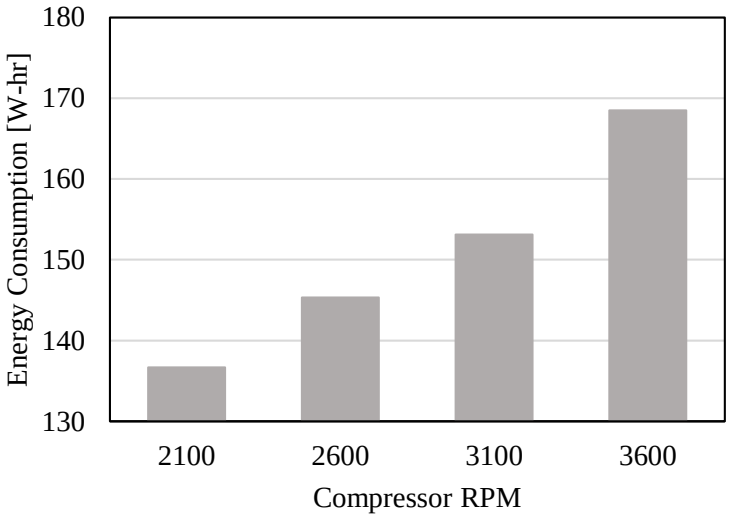

Figure 4.27: Recharge performance by heat pump operation at different compressor RPM

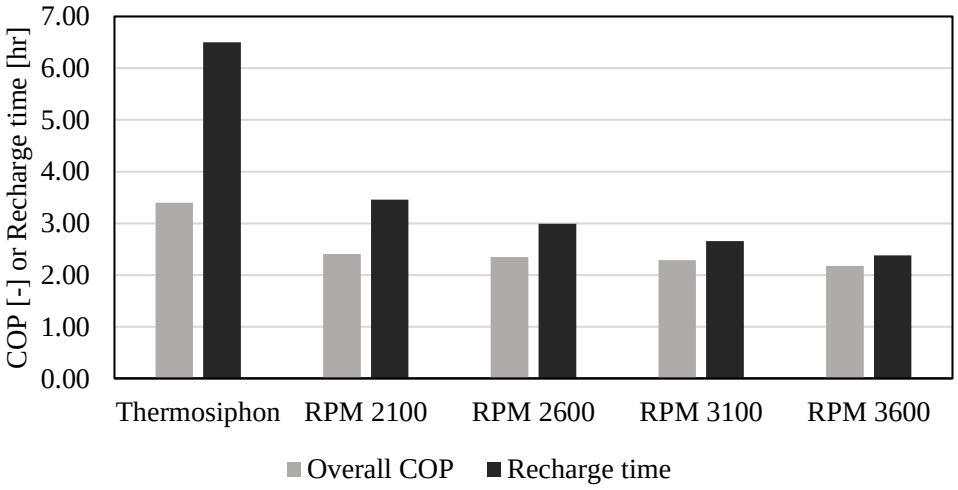

Figure 4.28: Comparison of various recharge options for RoCo

Chapter 5: Cyclic Losses in Vapor Compression System

5.1 Introduction

Previous chapters describe development of personal conditioning systems which have the potential to reduce 10-30% of energy consumption by building HVAC. Further reduction in energy consumption can be achieved by improving the performance of the building HVAC itself. Typically, building HVAC consists of a vapor compression system, which operates cyclically. This cyclic behavior leads to losses in performance, which will be the focus of the present chapter. A dynamic model of a conventional split-type air conditioner is developed and validated with experiment data. Special attention is given to the refrigerant migration occurring during the cyclic operation. The ANSI/AHRI Standard 210/240-2008 [32] specifies a cyclic D-Test, which is carried out with the air conditioner for validation.

5.2 Modeling Vapor Compression System

The model diagram for the system simulation is shown in Figure 5.1. The basic control volume equations are obtained from the `CEEE Modelica Library` developed by Qiao (2014) [47]. To enable stable simulation for reversible and zero flows which are expected during the cyclic operation, the components are updated to the `Stream Connector` on

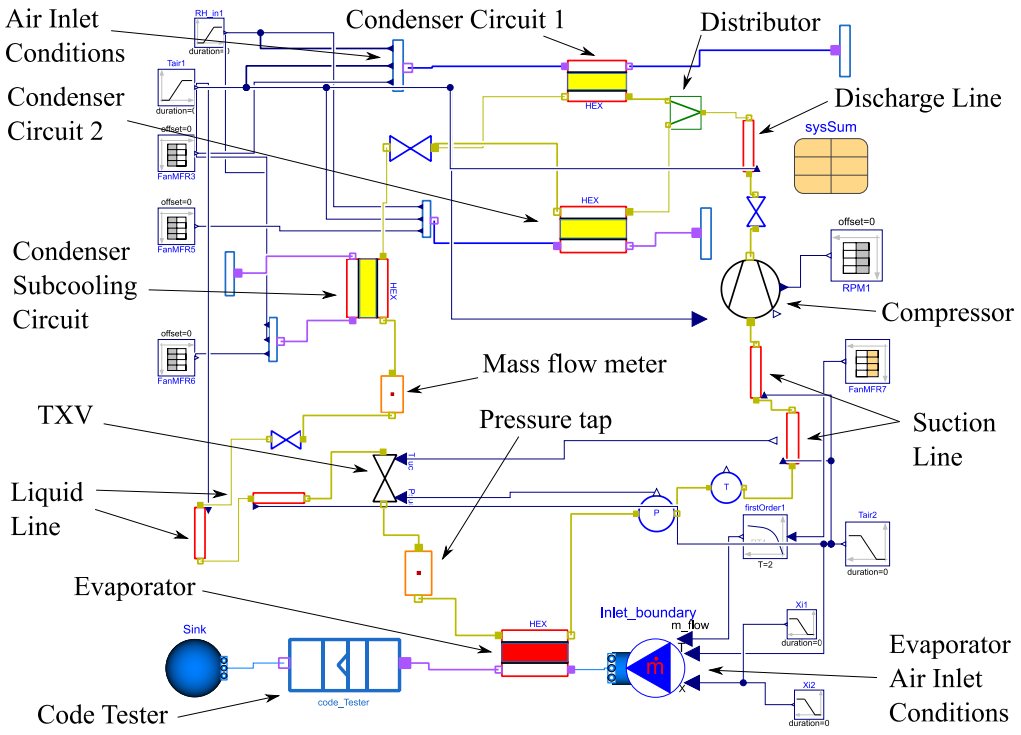

Figure 5.1: Model diagram for cyclic D-Test of air conditioner in a Code Tester

both airside and refrigerant side. A brief description of the components and the input parameters used for simulation are presented here.

5.2.1 Heat Exchangers

Condenser and evaporator are the heat exchangers in the vapor compression system. Both of them are modeled with separate control volumes for airside, tube and refrigerant as shown in Figure 1.4.

The evaporator consists of 3 refrigerant circuits (see Table 5.1 for other geometry details) in the form of a "N"-shaped coil. For the purpose of modeling, since each of the circuit is identical, only a single circuit is modeled and its behavior is scaled to simulate the overall performance of the heat exchanger. The condenser consists of three circuits,

two with identical number of tubes and a third circuit with a different number of tubes (see Table 5.2). Only one of the identical circuits is modeled and its performance parameters are scaled by two to model the identical circuits. For the third circuit, a separate heat exchanger model is used. The airside mass flow rate is distributed in the ratio of the number of tubes in each circuit. A distributor model is used to divide the refrigerant flow into these components as per their flow resistances. Finally, the refrigerant from these three circuits, flows through a sub-cooling circuit, which is modeled by a separate component. The detailed accounting of internal volume of the heat exchanger is required to capture the refrigerant migration accurately. Geometry details of them are found in Table 5.1 and 5.2.

Table 5.1: Evaporator geometry parameters

Parameter	Unit	Value
Tubes Per Row (Normal to Air Flow)	-	36
Number Tube Rows (In the direction of Air Flow)	-	2
Number of refrigerant circuits	-	3
Total number of tubes	-	72
Number of tubes per circuit	-	24
Tube Length	m	0.408
Tube Inner Diameter	m	0.0083566
Tube Outer Diameter	m	0.0100076
Fins per inch (FPI)	in^{-1}	16
Tube Material	-	Aluminum
Fin Material	-	Aluminum

Table 5.2: Condenser geometry parameters

Parameter	Unit	Value
Tubes Per Row (Normal to Air Flow)	-	24
Number Tube Rows (In the direction of Air Flow)	-	1
Number of refrigerant circuits	-	4
Total number of tubes	-	24
Number of tubes per circuit	-	8,6,6,4
Tube Length	m	1.7628
Tube Inner Diameter	m	0.0064008
Tube Outer Diameter	m	0.007366
Fins per inch (FPI)	in^{-1}	25
Tube Material	-	Copper
Fin Material	-	Aluminum

5.2.1.1 Refrigerant Control Volume

A flow chart representing the calculations for the refrigerant side are shown in Figure 5.2. Pressure and density weighted enthalpy are used as state variables. Void fraction based enthalpy correction is implemented to differentiate flow enthalpy from static enthalpy. Details of the calculations are presented in Laughman et al. (2015) [56]. Finally, using state transformations (partial derivatives of density with respect to the state variables), the transient mass and energy storage terms are converted to partial derivatives of state variables. These derivatives are used to calculate the values of the state variables at the next time step. The process continues until the stop time of dynamic simulation is reached.

Prediction of refrigerant charge in various portions of heat exchanger is best predicted by the Rouhani Axelsson correlation [218] with Steiner modification [219] as per the observations from optical void fraction measurement by Wojtan et al. (2004) [220]. However, it is a drift-flux based model, depending of refrigerant mass flow rate. At zero flow conditions, the model may produce division-by-zero errors. Slip-flow based void fraction models are also plotted at the flow conditions, alongside homogeneous and Rouhani-Axelsson with Steiner modification as shown in Figure 5.3. It can be observed that homogeneous void fraction model over-predicts void fraction significantly. Smith [221] and Chisholm [222] correlations provide similar results as the Rouhani-Axelsson correlation. Zivi correlation [223] has small under-prediction in regions of small flow quality, but it involves much less thermo-physical property evaluations. This leads to a faster computation time and is preferred for the present investigation.

Simulating vapor compression cycles at or near zero flow is challenging, due to the

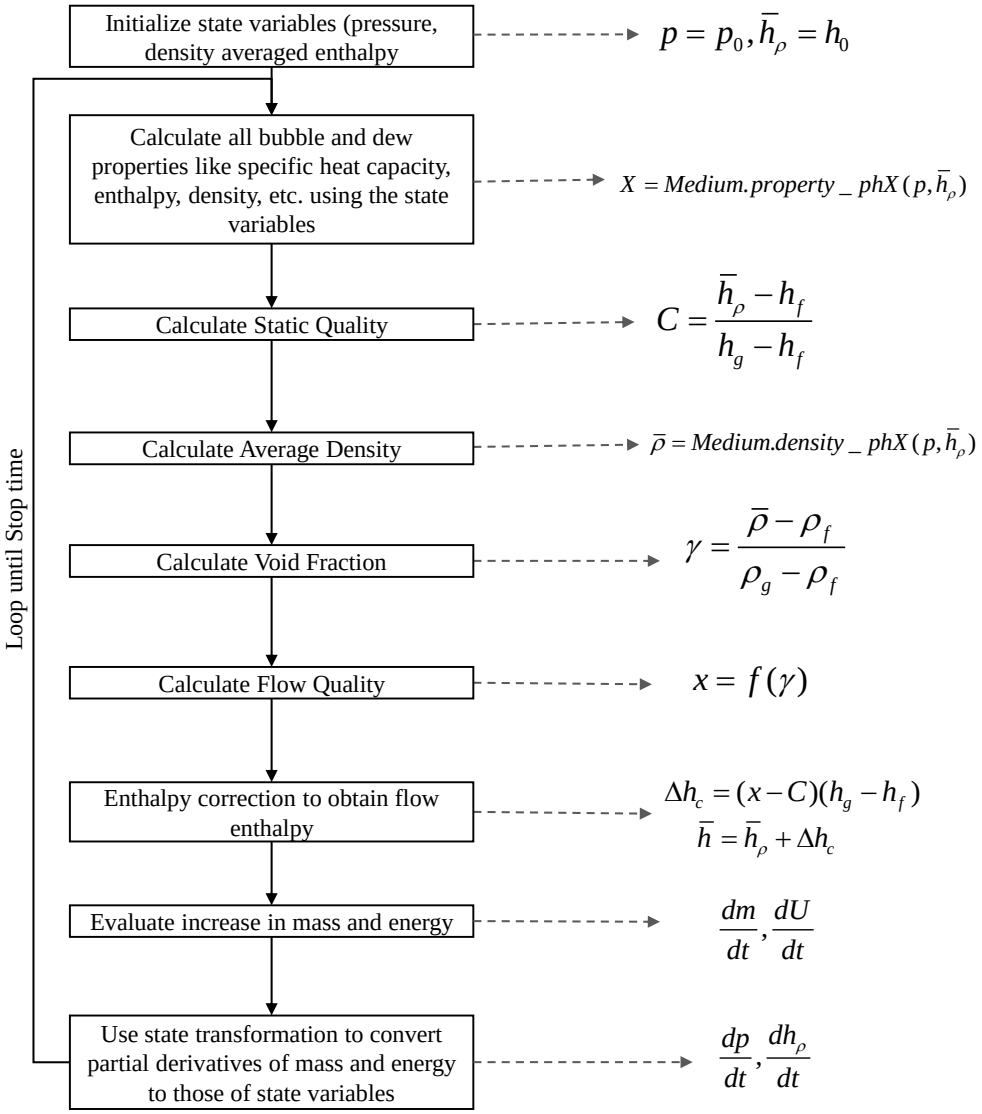

Figure 5.2: Calculations inside refrigerant control volume of heat exchangers

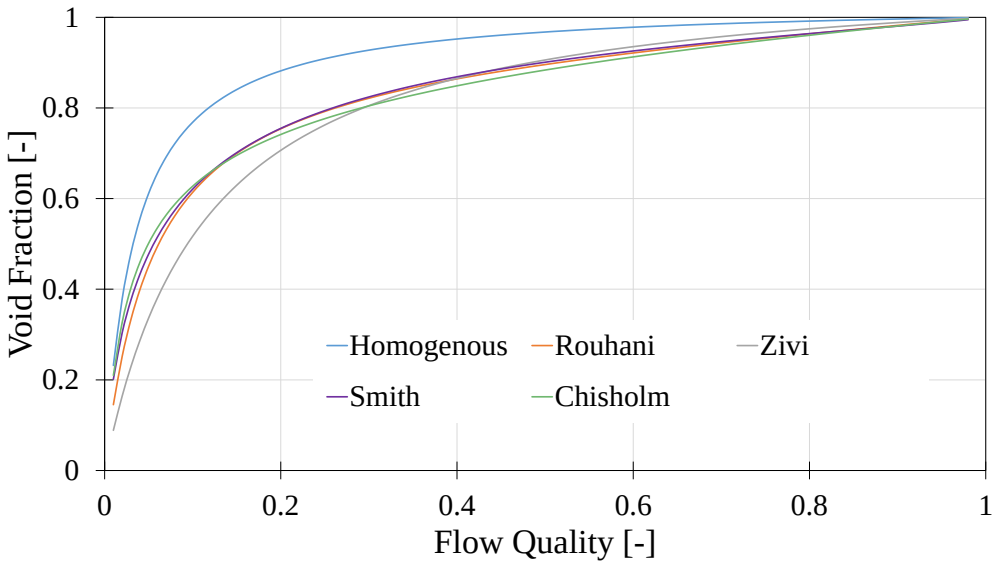

Figure 5.3: Void fraction from various correlations at flow conditions of system under investigation

fast dynamics in the model under those conditions that drastically reduce the step size of the solver. The improvements suggested by Dermont et al. [224] are implemented to increase simulation robustness under or near zero flow conditions.

The first modification is in the pressure drop correlation, which presents in essence the relationship between pressure drop and mass flow. The relationship is approximately a quadratic function (See Figure 5.4). The derivative of this function approaches zero when approaching a zero mass flow. A very small change in pressure drop corresponds to a very large change in mass flow rate, causing the solver to jump between different solutions which are beyond solver tolerance [224]. To avoid this behavior, the pressure drop correlation is modified at very low mass flow rates as shown in Figure 5.4.

Secondly, large oscillations occur due to large differences in heat transfer coefficient of adjacent control volumes during zero flow situations. As per suggestions of Dermont et al. [224], at low mass flow rates the two phase flow heat transfer

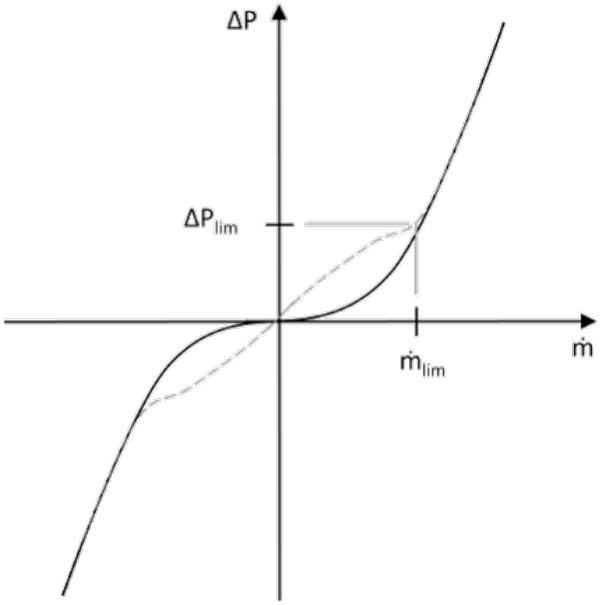

Figure 5.4: Pressure Drop Regularization [224]

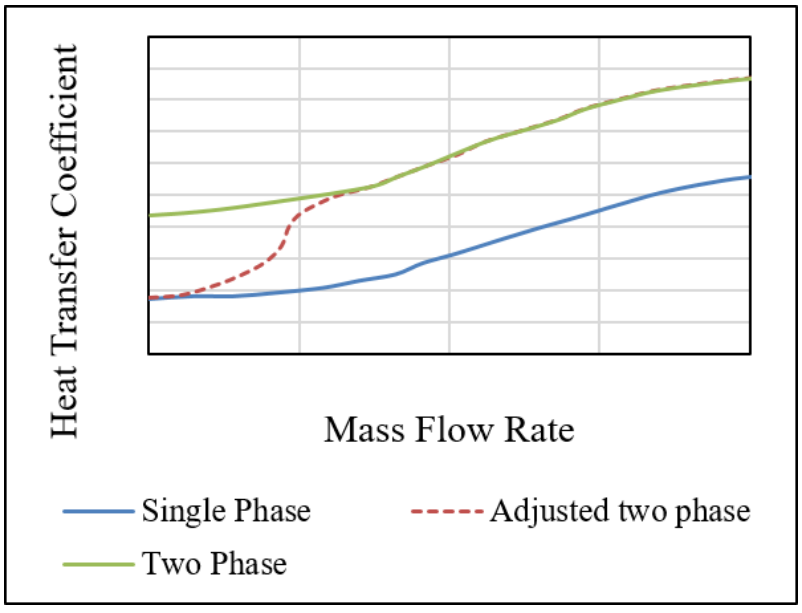

Figure 5.5: Interpolation of heat transfer coefficient between phases

coefficients should converge to single phase heat transfer coefficients. This prevents discontinuities in heat transfer and consequently energy balance of control volumes from numerical oscillations. The resultant behavior of the heat transfer coefficient correlation is shown in Figure 5.5.

5.2.1.2 Air side Control Volume

The surface area of fins and airside heat transfer coefficient are available from proprietary sources and used for improved accuracy. However, for the purposes of simulating a generic heat exchanger, these quantities can be estimated using well established geometry formulae for different fin types and airside heat transfer correlations. Calculations details for these are explained in Qiao (2014) [47]. The air side control volume is assumed to be quasi-steady due to the low density and specific heat capacity of the air. The airside sensible cooling capacity is evaluated using Equation (5.1) when the fan is on.

$$\dot{Q}_{sen,o} = \dot{m_{air}} c_{p,air} \left(T_w - T_{air}\right) \left(1 - e^{-\frac{\alpha A_{eff}}{\dot{m_{air}} c_{p,air}}}\right) \tag{5.1}$$

When the fan is off, the airflow rate may drop to zero. The airflow is occurs due to natural convection based flows. Equation (5.1) is not applicable here. Instead Equation (5.2) is used.

$$\dot{Q}_{sen,off} = \alpha A_{eff} \left(T_w - \frac{T_{air,in} - T_{air,out}}{2}\right) \tag{5.2}$$

Spline interpolation is used to combine Equation (5.1) and Equation (5.2) using the utility `Modelica.Media.Air.MoistAir.Utilities.spliceFunction`.

The airside heat transfer coefficient α is assumed to vary linearly between the conditions of fan on condition to the fan off condition (see Equation (5.3)). Thus the airside heat transfer coefficient is a function of mass flow rate and appropriate values (α_{fc} for fan on and $\alpha_n c$ for fan off) are taken as input.

$$\alpha = \alpha_{nc} + \frac{\dot{m_{air}}}{\dot{m}_0} (\alpha_{fc} - \alpha_{nc}) \tag{5.3}$$

To improve model speed and stability, the air side calculations assume no condensation of moisture during the operation. This is a reasonable assumption for an air-conditioner undergoing C-Test and D-Test, which are dry coil tests.

5.2.1.3 Tube Walls and Fins Control Volume

Tube walls and fins are modeled with the assumption that heat conduction is regarded one dimensional along the radial direction of the circular refrigerant tube. By applying fin efficiency, the tube walls and fins are lumped together [47]. The energy equation of the tube walls and fins is shown in Equation (5.4). The refrigerant and airside heat transfers are evaluated in their respective control volumes. Start value for temperature needs to be provided as an input. The spacial discretization corresponds to the discretization in the connected refrigerant control volume.

$$(M_{tube} c_{tube} + M_{fin} c_{fin}) \frac{dT_w}{dt} = \dot{Q}_{ref} + \dot{Q}_{air} \tag{5.4}$$

5.2.2 Compressor

Detailed geometry based compressor model is not a viable methodology for system level simulation due to short timescale and relatively long simulation run time [225]. So only the most important dynamics contributing to heat losses are modeled (see Figure 5.6).

Lumped control volumes for refrigerant flow in both suction and discharge are modeled. `TubeWall` model is used to model the metal portion of the compressor. Motor efficiency is provided as an input parameter and the heat generated by the losses in motor is transferred to the suction control volume. Heat losses by radiation and natural convection from both top and lower shell of compressor are estimated. Conduction axial conduction along the shell is not modeled. Motor is also assumed to transfer heat entirely to the suction control volume and thus, heat losses from motor to ambient are neglected. The refrigerant side heat transfer coefficient inside compression can be evaluated using Dittus-Boelter correlation [215] as per suggestion by Bell et al.(2008) [226].

The refrigerant flow through the compressor as a function of its RPM is calculated using Equation (5.5). During the off-cycle of the compressor, there may be a leakage of refrigerant from the high-side to the low-side. At low mass flow rates, this flow is expected to be laminar. A linear leakage model is implemented to be correctly able to predict refrigerant migration through compressor during the off cycle using nominal values of refrigerant flow for a nominal pressure drop (Equation 5.6). The total refrigerant flow through the compressor is evaluated using Equation (5.7).

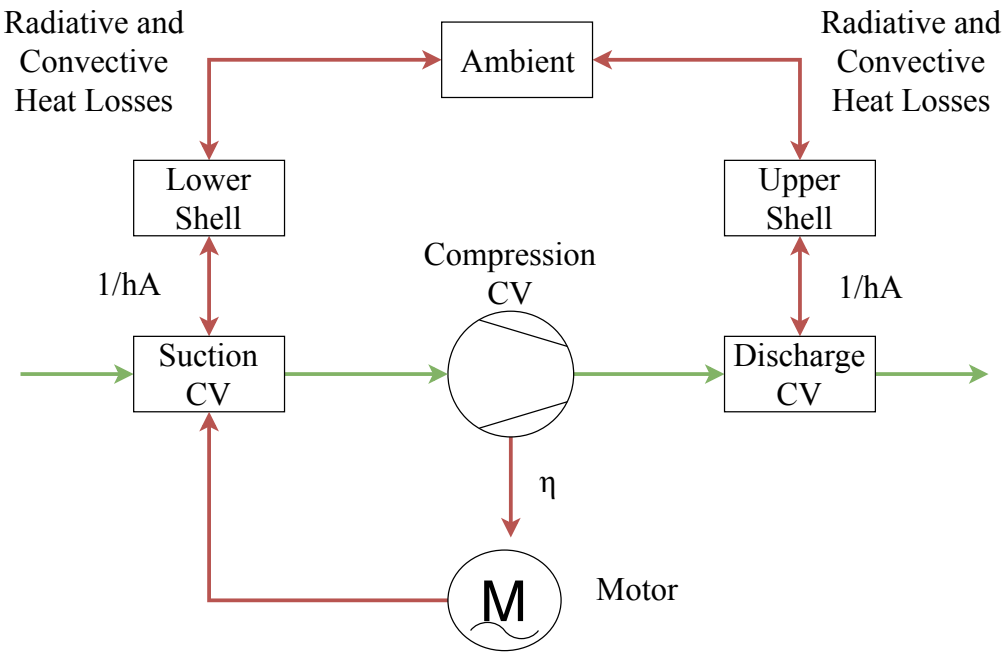

Figure 5.6: Schematic of heat transfer interactions in compressor model

$$\dot{m}_{flow} = \eta_v V_{dis} \rho \frac{RPM}{60} \tag{5.5}$$

$$\dot{m}_{leak} = \frac{\dot{m}_{leak,0}}{\Delta p_{leak,0}} (p_{dis} - p_{suc}) \tag{5.6}$$

$$\dot{m}_t = \dot{m}_{flow} - \dot{m}_{leak} \tag{5.7}$$

5.2.3 Thermostatic Expansion Valve

The TXV comprises of a throttling portion and sensor bulb portion. Physics based model of TXV similar to Qiao (2014) [47] is used for the simulation. As mentioned in Li and Braun (2008) [227], the details of the refrigerant inside the bulb are not available and typically, the fluid in the bulb is at a higher saturation pressure than the refrigerant. A tuning parameter ΔT_{sat} is used as a tuning parameter to adjust the saturation temperature of the refrigerant to that in the TXV bulb. The amount of fluid in the bulb is captured

using a time constant, which also needs to be calibrated to experiment data. A higher value of time constant (T_i) represents large amount of fluid in the TXV and vice-versa. Now, the refrigerant temperature in the bulb can be evaluated as shown in Equation (5.8). Refrigerant properties of R410A may be used to evaluate the pressure of the fluid inside the TXV bulb (Equation (5.9)). The addition of saturation temperature tuning parameter results in evaluation of higher pressure than the refrigerant pressure for the TXV bulb fluid. Refrigerant pressure from the outlet of evaporator $P_{e,o}$ is given as an input to the TXV model. The force exerted by the difference in the bulb and evaporator outlet pressure is balanced by the spring inside TXV (Equation (5.10)).

$$\frac{dT_b}{dt} = \frac{T_{suc} - T_b + \Delta T_{sat}}{t_i} \tag{5.8}$$

$$T_b = Medium.dewTemperature(p_b) \tag{5.9}$$

$$(P_b - P_{e,o})\, A_d = k\,(y + y_0) \tag{5.10}$$

$$A = \pi D_i y \tag{5.11}$$

A linear model for the spring deflection [227] is assumed due to lack of relevant information (Equation (5.11)). Finally, the equation for mass flow rate through orifice (Equation (5.12)) is used to evaluate the refrigerant mass flow rate through TXV. The only variation here from the orifice is that the flow area A is a variable depending on the force balance and geometry equations.

$$\dot{m} = C_d A \sqrt{\rho \Delta P} \tag{5.12}$$

5.2.4 Refrigerant Lines

The refrigerant lines are important from the point of view of correctly predicting the charge migration. The suction line is insulated, while the liquid line is not. Models accounting for both insulated and uninsulated refrigerant lines are modeled. The non-insulated refrigerant line is modeled with similar control volume structure as the heat exchanger (see Figure 1.4). However, the airside control volume is much simplified and models just the heat transfer to ambient by natural convection using the `Modelica.Thermal.HeatTransfer.Components.Convection` component. The airside heat transfer coefficient is estimated through Churchill-Chu correlation for natural convection from horizontal tube [228]. The insulated refrigerant line model consists of an additional `TubeWall` model described in Section 5.2.1.3 for insulated foam alongside another for refrigerant tube.

Heat transfer coefficient is given as a fixed input parameter for the models. The airside temperature for heat transfer needs to be provided as an input for these models. For the refrigerant lines, present inside the indoor unit environment chamber, the airside temperature of evaporator is given as the input temperature. Similarly, for the refrigerant lines present inside the outdoor unit environment chamber, the outdoor unit temperature is given as input. Portions of suction line and liquid line are present in both the rooms as they connect the two heat exchangers. As a result, these refrigerant lines are divided to account for accurate heat losses. The temperature at the inlet of compressor is measured by using a surface thermocouple. A small portion of the refrigerant line is uninsulated near the location of this thermocouple. As a result, this small portion is modeled using the uninsulated refrigerant line model.

5.3 Code Tester

5.3.1 Background

Code tester is described in ASHRAE Standard 41.2 [154], which provides recommended practices for airflow measurements. The test chamber is a generic name applied to these devices, but code tester has also been used for many years. The code tester (see Figure 5.7) consists of ducts for airflow passage from the test unit with pressure and temperature being measured at various locations along the passage. Flow settling devices (mixers) are placed in portions of the air duct to reduce the temperature gradient in the airflow. Nozzles alongside calibrated correlations are used to determine the volume flow rate of the air. A few dimensional constraints are applicable to their geometry. However, due to a wide variety of possibilities from these constraints, the design of code testers at different facilities are very different. There are also no guidelines on materials selected for fabricating the code testers. These aspects lead to significant variations in the thermal inertia effects for a tested unit in different code testers.

Split air conditioners (SPAC) are tested using separate environmental chambers for both indoor unit (IDU) and outdoor unit (ODU) as shown in Figure 5.7. The method used for calculating the cooling capacity is called the tunnel air enthalpy test. The code tester (labeled as airflow measuring apparatus in Figure 5.7 needs to be connected to only the IDU for the case of SPAC. A room conditioning apparatus maintains the IDU chamber to a fixed temperature, which is measured by the incoming thermocouple grid. The air flows over the IDU, where it gets cooled if the SPAC is ON. The code tester includes a mixer, an outlet thermocouple grid,

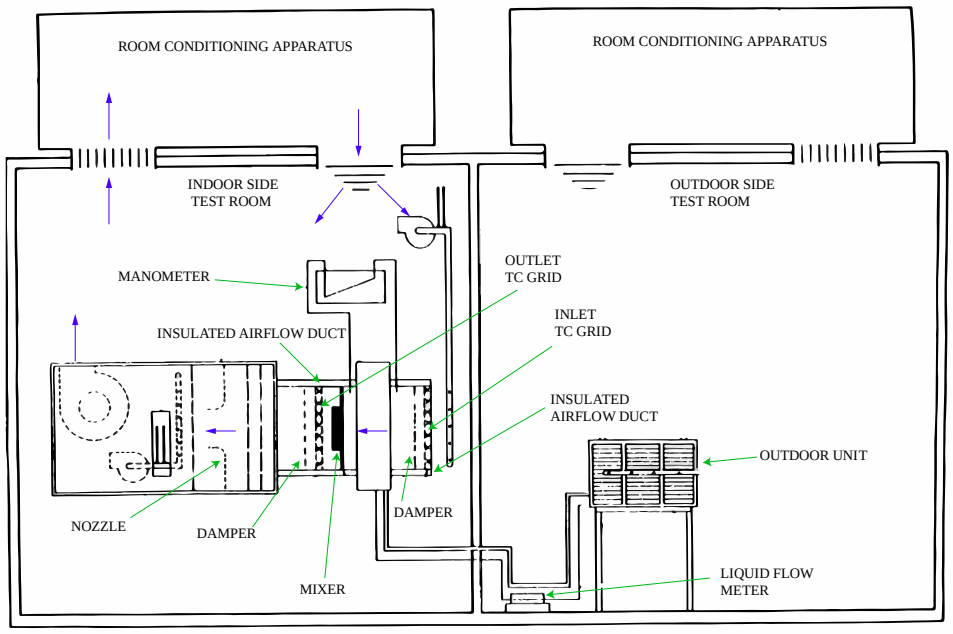

Figure 5.7: Tunnel Air Enthalpy Method Arrangement redrawn from ASHRAE Standard 116 (2010) [151]

nozzles and dampers all of which are enclosed within an insulated duct. An exhaust fan drives the air to the room conditioning apparatus to be reconditioned to the IDU chamber temperature.

Due to space constraints, the different portions of the code tester may all not be in the same horizontal plane and/or along the same horizontal axis. The insulated airflow duct shown in Figure 5.7 may consist of multiple ducts of varying lengths and bends. To avoid entrance flow effects and temperature gradients from bends, even though the whole setup ends up being fitted inside a room, the airflow length may end up being large (in the range of 20-40 feet). Such a code tester has significant thermal inertia and should be accounted for in the data reduction.

5.3.2 Model development

To correctly evaluate the outlet thermocouple grid temperature, the model for code tester is also developed and connected to the model of evaporator. The components for Code Tester are developed using the control volumes of Modelica Buildings Library [229].

The code tester used for measuring the cyclic performance of the tested unit is shown in Figure 5.8. Only a small portion of duct exists between the indoor unit and the outlet thermocouple grid to reduce the influence of code tester thermal inertia effects. An alternate proprietary code tester design, which is also used for in the current investigation consists of much longer air flow passage between the indoor unit and the outlet thermocouple grid.

This section describes the variety of components required for modeling the Code Tester. The two types of components used for modeling any generic code tester are `Duct` and `Mixer`. The object oriented nature of Modelica enables modeling any generic code tester by providing appropriate input parameters to these components. Typically, multiple duct components and a single mixer component will be required to model the complete code tester. As shown in Figure 5.8, `pipe1` and `pipe2` are the regions modeled using `Duct`. Details of the code tester shown in Figure 5.8 can be found in Qiu (2018) [230].

Figure 5.9 shows the component model for `Duct` (on Left) and `Mixer` (on Right). The `ControlVolume` and `PressureDrop` models are obtained from `Buildings.Fluid.MixingVolumes.MixingVolume` and `Buildings.Fluid.FixedResistances.PressureDrop`, respectively.

`ControlVolume` represents an instantaneously mixed volume. Potential and kinetic

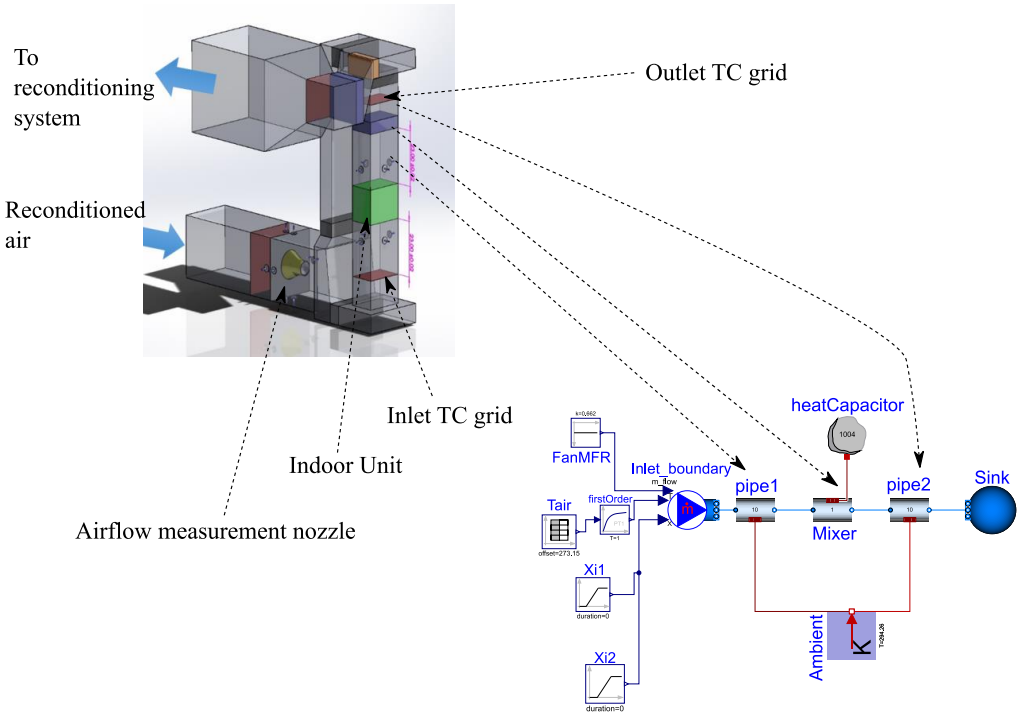

Figure 5.8: Modeling various components of code tester

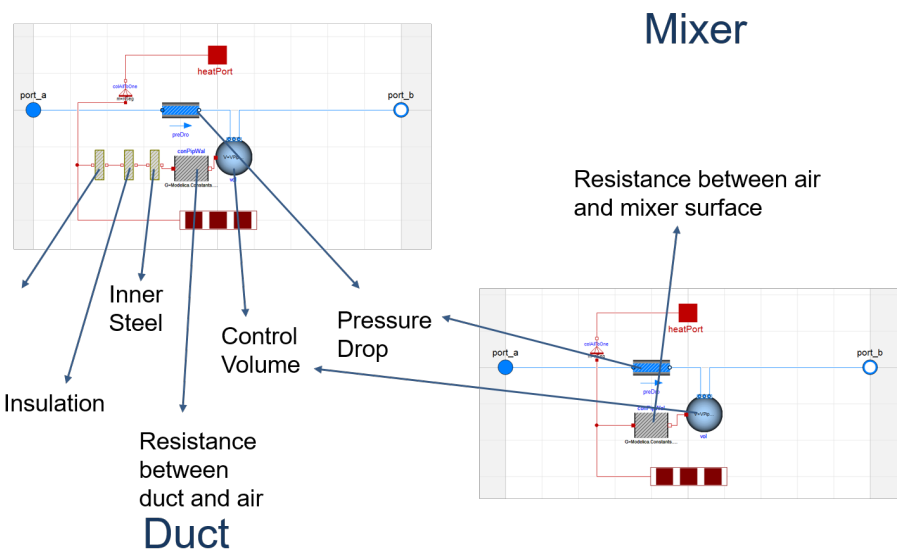

Figure 5.9: Component Model of Duct and Mixer

energy at the port are neglected, and there is no pressure drop at the ports. It can exchange heat through `HeatPort`. `PressureDrop` takes in nominal values of mass flow rate and pressure drop of the fluid as inputs and models a quadratic relationship between the two quantities.

The duct consists of two layers: an inner steel plate surrounded by insulation foam. In some cases an additional outer steel plate may be present around the insulation to form a three layer duct. Each of these three material layers are modeled using `TubeWall` (5.2.1.3). The thermal resistance between the inner steel plate and the airflow is estimated using Dittus Boelter correlation [215]. This value is given as an input to a `Modelica.Thermal.HeatTransfer.Components.ThermalConductor` component. For ducts, which may have bends an enhancement factor to the Dittus Boelter correlation is evaluated using Schmidt (1967) correlation [198].

Mixer is present entirely inside the airstream. So only the control volume and pressure drop blocks are used. The entire metal portion is lumped together using a `Modelica.Thermal.HeatTransfer.Components.HeatCapacitor` component is used to model the thermal inertia of the mixer components. The thermal resistance between air and mixer passage is provided as an input to a `Modelica.Thermal.HeatTransfer.Components.ThermalConductor` component.

5.4 Results and Discussion

The system model (Figure 5.1) is simulated with Radau II-a solver with a tolerance of 1e-6 for the cyclic D-Test [162]. To initialize surface temperatures of inner steel and foam of the code tester, a two-hour C-Test [162] is simulated with all temperatures starting at the indoor unit chamber temperature of 26.67°C (80°F).

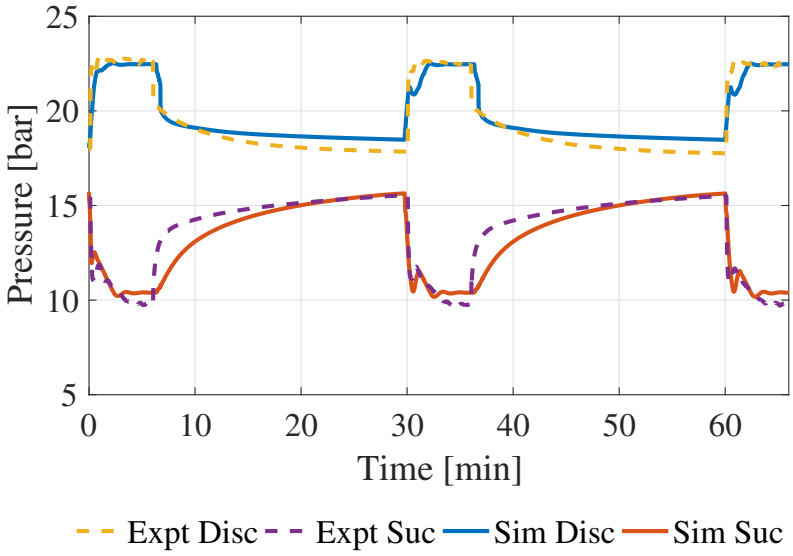

Figure 5.10: Comparison of suction and discharge pressure

The D-Test is started after a 24-minute off cycle following a 30-minute data logging period from stable values of C-Test. The test procedure does not provide time interval of running C-Test before obtaining stable readings of C-Test. This leads to different code tester initial temperatures at various locations, adding to variation in test readings. Standardization of transition from C-Test to D-Test is also another area for improvement.

5.4.1 Validation of cyclic test performance

The results are validated with experiment conducted with the code tester shown in Figure 5.8. Three on-cycles and two-off cycles are simulated. The validation of pressure levels is shown in Figure 5.10. The nominal values for refrigerant leakage through the compressor are $\dot{m}_0 = 0.0001$ kg s^{-1} and $dp_0 = 20$ bar. The minimum orifice opening of the TXV is taken to be 0 m^2. It is possible to isolate refrigerant migration through only TXV, only compressor or through both by this approach. The exact parameters will be calibrated from the experiment data.

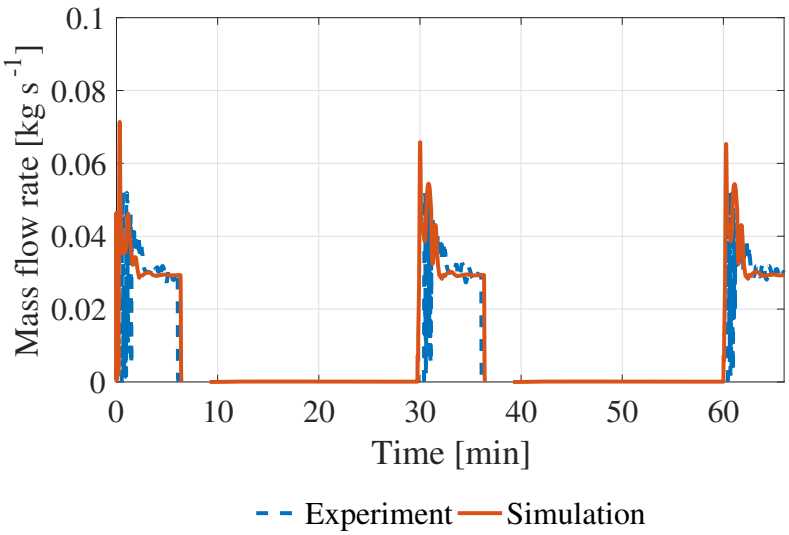

Figure 5.11: Comparison of refrigerant mass flow rate

The comparison of refrigerant mass flow rate is shown in Figure 5.11. It can be observed that this is predicted very well.

The comparison of power drawn by the compressor is shown in Figure 5.12. The rotational inertia of compressor motor at the start-up causes an overshoot at the beginning of each on-cycle. However, due to a lack of availability of compressor motor geometry, this phenomena is not modeled. The difference in integrated cooling capacity from not modeling of this phenomena is assumed negligible. The efficiency of compressor is calibrated from this plot.

The comparison of the temperature measured at the leaving thermo-couple grid is shown in Figure 5.13. The air temperature falls as the air stream gets cooled by the indoor unit during the ON-cycle for 6 minutes. Next 1.5 minutes after the ON-cycle involve the air circulating with the compressor turned off. This results in the cooling stored in the inner steel of the code tester and mixer to be partially transferred to the air stream. The cooling delivered in this portion is negligible to that from the indoor unit and so

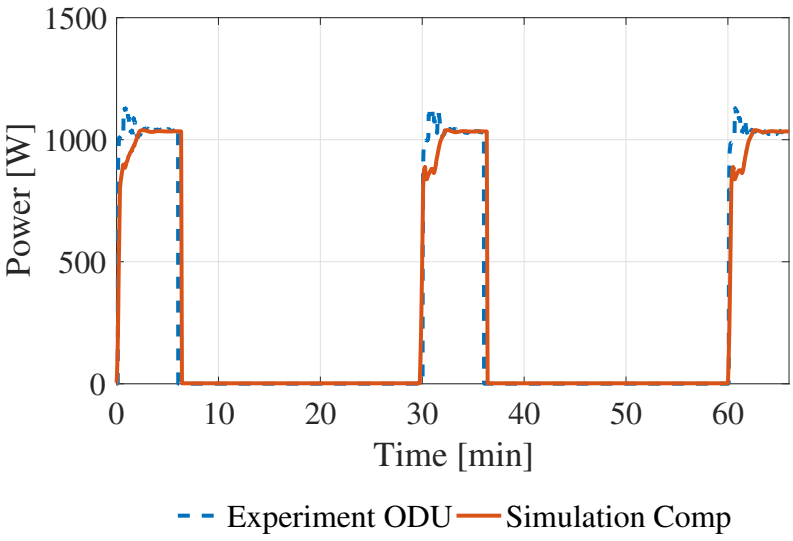

Figure 5.12: Comparison of compressor power

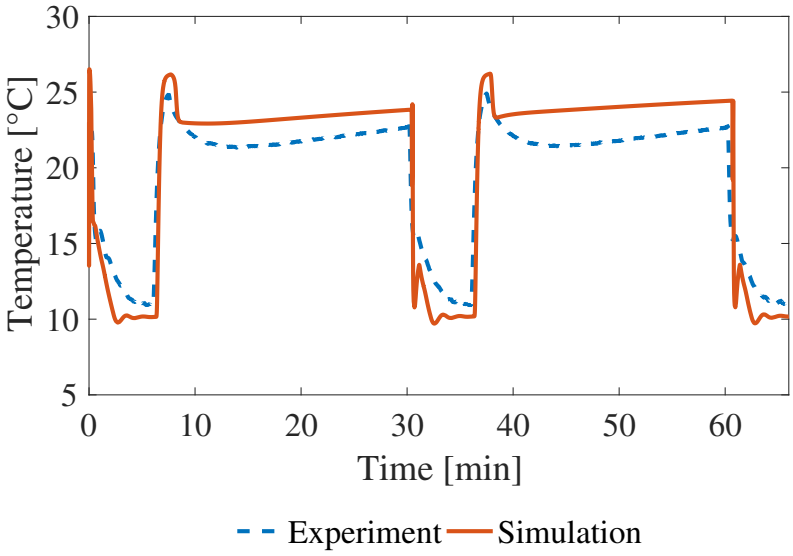

Figure 5.13: Comparison of code tester outlet thermocouple grid

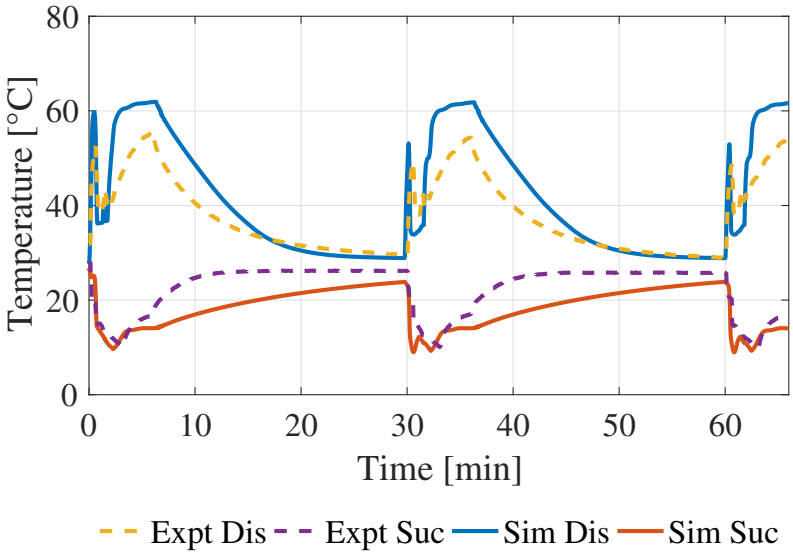

Figure 5.14: Comparison of temperatures at suction and discharge

the air stream temperature rises significantly. Finally, the next 22.5 minutes of the cycle involve dampers being shut-off to block air flow. Now, the air trapped in the code tester gets cooled down initially from the mixer and the inner steel. Later on, there is a slight increase in air temperature due to heat transfer from the IDU chamber to the air trapped inside the code tester.

The comparison of the temperature measured at the leaving thermo-couple grid is shown in Figure 5.14.

Similarly, temperatures at the outlet of condenser and inlet of evaporator are also plotted. Thus it can be seen that the model predicts the dynamic response during the cyclic D-Test with good accuracy.

5.4.2 Refrigerant Migration

Refrigerant migration plays an important role in determining the cyclic performance of the air conditioner. To evaluate refrigerant migration during the operation, quick-

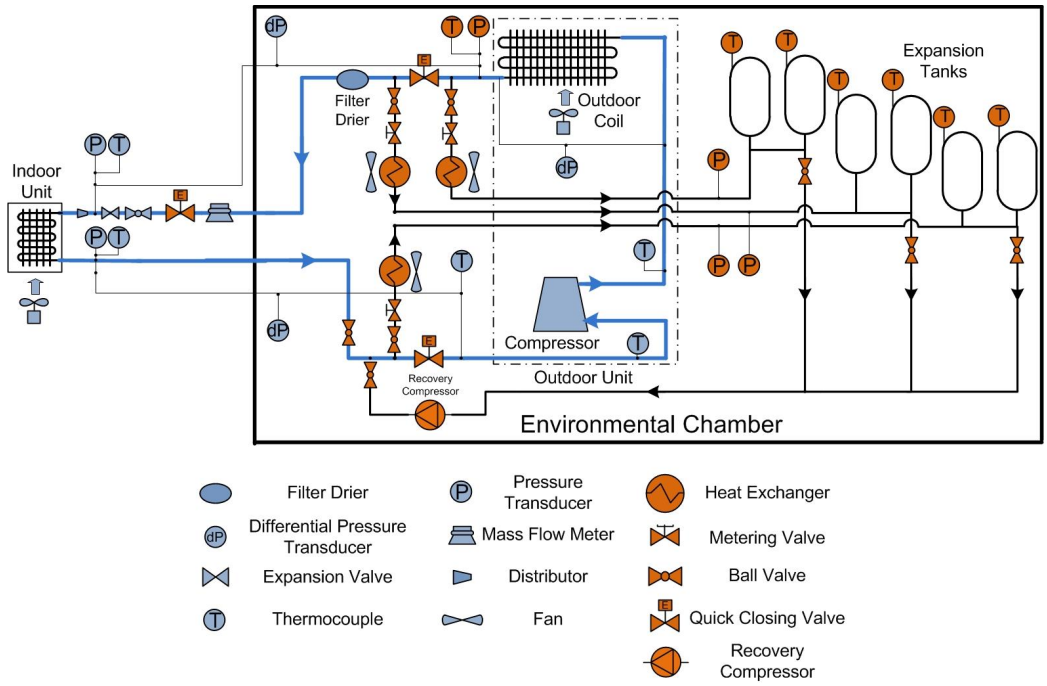

Figure 5.15: Comparison of temperatures at suction and discharge

closing valves were installed to separate the system into three locations (see Figure 5.15): (a) Indoor unit and suction line, (b) Liquid line and (c) Outdoor unit. After isolating the circuits, the refrigerant inside each of the three locations is expanded into the set of expansion tanks. The entire circuit with the expansion tanks, contains refrigerant in the vapor phase. Internal volume of each of the isolated circuits is known, and using the refrigerant pressure and temperature in each of the locations the total charge is estimated. The details of the testing procedure are explained in Qiu (2018) [230] and only briefly described here for brevity.

Refrigerant migration occurs as a result of pressure and temperature differences at various locations in refrigerant circuitry. Leakage rates through TXV and compressor provide path for refrigerant to migrate from the high pressure side to the low pressure side.

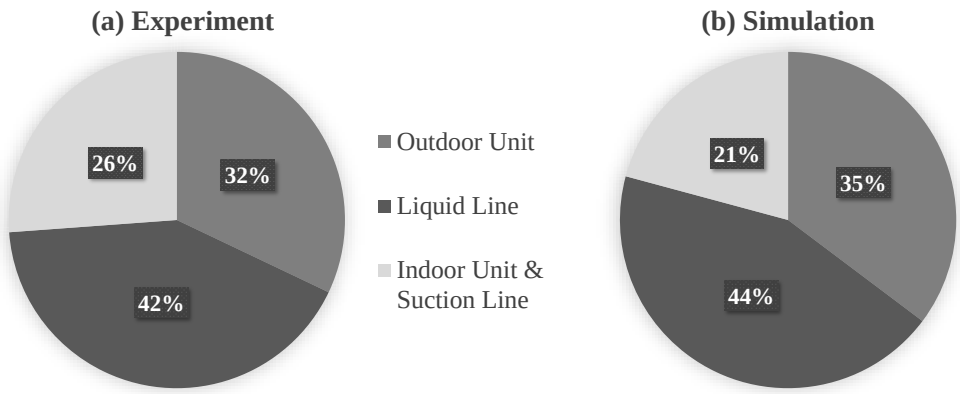

Figure 5.16: Refrigerant distribution in three locations during C-Test

These leakage rates are not available. The leakage parameters for TXV and compressor and calibrated to match experiment data.

The outdoor unit contains compressor and fan, both controlled by the same control board. When both are turned off at the same time, there is a delay between both of them coming to stop due to rotational inertia. This difference results in sharp decline of pressure for discharge pressure. The leakage flow area through TXV, leakage rate through compressor and compressor-fan delay are major factors for refrigerant migration.

The refrigerant distribution is first evaluated for the steady dry-coil C-Test. Comparison of refrigerant distribution with the simulation is shown in Figure 5.16. It can be observed that the model predicts the distribution fairly well. The higher percentage of refrigerant exists in the condenser region, which is the outdoor unit. This is because of the higher refrigerant pressure resulting in higher density of the vapor phase of refrigerant and also due to the existence of large amount of refrigerant in liquid phase. The liquid line is completely filled with liquid refrigerant and also takes up significant portion of refrigerant charge. The dryer and mass flow meter control volumes are included with the liquid line.

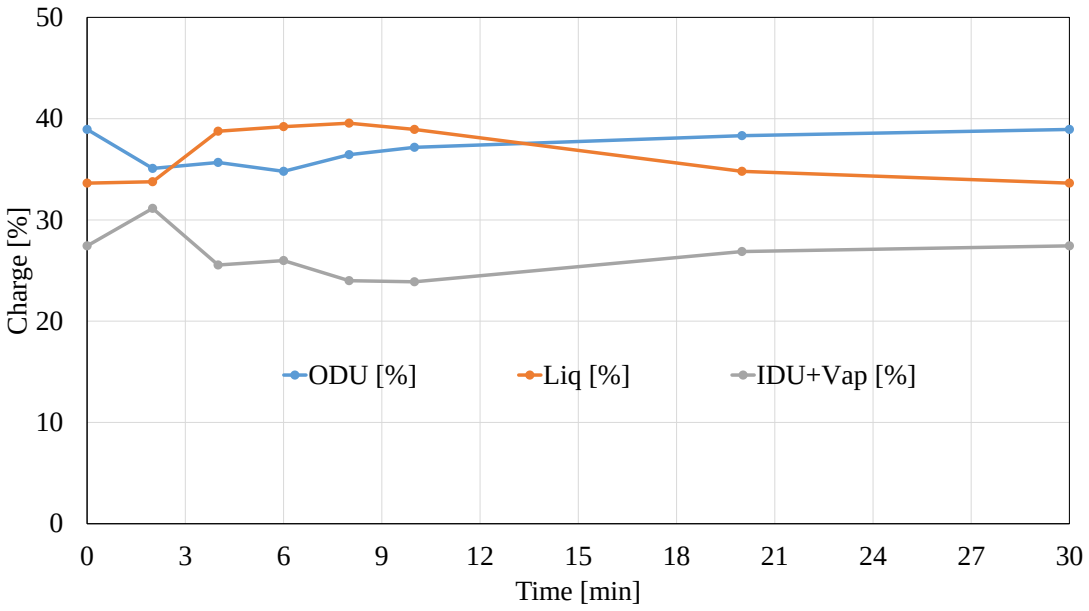

Figure 5.17: Refrigerant distribution in three locations during D-Test

The refrigerant charge stored in these three regions is measured during D-test and is shown in Figure 5.17. The experiment data is available for only 7 points and only one set of data is available at each point. Various cases are simulated to understand impact of refrigerant migration on different system parameters. The first 6 minutes consist of ON cycle, followed by 1.5 minutes of OFF cycle with dampers open and then final 22.5 minutes of OFF cycle with dampers closed.

The first case is shown in Figure 5.18. It consists of a complete shut-off TXV, refrigerant leakage through the compressor and no delay between ODU fan off and compressor off. It matches the experiment trends from Figure 5.17, fairly well. This will be referred to as case 1. The validation plots from Figure 5.10 to Figure 5.14 are for this case.

To understand the effect of delay in ODU fan switch off and the compressor off, a case with 40-sec delay between the two is simulated. This case is shown in Figure 5.19. We can observe that the fan cycling leads to a significant migration of refrigerant from

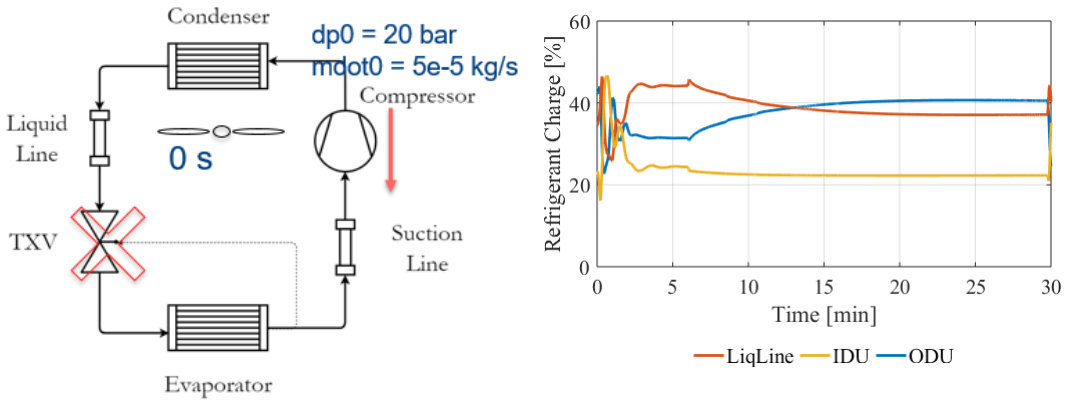

Figure 5.18: Case 01 for Refrigerant distribution in three locations during D-Test

liquid line to the outdoor unit section. This will be referred to as case 2. It shows the ability of the model to capture refrigerant migration driven by temperature differences between different portions of the circuit.

Next an opposite case of flow leakage is simulated. In this case, the compressor has a hard shut-off. The refrigerant migration path is through the TXV. Results of this case, shows significant addition of refrigerant in the evaporator. The refrigerant from the liquid line moves into the evaporator through the TXV. This situation is shown in Figure 5.20. This is referred to as case 3.

The real situation is a combination of all these cases. The fan and compressor have different rotational inertia and will have some delay to be fully off. The TXV and compressor may not have hard shut-off. There will be some leakage through them. It is necessary to understand the effects of these parameters on the measured variables.

The effect is shown on the suction and discharge pressure profiles. The delay in fan cycling causes more cooling of the refrigerant in the condenser leading to a sharp drop in

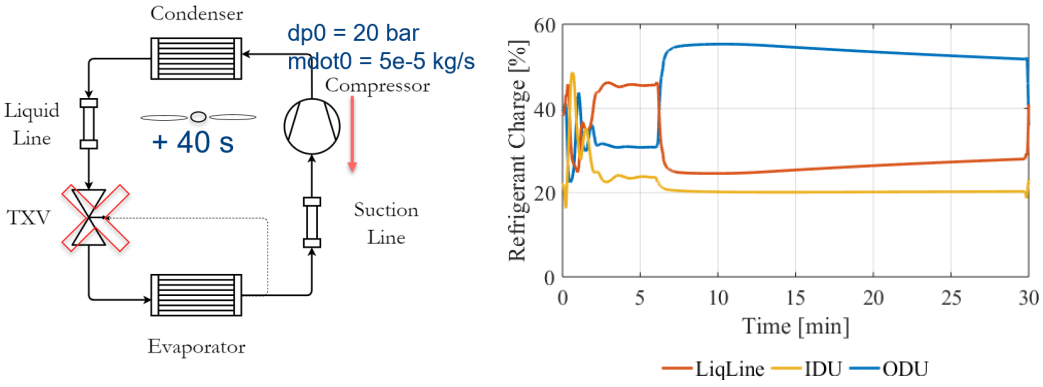

Figure 5.19: Case 02 for Refrigerant distribution in three locations during D-Test

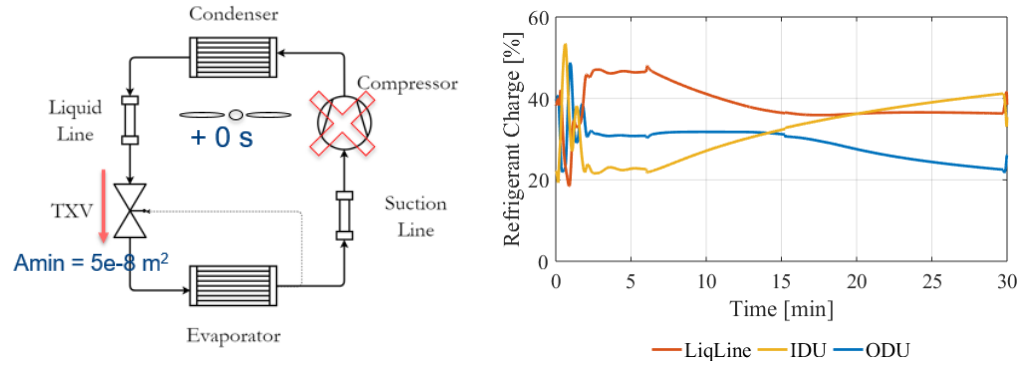

Figure 5.20: Case 03 for Refrigerant distribution in three locations during D-Test

discharge pressure. Having no delay leads to a much slower decline in discharge pressure at the onset of OFF cycle. The leakage through TXV causes rapid increase in suction pressure at the onset of the OFF cycle. The leakage rate through TXV in the model depends upon the flow area during the off cycle. This parameter is to be provided as an input and calibrated to match pressure profiles.

The cyclic degradation coefficient is evaluated for cases 1 and 3. The parameters used in evaluation for Cd are are within 4% of experiment data. However, due to the mathematical form of Cd equation, the deviation of estimated Cd is 36% from experiment data. We can however observe that even in the case of high migration, the Cd values evaluated are similar. This observation is in line with experimental testing. The pressure equalization (low pressure difference across the TXV when the system is off) does not have much impact on Cd, if no extra two-phase refrigerant flow from the evaporator exit is caused during the start-up.

Chapter 6: Analysis of evaluation of Cyclic Degradation Coefficient

6.1 Introduction

The current chapter aims at quantification of the thermal inertia effects of the code tester and its impact on the evaluation of cyclic degradation coefficient in a split air conditioning system. A new term called thermal inertia factor (TIF) is added to the formulation of the cyclic degradation coefficient to account for the thermal inertia of code tester. A conventional residential split air conditioning system is tested in two different code testers to obtain two different values of the cyclic degradation coefficient. A physically based model of code tester is developed using Modelica and validated with experimental data. TIFs for both these code testers are evaluated using this model and the new equation is able to predict the cyclic degradation coefficient obtained in the second setup from the results of the first setup and the TIF of the second. The current study is the first study of its kind and is expected to normalize the existing test procedures by removing variations arising from differences in code tester designs at various laboratories. Parametric studies by changing materials, air flow rates and temperatures of systems in the code tester are carried out to quantify the TIF and understand the effect of various factors on it.

6.2 Influence of thermal inertia from Code Tester

The present chapter evaluates two code testers with significantly different thermal inertia. One has a very high thermal inertia due to higher amount of material, while the other is designed to keep the thermal inertia at minimum. The higher thermal inertia code tester will be referred to as CT-A, while the one with lower thermal inertia will be referred to as CT-B. The exact geometry of these code testers is not presented here for proprietary reasons. However, the equations and calculation methods are discussed in such a detail that it may be applied to any design for a reader interested in conducting a similar analysis.

The product of mass and specific heat capacity of materials at different regions along airflow direction for CT-A are plotted in Figure 6.1. An airflow duct is made up of three layers: an insulation foam surrounded by steel plates on either side. Only the regions between the two thermocouple grids (see Figure 5.7), is included because the region after the second TC grid does not influence the measured temperature difference used for evaluating capacity. We can observe that the thermal mass is very well distributed throughout the code tester and there is no region which may be used as the dominating thermal inertia effect (say >90%) region mentioned in the standard. The mixer has one of the smallest thermal inertia, but it lies entirely along the airflow passage and will capture much more heat than a duct.

To capture the dynamic response of various regions of the code tester, a model is constructed using components from the Modelica Standard Library [164] and Buildings Library [229]. The models for different components of Code Tester are discussed in the previous chapter. The same models are used but with different

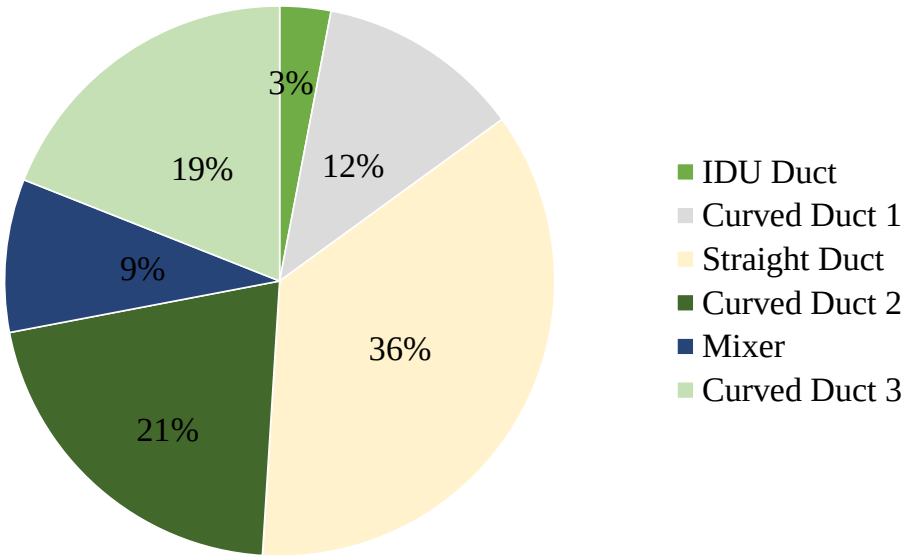

Figure 6.1: Distribution of thermal inertia of CT-A

boundary conditions to simulate the heater test. Model diagram of the heater test of Code Tester is shown in Figure 6.2.

The cyclic heater behavior is simulated by providing a square profile for temperature as a function of time as input, using a `TimeTable` block. During the off cycle, the temperature equals the room temperature and during the on cycle, it equals the temperature corresponding to the temperature available for sensible heat increase of the air stream corresponding to the heater capacity.

The model is run with Radau-IIa solver with a tolerance of 1e-6. The data is validated with temperature readings available at the outlet thermocouple grid and mixer location from the heater test for CT-A (see Figure 6.3 and Figure 6.4). The model shows a good match with trends from experimental data and can be used to investigate behavior of the code tester.

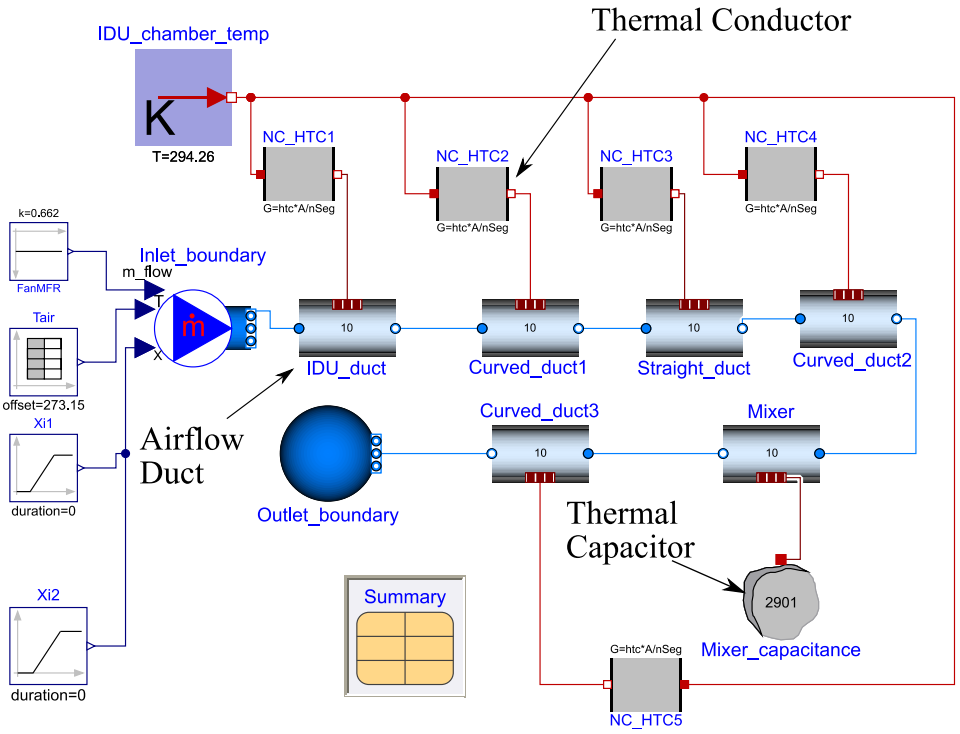

Figure 6.2: Model diagram for heater test with CT-A

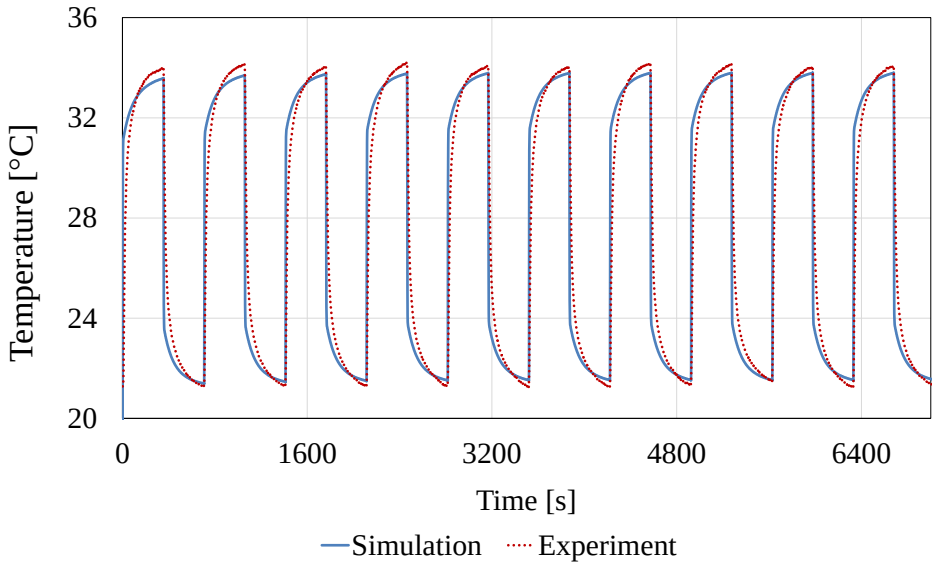

Figure 6.3: Temperature Validation of Model at Outlet TC grid

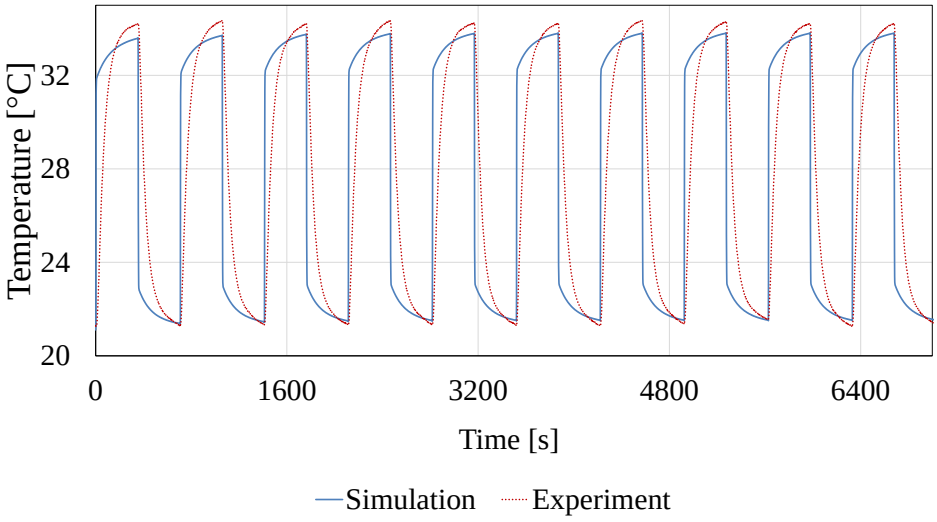

Figure 6.4: Temperature Validation of Model at Mixer TC grid

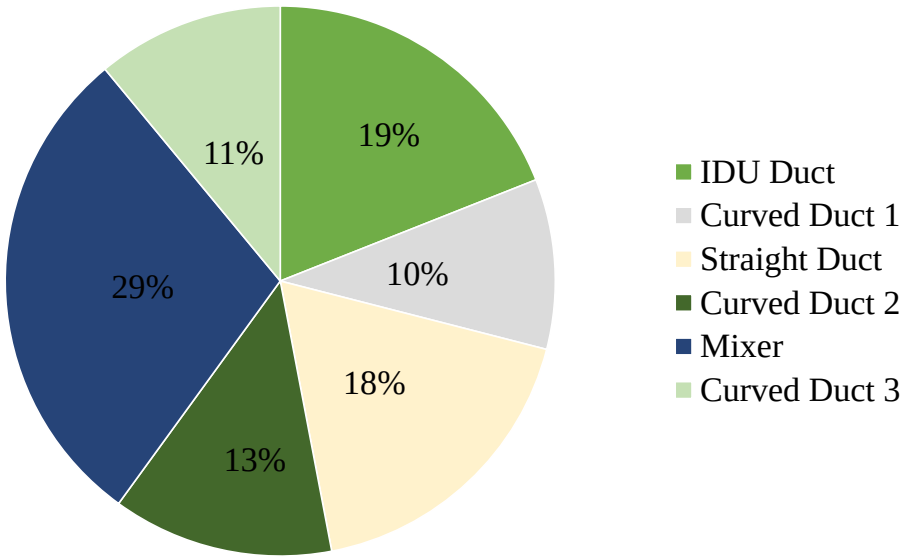

Figure 6.5: Net heat stored in code tester during cycling with heater

The heat stored in different regions of the code tester can be evaluated by integrating the capacity measured across the inlet and outlet of individual components from the model. The results are plotted in Figure 6.5. These percentages are much different from the plot of thermal inertia (Figure 6.1). One of the main reasons for the deviation is that the steel plate on the outside, having large thermal inertia does not contribute to the cyclic heat transfer. The mixer does indeed store the highest amount of heat in the code tester, but it is by no means a dominating contribution (>90%). As described earlier (Equation (1.8)), the code tester correction will be much smaller (29% of the actual) as per AHRI Standard 210/240 (2017) [162] standard.

6.3 New Correction Method to reduce Code Tester influence

A new term defined as thermal inertia factor (TIF) is proposed for improving the code tester correction to the total measured capacity. Cyclic degradation coefficient is measured for the same split AC system using CT-A and CT-B. TIF for both these code testers is evaluated and then an attempt is made to remove the influence of code tester on the cyclic degradation coefficient.

As shown earlier in the Section 6.2, a single component may not be able to represent the thermal inertia effects of the code tester correctly. The thermal inertia factor is defined as the ratio of integrated heat transfer to the code tester to the integrated total capacity of the tested equipment Equation (6.1).

$$TIF = \frac{\int_0^{t_o} \dot{Q}_{th} dt}{\int_0^{t_o} \dot{Q}_{cyc,dry,ideal} dt} \approx \frac{\int_0^{t_o} \dot{Q}_{th} dt}{\bar{\dot{Q}}_{heater} \Delta t} \tag{6.1}$$

The ideal dry test cyclic cooling capacity Equation (6.2) is the cooling capacity corrected for the code tester and is an unknown. Note that Equation (6.2) is equivalent to the differential version of Equation (1.8), without ignoring the contributions of the non-dominant thermal inertia regions.

$$\dot{Q}_{cyc,dry,ideal} = \dot{Q}_{cyc,dry} + \dot{Q}_{th} \tag{6.2}$$

If the tested equipment, i.e., capacity source, is an electric heater, it may be assumed to be instantly on and off. So the integral in the denominator of Equa-

tion (6.1) can be evaluated. This value is evaluated to be 6.67% for CT-A and 2.07% for CT-B when a 9 kW heater is used for the heater test described in Section 1.2.6.

When a 1.5 TR residential split AC system was subject to cyclic C and D Tests as per the AHRI Standard 210/240 (2017) [162], the cyclic degradation coefficient with CT-A is 0.17 and with CT-B is 0.14. The objective of the research is to reduce this variation arising from the variation of code tester thermal inertia.

Equation (6.3), shows the equation of cyclic degradation coefficient by substituting the definitions of CLF and PLF.

$$C_d = \frac{1 - \frac{\frac{\int_0^{t_o} \dot{Q}_{cyc,dry}\,dt}{\int_0^{t_o} \dot{W}_{cyc,dry}\,dt}}{\frac{\dot{Q}_{ss,dry}}{\dot{W}_{ss,dry}}}}{1 - \frac{\int_0^{t_o} \dot{Q}_{cyc,dry}\,dt}{\dot{Q}_{ss,dry} t_c}} \tag{6.3}$$

We can assume that the C-Test parameters are same for both systems since the thermal inertia effects are dynamic in nature. Additionally, as per Goldschmidt et al. (1980) [155], since the cyclic power consumption has negligible degradation effect, we can assume that the work done in D-Test with both code testers is constant. This enables grouping different constants into sets K1 and K2 (Equation (6.4) and (6.5)).

$$\frac{1}{K_1} = \frac{\dot{Q}_{ss,dry}}{\dot{W}_{ss,dry}} \left(\int_0^{t_o} \dot{W}_{cyc,dry}\,dt \right) \tag{6.4}$$

$$\frac{1}{K_2} = \frac{1}{\dot{Q}_{ss,dry} t_c} \tag{6.5}$$

Substituting K_1 and K_2 in Equation (6.3), we obtain Equation (6.6). The integrated cooling capacity $\int_0^{t_o} \dot{Q}_{cyc,dry} dt$ is experimental value and involves the thermal inertia effects from code tester.

$$C_d = \frac{1 - K_1 \left(\int_0^{t_o} \dot{Q}_{cyc,dry} dt \right)}{1 - K_2 \left(\int_0^{t_o} \dot{Q}_{cyc,dry} dt \right)} \tag{6.6}$$

Substituting the ideal cooling capacity from Equation (6.2), we obtain Equation (6.7).

$$C_d = \frac{1 - K_1 \left(\int_0^{t_o} \dot{Q}_{cyc,dry,ideal} - \dot{Q}_{th} dt \right)}{1 - K_2 \left(\int_0^{t_o} \dot{Q}_{cyc,dry,ideal} - \dot{Q}_{th} dt \right)} \tag{6.7}$$

Finally, if we can substitute TIF from Equation (6.3), to obtain the final form shown in Equation (6.1).

$$C_d = \frac{1 - K_1 \left(\int_0^{t_o} \dot{Q}_{cyc,dry,ideal} dt \right) (1 - TIF)}{1 - K_2 \left(\int_0^{t_o} \dot{Q}_{cyc,dry,ideal} dt \right) (1 - TIF)} \tag{6.8}$$

Ideal cyclic degradation coefficient can be defined as the value of Cd measured with a code tester with zero thermal inertia. Substituting TIF = 0, in Equation (6.8), we obtain Equation (6.9) for ideal Cd.

$$C_{d,ideal} = \frac{1 - K_1 \left(\int_0^{t_o} \dot{Q}_{cyc,dry,ideal} dt \right)}{1 - K_2 \left(\int_0^{t_o} \dot{Q}_{cyc,dry,ideal} dt \right)} \tag{6.9}$$

TIF can be evaluated for the heater test, but not for the case of D-Test. For the purpose of the present discussion, the value of TIF evaluated for the heater test

flow conditions is assumed to equate to the TIF during the D-Test. It is essential to understand the behavior of this term when the inlet flow conditions to the code tester are modified. Parametric study of the flow conditions like chamber temperature, heater capacity, and air flow rate to apply suitable scaling factors to the heater test TIF is part of future work. The ideal integrated cooling capacity may be evaluated from Equation (6.8) since measured Cd, TIF, K1 and K2 are available. Finally, Equation (6.9) may be used to evaluate ideal Cd. The results of these calculations are shown in Table 6.1. It can be observed that the ideal cooling capacity predicted is fairly close, but the evaluated ideal Cd is different. The calculation does capture qualitative trends. CT-A with higher thermal inertia needs more correction from measured Cd to ideal Cd, compared to CT-B.

Table 6.1: Evaluation of Ideal Cd for CT-A and CT-B

Code Tester	TIF	Cd	$\int_0^{t_o} \dot{Q}_{cyc,dry} dt$	$\int_0^{t_o} \dot{Q}_{cyc,dry,ideal} dt$	Cd_{ideal}
-	[-]	[-]	[W − hr]	[W − hr]	[-]
CT-A	6.67	0.17	444.3	474.1	0.10
CT-B	2.07	0.14	461.3	471.4	0.12

The code tester model is used to conduct a parametric study for different volume flow rates and inlet air temperatures to understand the behavior of TIF. The results are shown in Figure 6.6. The two cases plotted are fixed volume flow rate and fixed temperature across all the heaters. These are the two variables, which determine the airflow inlet conditions to the code tester. It can be observed from the graph that the volume flow rate is the main factor affecting TIF. The heater

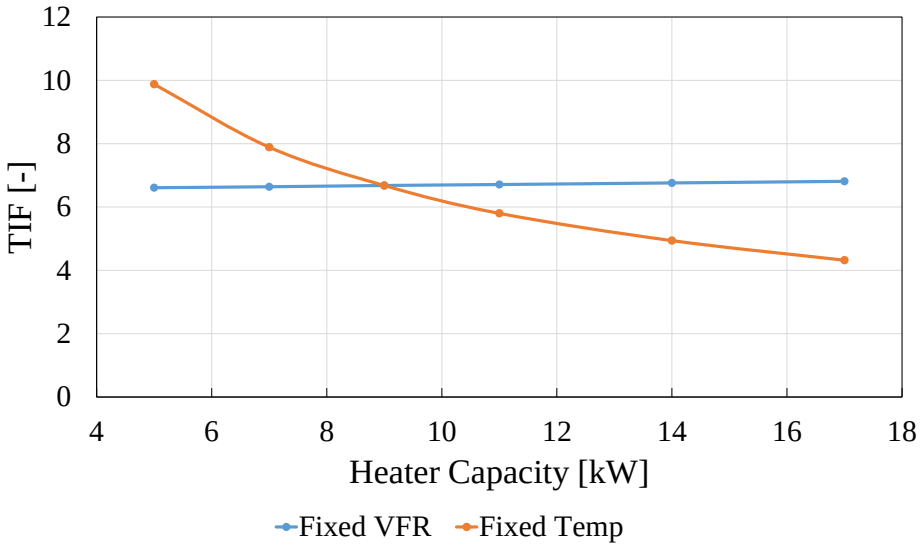

Figure 6.6: Parametric study with code tester airflow variables

test which is validated is at the intersection point. The thermal inertia factors are expected to lie within the boundary defined by these two extreme cases.

6.4 Measurement uncertainty

In the previous sections, effects of thermal inertia of code testers on the variations in the measured values of the cyclic degradation coefficient were discussed and a strategy to reduce them was presented. Another important aspect in understanding the variation in the measured value of the cyclic degradation coefficient from different tests is the uncertainty associated with its measurement.

The law of propagation of uncertainty is reliable only if the following conditions exist: (a) negligible non-linearity of function, (b) availability of analytic expression without discontinuity and (c) contributory uncertainties are small [231]. The Guide

to the Expression of Uncertainty in Measurement [232], published Supplement 1 in 2008 that describes the Monte Carlo method as a general numerical implementation of the propagation of probability distributions that can be expected to provide results free of the approximations involved in the original GUM uncertainty framework. Monte Carlo method is more reliable for a wide range of measurement problems and so this method is used for the current investigation.

The general steps involved in a Monte Carlo simulation are [233]:

1. Determine system characteristics (defining inputs, parameters, outputs and system model).

2. Determine inputs and parameters subject to uncertainty and assume or observe distribution characteristics.

3. Apply pseudo-random sampling to calculate values for input and parameter random vectors.

4. Calculate and output vector using the deterministic model.

5. Analyze the results using statistical techniques.

A comprehensive evaluation of uncertainties is conducted by including systematic uncertainties from instrumentation, calibration and also the random uncertainties. For the purpose of discussion, only the case of temperature measurement at the inlet of indoor unit (TIDDB) is described. The other input parameters (see Table 6.2) for uncertainty follow similar procedure. TIDDB is measured using a thermocouple grid, with 12 T-type thermocouples. The uncertainty associated with

each thermocouple is 0.9 °F. Whenever the value of a test result is determined by several independent methods, then the test result and its assoicated uncertainty may be determined by weighting the means, random uncertainties and systematic uncertainties of various methods. The weighting factor for 12 thermocouples as per ASME PTC 19.1-2013 [234] in Appendix A-2 is calculated using Equation (6.11). The instrument bias for the thermocouple grid is 0.26°F (Equation (6.12)).

$$b_x = 0.9°\text{F} \tag{6.10}$$

$$w_i = \frac{(1/b_x)^2}{\sum_{i=1}^{12}(1/b_x)^2} = \frac{1}{12} \tag{6.11}$$

$$b_{\bar{x}} = \sqrt{\sum_{i=1}^{12}(w_i b_x)^2} = 0.26°\text{F} \tag{6.12}$$

The thermocouples are calibrated with a water bath having systematic uncertainty (b_c) of 0.02 °F. A random uncertainty (s_c) of 0.017°F is noted for the calibration. The main purpose of the calibration process is to reduce the large known systematic errors to some acceptable level. The thermocouples calibrated with the bath are much more accurate and so the systematic uncertainty of the thermocouple grid is taken as the root of sum of square of the systematic and random uncertainty of the water bath used for calibration (Equation (6.13).

$$b_{tot} = \sqrt{b_c^2 + s_c^2} \tag{6.13}$$

Finally, after calibration, a few readings of thermocouple grid are taken to evaluate the random uncertainty. The standard deviation of temperature readings

is 0.012°F. Table 6.2 lists all the variables with their uncertainties for the evaluation of steady dry-coil C-Test based parameters in the value of Cd. Standard error, which is the standard deviation of the mean value of the measurement, is not included in the estimation. Instead standard deviation itself is used. This is because the modern data acquisition systems take several readings and the value recorded is an averaged one itself. Including standard error in evaluation of error may lead to severe under-prediction of uncertainty.

Table 6.2: Uncertainties for evaluation of Cd

Variable	Unit	Systematic	Random
TIDDB	°F	0.013	0.012
TIDDP	°F	0.101	0.018
TLDB	°F	0.013	0.063
TLDP	°F	0.101	0.031
TODDB	°F	0.013	0.037
PV	inch H_2O	0.001	0.0064
PSTAT	inch H_2O	0.002	0.0082
PATM	inch Hg	0.003	0.0505
Total Power	W	8.18	5.622
Nozzle Area	ft^2	0.00035	0.0

For evaluation of the Monte Carlo simulation, MATLAB [71] is used. Normal inverse cumulative distribution function `norminv` is used to generate population of the input variables from Table 6.2.

To generate a population of PATM (see Table 6.2), by combining both systematic and random errors, the approach followed by Wilson and Smith (2013) [235] is adopted. The input arguments for `norminv` function are a random variable generated by function `rand`, mean of measured value and systematic uncertainty of the calibrated variable. The random variable is added to this distribution by another `norminv` function, with mean at 0 and standard deviation equal to the random uncertainty. The values of systematic and random uncertainty are taken from Table 6.2. A sample code in MATLAB for the same is shown below. Similar code can be used to generate population for all the other variables.

```
% MATLAB Code to generate population for variable
for j=1:pop_size
    PATM(j) = norminv(rand,29.21,0.003)+norminv(rand,0,0.0505);
end
```

There are many situations where systematic errors for some of the parameters are correlated. This is applicable when the same apparatus is used to measure different parameters or when different equipment is calibrated to the same standard [234]. In the evaluation of Cd, all the thermocouples are calibrated with the same water bath and will have correlated systematic uncertainty. As per the recommendation in GUM Supplement 1, the only variation for correlated systematic errors is sampling from a multivariate distribution. However, in the case of thermocouples they are assumed to be perfected correlated with each other with a co-variance of 1. So, the same `norminv` function can be used for correlated systematic uncertainty as shown in the code snippet below. The same random number for generation of systematic uncertainty is passed to the systematic uncertainty portion of the population generation. Since the random uncertainty portion is not correlated, a separate random number is used for that case.

```
% MATLAB Code for correlated systematic uncertainty
for j=1:pop_size
    Tdb_corr = rand;
    TIDDB(j) = norminv(Tdb_corr,80.42,0.013)+norminv(rand,0,0.012);
    TLDB(j) = norminv(Tdb_corr,53.34,0.013)+norminv(rand,0,0.063);
end
```

After generating population of input variables, the population for output variables can be generated. The code snippet below shows evaluation of population for the total steady state cooling capacity from C-Test using a user-defined function QTCP. After the population of the cooling capacity is generated, the mean and standard deviation can be evaluated using `mean` and `std` functions in MATLAB. Similar formulation is used to evaluate mean and standard deviation for the steady state EER.

```
% MATLAB Code to generate output population
paramMatrix = [TIDDB;TIDDP;TLDB;TLDP;PATM;PSTAT;PV;Area_nozzle];
for j=1:pop_size
    Q_ss(j) = QTCP(paramMatrix(:,j));
end
Mean_QTCP = mean(Q_ss);
MCMUncert_QTCP = std(Q_ss);
```

For the cyclic D-test, it is necessary to evaluate integrated cooling capacity and cyclic EER. The variables, which vary in the D-test are TLDB and Total Power. The volume flow rate on the indoor unit also changes as the dampers are turned on and off. However, the dampers are adjacent to the indoor unit and the volume flow rate over the

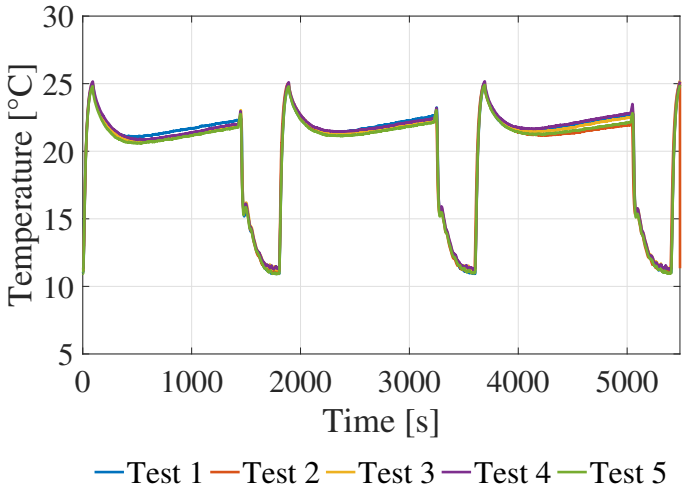

Figure 6.7: TLDB for five cyclic D-Tests

nozzles is unaffected. A time array during the on-cycle consisting of 450 seconds is taken for both TLDB and total power. Systematic uncertainty is assumed to be the same as the C-Test and is correlated with the same random variable. However, the value of random uncertainty is different from that of the C-Test. Experimental data is used to estimate random uncertainty.

The temperature at the leaving thermocouple grid is measured during five cyclic D-tests and plotted in Figure 6.7. It can be observed that temperatures are fairly close to each other. Each test consists of three on-cycles. Temperatures across each of these three on-cycles are plotted together as shown in Figure 6.8. Thus in total, there are 15 values of temperature for each 1-second interval of TLDB from 0 to 450 seconds. Standard deviation for these 15 values at all the grid points are evaluated using `std` function and plotted in Figure 6.9. Apart from a few outlier points at the beginning and end, the value is constant. The average value of standard deviation across the values in Figure 6.9 is 0.23 °C = 0.35 °F

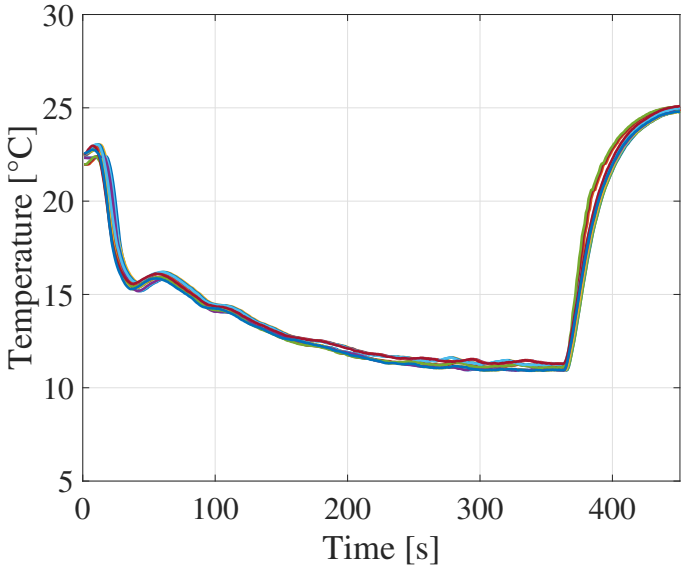

Figure 6.8: Plotting TLDB for all on-cycles from the five cyclic D-Tests

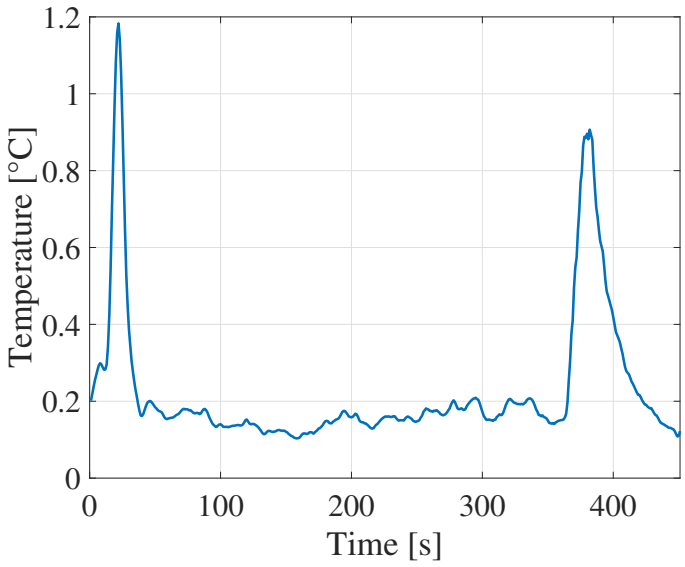

Figure 6.9: Standard deviation for TLDB array

The population of dynamic inputs for TLDB and total power can be generated now as shown below.

```
% Generate population of dynamic inputs
for j=1:pop_size
    for k=1:length(transpose(GRIDLVGUNITS))
        TLDB_D(k,j)= norminv(Tdb_corr,GRIDLVGUNITS(k),0.013)
                +norminv(rand,0,0.35);
        POW_D(k,j)= norminv(pow_corr,POWER(k),8.022)
                +norminv(rand,0,1.623);
    end
end
```

The cooling capacity and EER can be evaluated at each time grid point using the same user-defined function `QTCP`. With all the variables now available, population for Cd is generated and statistics calculated. Summary of the Monte Carlo evaluation is shown in Table 6.3. It can be observed that the experimental data matches well within the uncertainty for the steady C-Test conditions. However, due to the lack of volume flow rate cycling of D-Test, the integrated cooling capacity is over-predicted by the simulation. The standard deviation of Cd evaluated from simulation is 0.006. For the five cyclic tests conducted, the standard deviation measured is 0.007. For a 95% confidence interval, the total variation is Cd = 0.012, which is roughly 8% of the value of Cd.

If the values of acceptable uncertainty from ASHRAE 41.2 are used (Systematic = 0.1 °F, Random = 0.2 °F for temperature, 0.005 inch water for differential pressure), then the deviation in measured value of Cd = 11.4% for a 95% confidence interval. The

measurement uncertainty is responsible for the variation in the values of ideal Cd in Table 6.1.

Table 6.3: Uncertainties for evaluation of Cd

Variable	Unit	MC Mean	MC Std Dev	Expt Mean
Airflow	$ft^3\,min^{-1}$	615	3.54	615
Q_{ss}	$Btu\,hr^{-1}$	17339	105.04	17214
EER_{ss}	$Btu\,hr^{-1}\,W^{-1}$	13.33	0.117	13.23
q_{cyc}	Btu	1577	9.61	1516
EER_{cyc}	$Btu\,hr^{-1}\,W^{-1}$	11.85	0.113	11.42
Cd	[-]	0.1355	0.0055	0.17

Total deviation observed between Cd measured from CT-A and CT-B is about 20% and half of it is from measurement uncertainty. Remaining influence is from the effect of thermal inertia of code testers. It is therefore necessary to develop a more reliable method to rate cyclic performance of air conditioners. The new term to calculate cyclic variation should have much lesser variation in measurement. Design of code testers should also be standardized to account for uniform effect of thermal inertia across various tests. Also their designs should be such that the values of thermal inertia factor are low.

Chapter 7: Summary

7.1 Conclusions

This thesis provides several innovative ideas for more energy efficient use of HVAC systems to provide space heating and cooling in buildings.

To address the shortcomings of existing personal conditioning systems (PCS), four such systems are analyzed through multi-physics modeling to understand the extent of their benefits and shortcomings. Three of the systems use different thermal storages like chilled water, ice storage and PCM with a closed water loop, and a fourth system uses vapor compression cycle with PCM. All the systems are in the weight range of 19-31 kg. Chilled water-based system and ice storage based system are cost-effective compared to the other systems. The vapor compression system consumes roughly 40% more battery power than the water-based systems during cooling operation. However, vapor compression system has other benefits from usability like easier thermal recharge and closed operation for the system.

The VCS with PCM is developed into a technology called Roving Comforter (RoCo). The first prototype used thermosiphon for recharging the PCM, which required eight hours to re-solidify the PCM after a two hour cooling operation. A validated dynamic model for thermosiphon is developed and then exercised to evaluate performance with compressed expanded natural graphite (CENG) enhanced versions of the PCM. Based on the results,

2.2% volume fraction CENG is considered the most promising due to 51% reduction in the discharge time for a 5% increase in weight. The coefficient of performance for overall operation increases by 24%.

Due to regulations on the use of R134a, the dynamic performance of RoCo with a natural refrigerant (R290) is studied. Switching to R290 shows 33% improvement in the coefficient of performance, with additional benefits like reduced noise during cooling operation and lesser system weight also expected.

The newer prototypes of RoCo using CENG delivered 4-hour cooling operation with 6.5-hour recharge time by thermosiphon. The performance of heat pump based recharge at different compressor RPM was evaluated. The recharge period from heat pump operation showed 35-55% reduction in time from thermosiphon, with a penalty of 30-35% on the overall COP. However, the power consumption is in the order of a few hundred Wh and is small compared to the savings from building HVAC, which typically consumes power in kWh. Thus, heat pump recharge shows promise in comparison to the thermosiphon and will be used in future prototypes.

Next, refrigerant migration physics is investigated for a conventional air-conditioner undergoing cyclic testing in a code tester. The dynamic model shows the good prediction for temperature, pressure and power measurements. Slip-ratio based void fraction model is used to estimate refrigerant charge in each component. Refrigerant leakage through both compressor and TXV is modeled. The model also shows robustness during off-cycle of a cyclic test under the conditions of zero refrigerant flow. Validation for the percentage of refrigerant in different portions of the system shows a good overall prediction for steady state test experiment. Finally, the limitations of current HVAC rating procedure and specifically the contribution of the code tester on the cyclic degradation coefficient (Cd)

is investigated. Deviations arising from assumptions used in the calculation procedure are highlighted using a validated dynamic model for the code tester. A new term called thermal inertia factor is defined and the Cd formula is modified using the thermal inertia factor to remove the impact of a specific code tester design from the measured value of Cd. Discussions on future directions aimed at improving Cd evaluation procedure is presented.

7.2 Contributions

The main contributions of this thesis are dynamic, highly reusable models capable of analyzing a variety of complex two-phase refrigerant systems. Multi-physics insights are also available for models incorporating electrodynamics and mechanics equations alongside the thermal-fluid sciences.

The models are used to improve the performance of a few existing systems. It is expected to provide interesting insights on the systems analyzed for researchers developing similar technology and at the same time guidance on developing system models to simulate design space. The contributions from the thesis are classified into groups below:

1. Thermosiphon modeling
    - First demonstration of two-phase thermosiphon modeling with Modelica in literature
    - First validated numerical model for PCM-driven thermosiphon in literature
2. Personal Conditioning Systems
    - Identified and compared system parameters for the lightest design of four innovative PCS with different thermal storage through development of multi-

physics models

- Energy efficiency improvement for RoCo by identifying best operating parameters in studies involving different refrigerants, phase change materials and recharge options

3. Phase Change Material Modeling

   - Empirical correlation for solidification and melting of PureTemp 37 by helical coil refrigerant tubes at RoCo operating temperatures
   - Strategies to implement simple and accurate PCM models for system simulation in thermo-fluid systems

4. Cyclic performance of air conditioner

   - Develop dynamic modeling framework incorporating recommended best practices for zero flow modeling, compressor leakage, asymmetric refrigerant circuitry and void fraction model-based prediction of refrigerant charge
   - Develop generic reusable models for code tester components which can be integrated with system model of air conditioner
   - Provide insights into refrigerant migration physics during cyclic operation of a conventional air conditioner

5. Rating standards for evaluating cyclic performance of air conditioners

   - Quantify the effects of thermal inertia of code tester on the measured cyclic degradation coefficient
   - Identification of uncertainty in the measured value of cyclic degradation coefficient using Monte Carlo simulation

- Recommend best practices for measurement of accurate cyclic degradation of the conventional air conditioner

Bibliography

[1] U.S. Energy Information Administration. Independent statistics & analysis, 2017. [Online; accessed 14-April-2017].

[2] Bryan P Rasmussen. *Dynamic modeling and advanced control of air conditioning and refrigeration systems*. PhD thesis, 2005.

[3] Vahid Vakiloroaya, Bijan Samali, Ahmad Fakhar, and Kambiz Pishghadam. A review of different strategies for hvac energy saving. *Energy conversion and management*, 77:738–754, 2014.

[4] María Ibañez-Puy, Javier Bermejo-Busto, César Martín-Gómez, Marina Vidaurre-Arbizu, and José Antonio Sacristán-Fernández. Thermoelectric cooling heating unit performance under real conditions. *Applied Energy*, 200:303–314, 2017.

[5] Yongqiang Luo, Ling Zhang, Zhongbing Liu, Yingzi Wang, Fangfang Meng, and Lei Xie. Modeling of the surface temperature field of a thermoelectric radiant ceiling panel system. *Applied Energy*, 162:675–686, 2016.

[6] Mohammad Saffari Tabalvandani, Alvaro de Gracia Cuesta, César Fernàndez Camon, and Luisa F Cabeza. Simulation-based optimization of pcm melting temperature to improve the energy performance in buildings. *Applied Energy, 2017, In Press*, 2017.

[7] Na Luo, Tianzhen Hong, Hui Li, Ruoxi Jia, and Wenguo Weng. Data analytics and optimization of an ice-based energy storage system for commercial buildings. *Applied Energy*, 204:459–475, 2017.

[8] TX Li, DL Wu, F He, and RZ Wang. Experimental investigation on copper foam/hydrated salt composite phase change material for thermal energy storage. *International Journal of Heat and Mass Transfer*, 115:148–157, 2017.

[9] Xinqiao Yu, Da Yan, Kaiyu Sun, Tianzhen Hong, and Dandan Zhu. Comparative study of the cooling energy performance of variable refrigerant flow systems and variable air volume systems in office buildings. *Applied Energy*, 183:725–736, 2016.

[10] Pradeep Bansal. High efficiency novel window air conditioner. *Applied Energy*, 156:311–320, 2015.

[11] Kathrin Menberg, Yeonsook Heo, Wonjun Choi, Ryozo Ooka, Ruchi Choudhary, and Masanori Shukuya. Exergy analysis of a hybrid ground-source heat pump system. *Applied Energy*, 204:31–46, 2017.

[12] Zhihua Zhou, Zhiming Zhang, Guanyi Chen, Jian Zuo, Pan Xu, Chong Meng, and Zhun Yu. Feasibility of ground coupled heat pumps in office buildings: A china study. *Applied Energy*, 162:266–277, 2016.

[13] Omar Labban, Tianyi Chen, Ahmed F Ghoniem, John H Lienhard, and Leslie K Norford. Next-generation hvac: Prospects for and limitations of desiccant and membrane-based dehumidification and cooling. *Applied Energy*, 200:330–346, 2017.

[14] Dominic OConnor, John Kaiser Calautit, and Ben Richard Hughes. A novel design of a desiccant rotary wheel for passive ventilation applications. *Applied Energy*, 179:99–109, 2016.

[15] Tao Yu, Per Heiselberg, Bo Lei, Chen Zhang, Michal Pomianowski, and Rasmus Jensen. Experimental study on the dynamic performance of a novel system combining natural ventilation with diffuse ceiling inlet and tabs. *Applied energy*, 169:218–229, 2016.

[16] Daniel Bacellar, Vikrant Aute, Zhiwei Huang, and Reinhard Radermacher. Design optimization and validation of high-performance heat exchangers using approximation assisted optimization and additive manufacturing. *Science and Technology for the Built Environment*, 23(6):896–911, 2017.

[17] Jun Mei and Xiaohua Xia. Energy-efficient predictive control of indoor thermal comfort and air quality in a direct expansion air conditioning system. *Applied Energy*, 195:439–452, 2017.

[18] Jingchun Shen, Xingxing Zhang, Tong Yang, Llewellyn Tang, Ali Cheshmehzangi, Yupeng Wu, Guiqin Huang, Dan Zhong, Peng Xu, and Shengchun Liu. Characteristic study of a novel compact solar thermal facade (stf) with internally extruded pin–fin flow channel for building integration. *Applied Energy*, 168:48–64, 2016.

[19] Adams Rackes, Ana Paula Melo, and Roberto Lamberts. Naturally comfortable and sustainable: Informed design guidance and performance labeling for passive commercial buildings in hot climates. *Applied Energy*, 174:256–274, 2016.

[20] Ignacio Acosta, Miguel Ángel Campano, and Juan Francisco Molina. Window design in architecture: Analysis of energy savings for lighting and visual comfort in residential spaces. *Applied Energy*, 168:493–506, 2016.

[21] Scott Hackel and Amanda Pertzborn. Effective design and operation of hybrid ground-source heat pumps: three case studies. *Energy and Buildings*, 43(12):3497–3504, 2011.

[22] YF Liu and RZ Wang. Method to design optimal scheme for cold storage air conditioning system. *Energy conversion and management*, 43(17):2357–2367, 2002.

[23] Vahid Vakiloroaya, Jafar Madadnia, and Bijan Samali. Modeling and performance prediction of an integrated central cooling plant for hvac energy efficiency improvement. In *Building Simulation*, volume 6, pages 127–138. Tsinghua Univ Press, 2013.

[24] Inge Blom, Laure Itard, and Arjen Meijer. Lca-based environmental assessment of the use and maintenance of heating and ventilation systems in dutch dwellings. *Building and Environment*, 45(11):2362–2372, 2010.

[25] Jennifer OConnor. Survey on actual service lives for north american buildings. In *Woodframe housing durability and disaster issues conference, Las Vegas*, pages 1–9, 2004.

[26] Buildings Energy Data Book. Us department of energy, 2011, 2010.

[27] Weimin Wang, Srinivas Katipamula, Hung Ngo, Ronald Underhill, Danny Taasevigen, and Robert Lutes. Field evaluation of advanced controls for the retrofit of packaged air conditioners and heat pumps. *Applied Energy*, 154:344–351, 2015.

[28] Hui Zhang, Edward Arens, and Wilmer Pasut. Air temperature thresholds for indoor comfort and perceived air quality. *Building Research & Information*, 39(2):134–144, 2011.

[29] Gail Brager, Hui Zhang, and Edward Arens. Evolving opportunities for providing thermal comfort. *Building Research & Information*, 43(3):274–287, 2015.

[30] Stanley Aronoff and Audrey G Kaplan. *Total workplace performance: Rethinking the office environment*. Wdl Publications, 1995.

[31] RG Kapadia, Sanjeev Jain, and RS Agarwal. Transient characteristics of split air-conditioning systems using r-22 and r-410a as refrigerants. *HVAC&R Research*, 15(3):617–649, 2009.

[32] ARI Standard 210/240: Performance Rating of Unitary Air-Conditioning & Air-Source Heat Pump Equipment. Standard, Air Conditioning, Heating, and Refrigeration Institute, Arlington, VA, 2008.

[33] Sven Erik Mattsson, Hilding Elmqvist, and Martin Otter. Physical system modeling with modelica. *Control Engineering Practice*, 6(4):501–510, 1998.

[34] Karl Johan Åström, Hilding Elmqvist, Sven Erik Mattsson, et al. Evolution of continuous-time modeling and simulation. In *ESM*, pages 9–18, 1998.

[35] Christopher Laughman and Hongtao Qiao. Mass conserving models of vapor compression cycles. In *Proceedings of the 11th International Modelica Conference, Versailles, France, September 21-23, 2015*, number 118, pages 759–767. Linköping University Electronic Press, 2015.

[36] Peter Fritzson. *Principles of object-oriented modeling and simulation with Modelica 3.3: a cyber-physical approach*. John Wiley & Sons, 2014.

[37] Hubertus Tummescheit and Jonas Eborn. Design of a thermo-hydraulic model library in Modelica. In *12th European Simulation Multiconference*, 1998.

[38] Hubertus Tummescheit, Jonas Eborn, and Falko Wagner. Development of a Modelica base library for modeling of thermo-hydraulic systems. In *Modelica Workshop 2000 Proceedings*, pages 41–51, 2000.

[39] Hubertus Tummescheit. Design and implementation of object-oriented model libraries using modelica. *PhD Theses*, 2002.

[40] J Eborn, Hubertus Tummescheit, and W Wagner. Thermoflow, a thermo-hydraulic library in modelica. Technical report, 2001.

[41] Hilding Elmqvist, Hubertus Tummescheit, and Martin Otter. Object-oriented modeling of thermo-fluid systems. In *3rd International Modelica Conference*, pages 269–286, 2003.

[42] Jakob Munch Jensen. Dynamic modeling of thermofluid systems. 2003.

[43] Torge Pfafferott and Gerhard Schmitz. Modelling and transient simulation of CO 2-refrigeration systems with Modelica. *International journal of refrigeration*, 27(1):42–52, 2004.

[44] Torge Pfafferott and Gerhard Schmitz. Implementation of a modelica library for simulation of refrigeration systems. In *Paper presented at the 3rd International Modelica Conference*, 2003.

[45] Francesco Casella, Martin Otter, Katrin Proelss, Christoph Richter, and Hubertus Tummescheit. The modelica fluid and media library for modeling of incompressible and compressible thermo-fluid pipe networks. In *Proceedings of the 5th International Modelica Conference*, pages 631–640, 2006.

[46] Christoph Richter. *Proposal of new object-oriented equation-based model libraries for thermodynamic systems*. PhD thesis, 2008.

[47] Hongtao Qiao. *Transient modeling of two-stage and variable refrigerant flow vapor compression systems with frosting and defrosting*. PhD thesis, 2014.

[48] Staffan Haugwitz. Modelling of microturbine systems. *MSc Theses*, 2002.

[49] Antonio Alejandro Gómez Pérez. Modelling of a gas turbine with modelica. *MSc Theses*, 2001.

[50] Rüdiger Franke, Francesco Casella, Martin Otter, Michael Sielemann, Hilding Elmqvist, Mattson Sven Erik, and Olsson Hans. Stream connectors-an extension of Modelica for device-oriented modeling of convective transport phenomena. In *Proceedings of the 7th International Modelica Conference; Como; Italy; 20-22 September 2009*, number 043, pages 108–121. Linköping University Electronic Press, 2009.

[51] Dirk Limperich, Marco Braun, K Prölß, Gerhard Schmitz, et al. System simulation of automotive refrigeration cycles. In *Proceedings of the 4th international modelica conference*, 2005.

[52] Hubertus Tummescheit, Jonas Eborn, and Katrin Prölss. Airconditioninga Modelica library for dynamic simulation of AC systems. In *Paper presented at the 4th International Modelica Conference*, 2005.

[53] Hongtao Qiao, Christopher R Laughman, Vikrant Aute, and Reinhard Radermacher. An advanced switching moving boundary heat exchanger model with pressure drop. *International journal of refrigeration*, 65:154–171, 2016.

[54] Luca Cecchinato and Ferdinando Mancini. An intrinsically mass conservative switched evaporator model adopting the moving-boundary method. *International journal of refrigeration*, 35(2):349–364, 2012.

[55] Christopher R Laughman and Hongtao Qiao. On the influence of state selection on mass conservation in dynamic vapour compression cycle models. *Mathematical and Computer Modelling of Dynamical Systems*, pages 1–22, 2017.

[56] Christopher R Laughman, Hongtao Qiao, Vikrant Aute, and Reinhard Radermacher. A comparison of transient heat pump cycle models using alternative flow descriptions. *Science and Technology for the Built Environment*, 21(5):666–680, 2015.

[57] Olaf Bauer. Modelling of two-phase flows with modelica. Master's thesis, Lund Institute of Technology, 1999.

[58] Lord Rayleigh. LIX. On convection currents in a horizontal layer of fluid, when the higher temperature is on the under side. *The London, Edinburgh, and Dublin Philosophical Magazine and Journal of Science*, 32(192):529–546, 1916.

[59] Flavio Dobran. Steady-state characteristics and stability thresholds of a closed two-phase thermosyphon. *International Journal of heat and mass transfer*, 28(5):949–957, 1985.

[60] J G Reed and C L Tien. Modeling of the two-phase closed thermosyphon. *Journal of heat transfer*, 109(3):722–730, 1987.

[61] Stéphane Lips, Valérie Sartre, Frederic Lefevre, Sameer Khandekar, and Jocelyn Bonjour. Overview of heat pipe studies during the period 2010- 2015. *Interfacial Phenomena and Heat Transfer*, 4(1), 2016.

[62] Saffa Riffat and Xiaoli Ma. Recent developments in heat pipe technology and applications: a review. *International Journal of Low-carbon Technologies*, 2(2):162–177, 2007.

[63] Amir Faghri. Review and advances in heat pipe science and technology. *Journal of heat transfer*, 134(12):123001, 2012.

[64] Charles C J Vincent and Jim B W Kok. Investigation of the overall transient performance of the industrial two-phase closed loop thermosyphon. *International Journal of heat and mass transfer*, 35(6):1419–1426, 1992.

[65] Rahmatollah Khodabandeh. Heat transfer in the evaporator of an advanced two-phase thermosyphon loop. *International journal of refrigeration*, 28(2):190–202, 2005.

[66] Rahmatollah Khodabandeh. Pressure drop in riser and evaporator in an advanced two-phase thermosyphon loop. *International journal of refrigeration*, 28(5):725–734, 2005.

[67] Penglei Zhang, Baolong Wang, Wenxing Shi, Linjun Han, and Xianting Li. Modeling and performance analysis of a two-phase thermosyphon loop with partially/fully liquid-filled downcomer. *International Journal of Refrigeration*, 58:172–185, 2015.

[68] Hainan Zhang, Zichao Shi, Kaitao Liu, Shuangquan Shao, Tingxiang Jin, and Changqing Tian. Experimental and numerical investigation on a co 2 loop thermosyphon for free cooling of data centers. *Applied Thermal Engineering*, 111:1083–1090, 2017.

[69] S I Haider, Yogendra K Joshi, and Wataru Nakayama. A natural circulation model of the closed loop, two-phase thermosyphon for electronics cooling. *Journal of heat transfer*, 124(5):881–890, 2002.

[70] S A Klein and F L Alvarado. Engineering equation solver. *F-Chart Software, Madison, WI*, 1, 2002.

[71] MATLAB Users Guide. The mathworks. *Inc., Natick, MA*, 5:333, 1998.

[72] R T Dobson and J C Ruppersberg. Flow and heat transfer in a closed loop thermosyphon. Part ITheoretical simulation. *J. Energy South. Afr*, 18:32–40, 2007.

[73] S Bodjona, E Videcoq, Richard Saurel, A Chinnayya, AM Benselama, and Y Bertin. Transient simulation of a two-phase loop thermosyphon with a model out of thermodynamic equilibrium. *International Journal of Heat and Mass Transfer*, 108:2321–2332, 2017.

[74] R Srikanth, Rohit S Nair, and C Balaji. Thermosyphon assisted melting of pcm inside a rectangular enclosure: A synergistic numerical approach. In *Journal of Physics: Conference Series*, volume 745, page 032130. IOP Publishing, 2016.

[75] Belen Zalba, José Ma Marín, Luisa F Cabeza, and Harald Mehling. Review on thermal energy storage with phase change: materials, heat transfer analysis and applications. *Applied thermal engineering*, 23(3):251–283, 2003.

[76] David Gonzalez-Nino, Lauren M Boteler, Dimeji Ibitayo, Nicholas R Jankowski, Damian Urciuoli, Iain M Kierzewski, and Pedro O Quintero. Experimental evaluation of metallic phase change materials for thermal transient mitigation. *International Journal of Heat and Mass Transfer*, 116:512–519, 2018.

[77] Muhammad Junaid Ashraf, Hafiz Muhammad Ali, Hazrat Usman, and Adeel Arshad. Experimental passive electronics cooling: Parametric investigation of pin-fin geometries and efficient phase change materials. *International Journal of Heat and Mass Transfer*, 115:251–263, 2017.

[78] Adèle Caron-Soupart, Jean-François Fourmigué, Philippe Marty, and Raphaël Couturier. Performance analysis of thermal energy storage systems using phase change material. *Applied Thermal Engineering*, 98:1286–1296, 2016.

[79] Debabrata Pal and Yogendra K Joshi. Melting in a side heated tall enclosure by a uniformly dissipating heat source. *International Journal of Heat and Mass Transfer*, 44(2):375–387, 2001.

[80] Babak Kamkari, Hossein Shokouhmand, and Frank Bruno. Experimental investigation of the effect of inclination angle on convection-driven melting of phase change material in a rectangular enclosure. *International Journal of Heat and Mass Transfer*, 72:186–200, 2014.

[81] Yvan Dutil, Daniel R Rousse, Nizar Ben Salah, Stéphane Lassue, and Laurent Zalewski. A review on phase-change materials: mathematical modeling and simulations. *Renewable and sustainable Energy reviews*, 15(1):112–130, 2011.

[82] Henry Hu and Stavros A Argyropoulos. Mathematical modelling of solidification and melting: a review. *Modelling and Simulation in Materials Science and Engineering*, 4(4):371, 1996.

[83] Piia Lamberg, Reijo Lehtiniemi, and Anna-Maria Henell. Numerical and experimental investigation of melting and freezing processes in phase change material storage. *International Journal of Thermal Sciences*, 43(3):277–287, 2004.

[84] AH Mosaffa, F Talati, H Basirat Tabrizi, and MA Rosen. Analytical modeling of pcm solidification in a shell and tube finned thermal storage for air conditioning systems. *Energy and buildings*, 49:356–361, 2012.

[85] K Azzouz, D Leducq, and D Gobin. Performance enhancement of a household refrigerator by addition of latent heat storage. *International Journal of Refrigeration*, 31(5):892–901, 2008.

[86] Hamid El Qarnia. Numerical analysis of a coupled solar collector latent heat storage unit using various phase change materials for heating the water. *Energy Conversion and Management*, 50(2):247–254, 2009.

[87] S Bakhshipour, MS Valipour, and Y Pahamli. Parametric analysis of domestic refrigerators using pcm heat exchanger. *International Journal of Refrigeration*, 83:1–13, 2017.

[88] Santosh Kumar Sahoo, Prasenjit Rath, and Mihir Kumar Das. Numerical study of phase change material based orthotropic heat sink for thermal management of electronics components. *International Journal of Heat and Mass Transfer*, 103:855–867, 2016.

[89] Y Cao and A Faghri. A numerical analysis of phase-change problems including natural convection. *Journal of Heat Transfer (Transactions of the ASME (American Society of Mechanical Engineers), Series C);(United States)*, 112(3), 1990.

[90] Corinna Leonhardt and Dirk Müller. Modelling of Residential Heating Systems using a Phase Change Material Storage System. 43:507–512, 2009.

[91] Jochen Buschle, Wolf-Dieter Steinmann, and Rainer Tamme. Analysis of steam storage systems using Modelica. In *Proceedings 5th Modelica Conference 2006*, 2006.

[92] Anton Trník, Libor Vozár, et al. Modeling of heat capacity peaks and enthalpy jumps of phase-change materials used for thermal energy storage. *International Journal of Heat and Mass Transfer*, 107:123–132, 2017.

[93] Anica Trp, Kristian Lenic, and Bernard Frankovic. Analysis of the influence of operating conditions and geometric parameters on heat transfer in water-paraffin shell-and-tube latent thermal energy storage unit. *Applied Thermal Engineering*, 26(16):1830–1839, 2006.

[94] Benjamin J. Jones, Dawei Sun, Shankar Krishnan, and Suresh V. Garimella. Experimental and numerical study of melting in a cylinder. *International Journal of Heat and Mass Transfer*, 49(15-16):2724–2738, 2006.

[95] Anica Trp. An experimental and numerical investigation of heat transfer during technical grade paraffin melting and solidification in a shell-and-tube latent thermal energy storage unit. *Solar Energy*, 79(6):648–660, 2005.

[96] E M Sparrow, S V Patankar, and Ramadhyani S. Analysis of Melting in the Presence of Natural Convection in the Melt Region. *Journal of Heat Transfer*, 99(4):520–526, 1977.

[97] Saied Mohammad Vakilaltojjar and W Saman. Analysis and modelling of a phase change storage system for air conditioning applications. *Applied Thermal Engineering*, 21(3):249–263, 2001.

[98] A H Mosaffa, F Talati, H Basirat Tabrizi, and M A Rosen. Analytical modeling of PCM solidification in a shell and tube finned thermal storage for air conditioning systems. *Energy and Buildings*, 49:356–361, 2012.

[99] Miroslaw Zukowski. Experimental study of short term thermal energy storage unit based on enclosed phase change material in polyethylene film bag. *Energy Conversion and Management*, 48(1):166–173, 2007.

[100] Michael Vynnycky and Shigeo Kimura. An analytical and numerical study of coupled transient natural convection and solidification in a rectangular enclosure. *International Journal of Heat and Mass Transfer*, 50(25-26):5204–5214, 2007.

[101] M Costa, D Buddhi, and A Oliva. Numerical simulation of a latent heat thermal energy storage system with enhanced heat conduction. *Energy Conservation Management*, Vol.39, No(3):319–330, 1998.

[102] Nourouddin Sharifi, Christopher W Robak, Theodore L Bergman, and Amir Faghri. Three-dimensional pcm melting in a vertical cylindrical enclosure including the effects of tilting. *International Journal of Heat and Mass Transfer*, 65:798–806, 2013.

[103] Abhay Dinker, Madhu Agarwal, and G. D. Agarwal. Experimental assessment on thermal storage performance of beeswax in a helical tube embedded storage unit. *Applied Thermal Engineering*, 111(September):358–368, 2017.

[104] Abdel Illah Nabil Korti and Fatima Zohra Tlemsani. Experimental investigation of latent heat storage in a coil in PCM storage unit. *Journal of Energy Storage*, 5:177–186, 2016.

[105] M H Abdel-Aziz, I Nirdosh, and G H Sedahmed. Mass and heat transfer at the outer surface of helical coils under single and two phase flow. *Applied Thermal Engineering*, 103:713–719, 2016.

[106] Srbislav B Genić, Branislav M Jaćimović, Marko S Jarić, Nikola J Budimir, and Mirko M Dobrnjac. Research on the shell-side thermal performances of heat exchangers with helical tube coils. *International Journal of heat and mass transfer*, 55(15-16):4295–4300, 2012.

[107] Xun Yang, Teng Xiong, Jing Liang Dong, Wen Xin Li, and Yong Wang. Investigation of the Dynamic Melting Process in a Thermal Energy Storage Unit Using a Helical Coil Heat Exchanger. *Energies*, 10(8):1129, 2017.

[108] Johan Åkesson. *Languages and Tools for Optimization of Large-Scale Systems*. PhD thesis, Department of Automatic Control, Lund Institute of Technology (LTH), PO Box 118 221 00 Lund, Sweden, 2007.

[109] Tyler Hoyt, Edward Arens, and Hui Zhang. Extending air temperature setpoints: Simulated energy savings and design considerations for new and retrofit buildings. *Building and Environment*, 88:89–96, 2015.

[110] Hui Zhang, Edward Arens, and Yongchao Zhai. A review of the corrective power of personal comfort systems in non-neutral ambient environments. *Building and Environment*, 91:15–41, 2015.

[111] Arsen Krikor Melikov and Gitte L Knudsen. Human response to an individually controlled microenvironment. *HVAC&R Research*, 13(4):645–660, 2007.

[112] Hui Zhang, Edward Arens, DongEun Kim, Elena Buchberger, Fred Bauman, and Charlie Huizenga. Comfort, perceived air quality, and work performance in a low-power task–ambient conditioning system. *Building and Environment*, 45(1):29–39, 2010.

[113] Yongchao Zhai, Hui Zhang, Yufeng Zhang, Wilmer Pasut, Edward Arens, and Qinglin Meng. Comfort under personally controlled air movement in warm and humid environments. *Building and environment*, 65:109–117, 2013.

[114] Fred S Bauman, Thomas G Carter, Anne V Baughman, and Edward A Arens. Field study of the impact of a desktop task/ambient conditioning system in office buildings. *ASHRAE Transactions*, 104:1153, 1998.

[115] Michal Veselý and Wim Zeiler. Personalized conditioning and its impact on thermal comfort and energy performance A review. *Renewable and Sustainable Energy Reviews*, 34:401–408, 2014.

[116] Ning Mao, Dongmei Pan, Zhao Li, Yingjie Xu, Mengjie Song, and Shiming Deng. A numerical study on influences of building envelope heat gain on operating performances of a bed-based task/ambient air conditioning (tac) system in energy saving and thermal comfort. *Applied Energy*, 192:213–221, 2017.

[117] K Tsuzuki, Edward Arens, Fred Bauman, and D Wyon. Individual thermal comfort control with desk-mounted and floor-mounted task/ambient conditioning (tac) systems. *Indoor Air, Edinburgh*, 1999.

[118] Arsen K Melikov, Radim Cermak, and Milan Majer. Personalized ventilation: evaluation of different air terminal devices. *Energy and buildings*, 34(8):829–836, 2002.

[119] Jing Du, Mingyin Chan, Dongmei Pan, and Shiming Deng. A numerical study on the effects of design/operating parameters of the radiant panel in a radiation-based task air conditioning system on indoor thermal comfort and energy saving for a sleeping environment. *Energy and Buildings*, 151:250–262, 2017.

[120] Nesreen Ghaddar, Kamel Ghali, and Walid Chakroun. Evaporative cooler improves transient thermal comfort in chilled ceiling displacement ventilation conditioned space. *Energy and Buildings*, 61:51–60, 2013.

[121] W Chakroun, N Ghaddar, and K Ghali. Chilled ceiling and displacement ventilation aided with personalized evaporative cooler. *Energy and buildings*, 43(11):3250–3257, 2011.

[122] Wilmer Pasut, Hui Zhang, Ed Arens, and Yongchao Zhai. Energy-efficient comfort with a heated/cooled chair: Results from human subject tests. *Building and Environment*, 84:10–21, 2015.

[123] Shinichi Watanabe, Toshimichi Shimomura, and Hironori Miyazaki. Thermal evaluation of a chair with fans as an individually controlled system. *Building and Environment*, 44(7):1392–1398, 2009.

[124] Jianlei Niu, Naiping Gao, Ma Phoebe, and Zuo Huigang. Experimental study on a chair-based personalized ventilation system. *Building and Environment*, 42(2):913–925, 2007.

[125] Wenfang Song, Faming Wang, and Fanru Wei. Hybrid cooling clothing to improve thermal comfort of office workers in a hot indoor environment. *Building and Environment*, 100:92–101, 2016.

[126] Haneen Hamdan, Nesreen Ghaddar, Djamel Ouahrani, Kamel Ghali, and M Itani. Pcm cooling vest for improving thermal comfort in hot environment. *International Journal of Thermal Sciences*, 102:154–167, 2016.

[127] Mariam Itani, Nesreen Ghaddar, Kamel Ghali, Djamel Ouahrani, and Walid Chakroun. Cooling vest with optimized pcm arrangement targeting torso sensitive areas that trigger comfort when cooled for improving human comfort in hot conditions. *Energy and Buildings*, 139:417–425, 2017.

[128] AD Flouris and SS Cheung. Design and control optimization of microclimate liquid cooling systems underneath protective clothing. *Annals of biomedical engineering*, 34(3):359, 2006.

[129] Huantian Cao, Donna H Branson, Semra Peksoz, Jinhee Nam, and Cheryl A Farr. Fabric selection for a liquid cooling garment. *Textile Research Journal*, 76(7):587–595, 2006.

[130] An-Shik Yang, Yang-Cheng Shih, Chun-Lung Lee, and Ming-Chen Lee. Investigation of flow and heat transfer around internal channels of an air ventilation vest. *Textile Research Journal*, 84(4):399–410, 2014.

[131] DL Oneal and S Katipamula. Performance degradation during on-off cycling of single-speed air conditioners and heat pumps: model development and analysis. *Ashrae transactions*, 97(2):316–323, 1991.

[132] WH Parken, RW Beausoliel, and GE Kelly. Factors affecting the performance of a residential air-to-air heat pump. In *ASHRAE Transactions*, volume 18, pages 43–44, 1976.

[133] Jun Wang and Yezheng Wu. Start-up and shut-down operation in a reciprocating compressor refrigeration system with capillary tubes. *International Journal of Refrigeration*, 13(3):187–190, 1990.

[134] PP Votsis, SA Tassou, DR Wilson, and CJ Marquand. Dynamic characteristics of an air-to-water heat-pump system. *International journal of refrigeration*, 15(2):89–94, 1992.

[135] MJP Janssen, JA De Wit, and LJM Kuijpers. Cycling losses in domestic appliances: an experimental and theoretical analysis. *International Journal of Refrigeration*, 15(3):152–158, 1992.

[136] Erik Björk and Björn Palm. Refrigerant mass charge distribution in a domestic refrigerator, part i: Transient conditions. *Applied Thermal Engineering*, 26(8):829–837, 2006.

[137] Giacomo Bagarella, Renato M Lazzarin, and Biagio Lamanna. Cycling losses in refrigeration equipment: An experimental evaluation. *International Journal of Refrigeration*, 36(8):2111–2118, 2013.

[138] WJ Mulroy and DA Didion. Refrigerant migration in a split-unit air conditioner. discussion. *ASHRAE transactions*, 91(1):193–206, 1985.

[139] MI Belth, TE Grzymala, and DR Tree. Transient mass flow rate of a residential air-to-air heat pump. *International journal of refrigeration*, 11(5):298–304, 1988.

[140] Steffen Peuker and Predrag Hrnjak. Refrigerant mass and oil migration during start-up transient. 2008.

[141] Tingxun Li, Jian Lu, Lei Chen, Dongcai He, Xiaozhou Qiu, Hongyao Li, and Zhen Liu. Measurement of refrigerant mass distribution within a r290 split air conditioner. *International Journal of Refrigeration*, 57:163–172, 2015.

[142] WE Murphy and VW Goldschmidt. The degradation coefficient of a field-tested self-contained 3-ton air conditioner. *ASHRAE Transactions*, 85(Part 2):396, 1979.

[143] Man-Hoe Kim and Clark W Bullard. Dynamic characteristics of a r-410a split air-conditioning system. *International Journal of Refrigeration*, 24(7):652–659, 2001.

[144] Steffen Peuker. *Experimental and Analytical Investigation of Refrigerant and Lubricant Migration*. PhD thesis, University of Illinois at Urbana-Champaign, Urbana, Illinois, 2010.

[145] WE Murphy and VW Goldschmidt. Cyclic characteristics of a typical residential air conditioner-modeling of start-up transients. *ASHRAE transactions*, 91(2A):427–437, 1985.

[146] WE Murphy and VW Goldschmidt. Cycling characteristics of a residential air conditioner-modeling of shutdown transients. *ASHRAE Transactions*, 92(1A):186–202, 1986.

[147] B Ozyurt and AN Egrican. Experimental investigation of charge distribution in a vapor compression refrigeration cycle. In *Second IIR Workshop on Refrig erant Charge Reduction Stockholm Sweden*, 2010.

[148] Bin Li, Steffen Peuker, Predrag S Hrnjak, and Andrew G Alleyne. Refrigerant mass migration modeling and simulation for air conditioning systems. *Applied Thermal Engineering*, 31(10):1770–1779, 2011.

[149] Satyam Bendapudi, James E Braun, and Eckhard A Groll. A comparison of moving-boundary and finite-volume formulations for transients in centrifugal chillers. *International journal of refrigeration*, 31(8):1437–1452, 2008.

[150] GE Kelly and WH Parken Jr. Method of testing, rating and estimating the seasonal performance of central air conditioners and heat pumps operating in the cooling mode. *Final Report National Bureau of Standards, Washington, DC. Center for Building Technology.*, 1, 1978.

[151] ASHRAE Standard 116-2010: Methods of Testing for Rating Seasonal Efficiency of Unitary Air Conditioners and Heat Pumps (ANSI Approved). Standard, American Society of Heating, Refrigerating and Air-Conditioning Engineers, Atlanta, GA, 1992.

[152] David A Didion and George E Kelly. New testing and rating procedures for seasonal performance of heat pumps. *ASHRAE Journal*, 21(9):40–44, 1979.

[153] ANSI/ASHRAE 37-2009: Methods of Testing for Rating Electrically Driven Unitary Air-Conditioning and Heat Pump Equipment. Standard, American Society of Heating, Refrigerating and Air-Conditioning Engineers, Atlanta, GA, 2009.

[154] ASHRAE Standard 41.2-1987 (RA 92): Standard Methods for Laboratory Air-Flow Measurement. Standard, American Society of Heating, Refrigerating and Air-Conditioning Engineers, Atlanta, GA, 1992.

[155] V W Goldschmidt, G H Hart, and R C Reiner. A note on the transient performance and degradation coefficient of a field tested heat pump-cooling and heating mode. *ASHRAE Transactions*, 86(Part 2):368, 1980.

[156] D L O'Neal and S Katipamula. Development of nondimensional cycling model for estimating the seasonal performance of air conditioners. *Journal of solar energy engineering*, 115(3):176–181, 1993.

[157] Srinivas Katipamula and Dennis L O'Neal. A part load factor for a heat pump derived from laboratory measurements. *Energy and buildings*, 19(2):125–132, 1992.

[158] Hugh I Henderson, Danny Parker, and Yu J Huang. Improving DOE-2's RESYS routine: User defined functions to provide more accurate part load energy use and humidity predictions. In *2000 ACEEE Summer Study on Energy Efficiency in Buildings - Proceedings*, number Panel 1. Residential Buildings: Technologies, Design and Performance Analysis, pages 1.113–1.124. European Council for an Energy Efficient Economy, 2000.

[159] Ernesto Bettanini, Alessio Gastaldello, and Luigi Schibuola. Simplified models to simulate part load performances of air conditioning equipments. In *8th International IBPSA conference, Eindhoven, Netherland*, 2003.

[160] ISO Standard 16358-1. Air-cooled air conditioners and air-to-air heat pumps - testing and calculating methods for seasonal performance factors - part 1: cooling seasonal performance factor. *International Standards Organization*, 2013.

[161] E Fuentes, D A Waddicor, and J Salom. Improvements in the characterization of the efficiency degradation of water-to-water heat pumps under cyclic conditions. *Applied energy*, 179:778–789, 2016.

[162] AHRI Standard 210/240. Performance Rating of Unitary Air Conditioning and Air-Source Heat Pump Equipment. *Air-Conditioning, Heating, & Refrigeration Institute, Arlington, VA 22201, USA*, 2017.

[163] Modelica. Modelica and the Modelica Association, 2017.

[164] Modelica Association. Modelica standard library. *Online, URL: http://www. modelica. org/libraries/Modelica*, 2008.

[165] Hongtao Qiao, Vikrant Aute, and Reinhard Radermacher. Transient modeling of a flash tank vapor injection heat pump system Part I: Model development. *International journal of refrigeration*, 49:169–182, 2015.

[166] Y Cao and A Faghri. A numerical analysis of phase-change problems including natural convection. *Journal of heat transfer*, 112(3):812–816, 1990.

[167] Vasilios Alexiades and Alan D Solomon. Mathematical modeling of melting and freezing processes, hemisphere publ, 1993.

[168] Puretemp -global authority on phase change materials, 2017. [Online; accessed 12-February-2017].

[169] Stuart W Churchill. Comprehensive correlating equations for heat, mass and momentum transfer in fully developed flow in smooth tubes. *Industrial & Engineering Chemistry Fundamentals*, 16(1):109–116, 1977.

[170] Pengfei Li, Yaoyu Li, and John E Seem. Modelica-based dynamic modeling of a chilled-water cooling coil. *HVAC&R Research*, 16(1):35–58, 2010.

[171] SW Churchill and R Usagi. A general expression for the correlation of rates of transfer and other phenomena. *AIChE Journal*, 18(6):1121–1128, 1972.

[172] Wolfgang Wagner and Hans-Joachim Kretzschmar. Iapws industrial formulation 1997 for the thermodynamic properties of water and steam. *International Steam Tables: Properties of Water and Steam Based on the Industrial Formulation IAPWS-IF97*, pages 7–150, 2008.

[173] Haobo Jiang, Vikrant Aute, and Reinhard Radermacher. Coildesigner: a general-purpose simulation and design tool for air-to-refrigerant heat exchangers. *International Journal of Refrigeration*, 29(4):601–610, 2006.

[174] Michael Wetter, Wangda Zuo, Thierry S Nouidui, and Xiufeng Pang. Modelica buildings library. *Journal of Building Performance Simulation*, 7(4):253–270, 2014.

[175] YL Hao and YX Tao. Heat transfer characteristics of melting ice spheres under forced and mixed convection. *Transactions-American Society of Mechanical Engineers Journal of Heat Transfer*, 124(5):891–903, 2002.

[176] James Marco, Neelu Kumari, W Dhammika Widanage, and Peter Jones. A cell-in-the-loop approach to systems modelling and simulation of energy storage systems. *Energies*, 8(8):8244–8262, 2015.

[177] Markus Einhorn, Valerio Conte, Christian Kral, and Jürgen Fleig. Comparison of electrical battery models using a numerically optimized parameterization method. In *2011 IEEE Vehicle Power and Propulsion Conference*, pages 1–7. IEEE, 2011.

[178] M Einhorn, F V Conte, C Kral, C Niklas, H Popp, and J Fleig. A modelica library for simulation of electric energy storages. In *Proceedings of the 8th International Modelica Conference; March 20th-22nd; Technical Univeristy; Dresden; Germany*, number 63, pages 436–445. Linköping University Electronic Press, 2011.

[179] Muhammet Kasim Gonullu. Development of a mobile robot to be used in mobile robot research, 2013.

[180] Aspen Compressor, 2017.

[181] Yilin Du, Jan Muehlbauer, Jiazhen Ling, Vikrant Aute, Yunho Hwang, and Reinhard Radermacher. Rechargeable Personal Air Conditioning Device. In *ASME 2016 10th International Conference on Energy Sustainability collocated with the ASME 2016 Power Conference and the ASME 2016 14th International Conference on Fuel Cell Science, Engineering and Technology*. American Society of Mechanical Engineers, 2016.

[182] Shengwei Zhu, Daniel Dalgo, Jelena Srebric, and Shinsuke Kato. Cooling efficiency of a spot-type personalized air-conditioner. *Building and Environment*, 121:35–48, 2017.

[183] U.S. Energy Information Administration. Independent statistics and analysis, 2017.

[184] Mohammad Heidarinejad, Daniel Alejandro Dalgo, Nicholas W Mattise, and Jelena Srebric. Personalized cooling as an energy efficiency technology for city energy footprint reduction. *Journal of Cleaner Production*, 171:491–505, 2018.

[185] Xavier Py, Regis Olives, and Sylvain Mauran. Paraffin/porous-graphite-matrix composite as a high and constant power thermal storage material. *International Journal of heat and mass transfer*, 44(14):2727–2737, 2001.

[186] Yajuan Zhong, Sizhong Li, Xinghai Wei, Zhanjun Liu, Quangui Guo, Jingli Shi, and Lang Liu. Heat transfer enhancement of paraffin wax using compressed expanded natural graphite for thermal energy storage. *Carbon*, 48(1):300–304, 2010.

[187] Xianglei Wang, Quangui Guo, Yajuan Zhong, Xinghai Wei, and Lang Liu. Heat transfer enhancement of neopentyl glycol using compressed expanded natural graphite for thermal energy storage. *Renewable energy*, 51:241–246, 2013.

[188] Anne M Mallow, Omar Abdelaziz, and Samuel Graham. Thermal Charging Study of Compressed Expanded Natural Graphite/Phase Change Material Composites. Technical report, 2016.

[189] Vikrant Aute and Reinhard Radermacher. Standardized polynomials for fast evaluation of refrigerant thermophysical properties. In *15th International Refrigeration and Air Conditioning Conference*, pages 2462:1–10, Purdue, Indiana, USA, 2014.

[190] S Bodjona, E Videcoq, R Saurel, A Chinnayya, A M Benselama, and Y Bertin. Transient simulation of a two-phase loop thermosyphon with a model out of thermodynamic equilibrium. *International Journal of Heat and Mass Transfer*, 108:2321–2332, 2017.

[191] Frank P Incropera and David P Dewitt. Introduction to Heat Transfer. 2002.

[192] Henry Hu and Stavros A Argyropoulos. Mathematical modelling of solidification and melting: a review. *Modelling and Simulation in Materials Science and Engineering*, 4(4):371, 1996.

[193] Yvan Dutil, Daniel R Rousse, Nizar Ben Salah, Stéphane Lassue, and Laurent Zalewski. A review on phase-change materials: Mathematical modeling and simulations. *Renewable and Sustainable Energy Reviews*, 15(1):112–130, 2011.

[194] M Iten and S Liu. A work procedure of utilising PCMs as thermal storage systems based on air-TES systems. *Energy Conversion and Management*, 77:608–627, 2014.

[195] V R Voller. Fast implicit finite-difference method for the analysis of phase change problems. *Numerical Heat Transfer*, 17(2):155–169, 1990.

[196] Kevin Merlin, Didier Delaunay, Jérôme Soto, and Luc Traonvouez. Heat transfer enhancement in latent heat thermal storage systems: comparative study of different solutions and thermal contact investigation between the exchanger and the PCM. *Applied Energy*, 166:107–116, 2016.

[197] M M Shah. Chart correlation for saturated boiling heat transfer: equations and further study. *ASHRAE Trans.;(United States)*, 88(CONF-820112-), 1982.

[198] Eckehard F Schmidt. Wärmeübergang und Druckverlust in rohrschlangen. *Chemie Ingenieur Technik*, 39(13):781–789, 1967.

[199] Rüdiger Franke, Francesco Casella, Martin Otter, Michael Sielemann, Hilding Elmqvist, Sven Erik Mattson, and Hans Olsson. Stream Connectors An Extension of Modelica for Device-Oriented Modeling of Convective Transport Phenomena. 43:108–121, 2009.

[200] Mirza M Shah. Comprehensive correlations for heat transfer during condensation in conventional and mini/micro channels in all orientations. *International journal of refrigeration*, 67:22–41, 2016.

[201] Chi-Chuan Wang, Kuan-Yu Chi, and Chun-Jung Chang. Heat transfer and friction characteristics of plain fin-and-tube heat exchangers, part ii: Correlation. *International Journal of Heat and mass transfer*, 43(15):2693–2700, 2000.

[202] Stuart W Churchill and Humbert H S Chu. Correlating equations for laminar and turbulent free convection from a vertical plate. *International journal of heat and mass transfer*, 18(11):1323–1329, 1975.

[203] Liu Liu, Felix Felgner, and Georg Frey. Comparison of 4 numerical solvers for stiff and hybrid systems simulation. In *Emerging Technologies and Factory Automation (ETFA), 2010 IEEE Conference on*, pages 1–8. IEEE, 2010.

[204] Yilin Du. Battery powered portable vapor compression cycle system with PCM condenser. Master's thesis, Department of Mechanical Engineering, University of Maryland, College Park, 2016.

[205] Rohit Dhumane, Anne Mallow, Yiyuan Qiao, Kyle R Gluesenkamp, Samuel Graham, Jiazhen Ling, and Reinhard Radermacher. Enhancing the Thermosiphon-Driven Discharge of a Latent Heat Thermal Storage System used in a Personal Cooling Device. *International Journal of Refrigeration*, In Press, 2018.

[206] Thomas F Stocker, D Qin, G K Plattner, M Tignor, S K Allen, J Boschung, A Nauels, Y Xia, V Bex, and P M Midgley. Climate change 2013: the physical science basis. Intergovernmental panel on climate change, working group I contribution to the IPCC fifth assessment report (AR5). *New York*, 2013.

[207] United States Environmental Protection Agency. Recent International Developments under the Montreal Protocol, 2017.

[208] United Nations. Kigali Amendment to the Montreal Protocol Art IV(1), 2016.

[209] Björn Palm. Hydrocarbons as refrigerants in small heat pump and refrigeration systemsa review. *International journal of refrigeration*, 31(4):552–563, 2008.

[210] Weier Tang, Guogeng He, Dehua Cai, Yihao Zhu, Aoni Zhang, and Qiqi Tian. The experimental investigation of refrigerant distribution and leaking characteristics of R290 in split type household air conditioner. *Applied Thermal Engineering*, 115:72–80, 2017.

[211] Anne Mallow, Omar Abdelaziz, and Samuel Graham. Thermal charging performance of enhanced phase change material composites for thermal battery design. *International Journal of Thermal Sciences*, 127:19–28, 2018.

[212] Debabrata Pal and Yogendra K Joshi. Melting in a side heated tall enclosure by a uniformly dissipating heat source. *International Journal of Heat and Mass Transfer*, 44(2):375–387, 2001.

[213] CC Wang, WL Fu, and CT Chang. Heat transfer and friction characteristics of typical wavy fin-and-tube heat exchangers. *Experimental thermal and fluid science*, 14(2):174–186, 1997.

[214] Satish G Kandlikar. A general correlation for saturated two-phase flow boiling heat transfer inside horizontal and vertical tubes. *Journal of heat transfer*, 112(1):219–228, 1990.

[215] FW Dittus and LMK Boelter. Heat transfer in automobile radiators of the tubular type. *International Communications in Heat and Mass Transfer*, 12(1):3–22, 1985.

[216] Heinrich Blasius. Das ähnlichkeitsgesetz bei reibungsvorgängen in flüssigkeiten. In *Mitteilungen über Forschungsarbeiten auf dem Gebiete des Ingenieurwesens*, pages 1–41. Springer, 1913.

[217] H Müller-Steinhagen and K Heck. A simple friction pressure drop correlation for two-phase flow in pipes. *Chemical Engineering and Processing: Process Intensification*, 20(6):297–308, 1986.

[218] S Zia Rouhani and Eva Axelsson. Calculation of void volume fraction in the subcooled and quality boiling regions. *International Journal of Heat and Mass Transfer*, 13(2):383–393, 1970.

[219] D Steiner. Heat transfer to boiling saturated liquids vdi-wärmeatlas (vdi heat atlas). *VDI-Gesellschaft Verfahrenstechnik und Chemieingenieurswesen (GCV), Düsseldorf*, 1993.

[220] Leszek Wojtan, Thierry Ursenbacher, and John R Thome. Interfacial measurements in stratified types of flow. part ii: Measurements for r-22 and r-410a. *International journal of multiphase flow*, 30(2):125–137, 2004.

[221] SL Smith. Void fractions in two-phase flow: a correlation based upon an equal velocity head model. *Proceedings of the Institution of Mechanical Engineers*, 184(1):647–664, 1969.

[222] D Chisholm. Void fraction during two-phase flow. *Journal of Mechanical Engineering Science*, 15(3):235–236, 1973.

[223] SM Zivi. Estimation of steady-state steam void-fraction by means of the principle of minimum entropy production. *Journal of heat transfer*, 86(2):247–251, 1964.

[224] Pieter Dermont, Dirk Limperich, Johan Windahl, Katrin Prölss, and Carsten Kübler. Advances of zero flow simulation of air conditioning systems using modelica. In *The First Japanese Modelica Conferences, May 23-24, Tokyo, Japan*, number 124, pages 139–144. Linköping University Electronic Press, 2016.

[225] John Gall, Daniel E Fisher, Gabrielle Corti, Stefano Marelli, and Lorenzo Cremaschi. Modeling of r-410a variable capacity compressor with modelica and experimental validation. *International Journal of Refrigeration*, 58:90–109, 2015.

[226] Bell, Ian and Lemort, Vincent and Braun, Jim and Groll, Eckhard. In *International Compressor Engineering Conference*, pages 1872:1–10, Purdue, Indiana, USA, 2008.

[227] Haorong Li and James E Braun. A method for modeling adjustable throat-area expansion valves using manufacturers' rating data. *HVAC&R Research*, 14(4):581–595, 2008.

[228] Stuart W Churchill and Humbert HS Chu. Correlating equations for laminar and turbulent free convection from a vertical plate. *International journal of heat and mass transfer*, 18(11):1323–1329, 1975.

[229] Michael Wetter, Wangda Zuo, Thierry S Nouidui, and Xiufeng Pang. Modelica buildings library. *Journal of Building Performance Simulation*, 7(4):253–270, 2014.

[230] Tianyue Qiu. Refrigerant charge distribution in unitary air-conditioning units. Master's thesis, University of Maryland, 2018.

[231] Pasquale Memmolo, Rosario Schiano Lo Moriello, Paolo Pinto, and Blandina de Iorio. On the use of numeric integration for uncertainty evaluation in indirect measurements. In *Advanced Methods for Uncertainty Estimation in Measurement, 2007 IEEE International Workshop on*, pages 89–92. IEEE, 2007.

[232] Bureau International des Poids et Mesures, Commission électrotechnique internationale, and Organisation internationale de normalisation. *Guide to the expression of uncertainty in measurement*. International Organization for Standardization, 1995.

[233] Damien John Batstone. Teaching uncertainty propagation as a core component in process engineering statistics. *Education for Chemical Engineers*, 8(4):e132–e139, 2013.

[234] ASME PTC 19.1-2013: Test Uncertainty. Standard, American Society of Mechanical Engineers, New York, NY, 2013.

[235] Brandon M Wilson and Barton L Smith. Taylor-series and monte-carlo-method uncertainty estimation of the width of a probability distribution based on varying bias and random error. *Measurement Science and Technology*, 24(3):035301, 2013.